Bioactive Cellulose Nanocrystal Reinforced 3D Printable Poly(ε-caprolactone) Nanocomposite for Bone Tissue Engineering

Jung Ki Hong

Dissertation submitted to the faculty of the Virginia Polytechnic Institute and State University in partial fulfillment of the requirements for the degree of

Doctor of Philosophy
In
Macromolecular Science and Engineering

Maren Roman, Chair
Kevin J. Edgar
Charles E. Frazier
Scott H. Renneckar
Abby R. Whittington

February 6, 2015
Blacksburg, Virginia

Keywords: cellulose nanocrystal, poly(ε-caprolactone), nanocomposite, biomineralization, 3D printing, porous bone scaffold, mechanical performance, biocompatibility

Bioactive Cellulose Nanocrystal Reinforced 3D Printable Poly(ε-caprolactone) Nanocomposite for Bone Tissue Engineering

Jung Ki Hong

ABSTRACT

Polymeric bone scaffolds are a promising tissue engineering approach for the repair of critical-size bone defects. Porous three-dimensional (3D) scaffolds play an essential role as templates to guide new tissue formation. However, there are critical challenges arising from the poor mechanical properties and low bioactivity of bioresorbable polymers, such as poly(ε-caprolactone) (PCL) in bone tissue engineering applications. This research investigates the potential use of cellulose nanocrystals (CNCs) as multi-functional additives that enhance the mechanical properties and increase the biomineralization rate of PCL. To this end, an *in vitro* biomineralization study of both sulfuric acid hydrolyzed-CNCs (SH-CNCs) and surface oxidized-CNCs (SO-CNCs) has been performed in simulated body fluid in order to evaluate the bioactivity of the surface functional groups, sulfate and carboxyl groups, respectively. PCL nanocomposites were prepared with different SO-CNC contents and the chemical/physical properties of the nanocomposites were analyzed. 3D porous scaffolds with fully interconnected pores and well-controlled pore sizes were fabricated from the PCL nanocomposites with a 3D printer. The mechanical stability of the scaffolds were studied using creep test under dry and submersion conditions. Lastly, the biocompatibility of CNCs and 3D printed porous scaffolds were assessed *in vitro*.

The carboxyl groups on the surface of SO-CNCs provided a significantly improved calcium ion binding ability which could play an important role in the biomineralization (bioactivity) by induction of mineral formation for bone tissue engineering applications. In addition, the mechanical properties of porous PCL nanocomposite scaffolds were pronouncedly reinforced by incorporation of SO-CNCs. Both the compressive modulus and creep resistance of the PCL scaffolds were enhanced either in dry or in submersion conditions at 37 °C. Lastly, the biocompatibility study demonstrated that both the CNCs and material fabrication processes (e.g., PCL nanocomposites and 3D printing) were not toxic to the preosteoblasts (MC3T3 cells). Also, the SO-CNCs showed a positive effect on biomineralization of PCL scaffolds (i.e., accelerated calcium or mineral deposits on the surface of the scaffolds) during *in vitro* study. Overall, the SO-CNCs could play a critical role in the development of scaffold materials as a potential candidate for reinforcing nanofillers in bone tissue engineering applications.

Acknowledgements

I would like to express my sincere thanks to everyone who has helped me to complete my Ph.D. research. This has been quite a long, but the most enjoyable and meaningful time to develop my academic life. I have received thoughtful guidance and support that cannot be expressed in words from many people and it has been a great privilege for me. I would like to pay my sincere gratitude.

First of all, I would like to thank my advisor, Professor Maren Roman. From the beginning to the end, her continuous support has given me the confidence to pursue my research. I cannot thank her enough for providing me with the knowledge to grow and the chance to develop my research idea throughout the entire academic career. I would like to thank my Ph.D. committee members, Professor Kevin Edgar, Charles Frazier, Scott Renneckar and Abby Whittington for their great support and cooperation throughout my graduate research. I am grateful for discussions with them, their expert advice and sharing their facilities for this research. I cannot help but admire their enthusiasm for academic development. Special thanks to Professor Charles Frazier and his group for their kind assistance in the laboratory experiment. Also, I am extremely thankful to Shelley Cooke, who as a co-author for chapter five, for sharing expertise, and sincere and valuable discussion.

My sincere appreciation is extended to many people in the Department of Sustainable Biomaterials, especially, Rick Caudill, David Jones, Debbie Garnand, Angie Riegel, Dr. Ann Norris and Professor Audrey Zink-Sharp for their help.

Last but not least, this work is dedicated to my family and I would like to extend my deepest gratitude. Their everlasting love, support and sacrifice became the driving force in my life.

This work was supported primarily by the Institute for Critical Technology and Applied Science (ICTAS). This material is based upon work supported by the National Science Foundation under Award No. DMR-0907567, Omnova, Inc. and Tembec, Inc. The project was supported by the Agriculture and Food Research Initiative of the USDA National Institute of Food and Agriculture, grant number 2010-65504-20429.

Table of Contents

List of figures

List of tables

Chapter 1. Introduction

1.1 Motivations and project description

Bone is one of the few organs in the body that has the ability to heal itself by self-regeneration without scar tissue formation following injury. However, the self-healing capacity of bone is limited to smaller than critical-sized bone defects. The critical-sized bone defect can be treated with bone grafts, such as autografts, allografts, and xenografts or with metal and ceramic implants. These approaches have several limitations including donor site morbidity, donor bone supply shortage, infection, corrosion, stress shielding, and secondary surgery.

Tissue engineering is an alternative approach that has the potential to overcome the problems associated with the replacement of damaged tissues or organs. It is generally desired that materials/scaffolds possess certain properties such as biocompatibility, bioactivity, bioresorbability, and the capacity for tissue ingrowth. Engineered bone scaffolds, in particular, need to be rigid and biomineralizable. Bone scaffolds are a promising approach to replacing and mimicking the properties of natural bone tissue. Porous three-dimensional (3D) scaffolds play an essential role as temporary structural templates to guide new tissue formation. 3D printing techniques enable the fabrication of well-controlled scaffolds with fully interconnected pore networks and thus make customization for specific defect sites possible. A variety of materials have been investigated to develop scaffolds that fulfill the requirements for bone tissue engineering

applications. Polymers exhibit tunability, processability, biocompatibility, and versatility, thus they have greater potential in the field of bone tissue engineering relative to other materials, such as ceramics and metals. However, polymeric materials present critical challenges that need to be addressed, namely, inferior strength, stiffness, and bioactivity.

Poly(ε-caprolactone) (PCL) is a bioresorbable and semi-crystalline linear polymer that has been approved by the U.S. Food and Drug Administration and has long been used for biomedical applications, such as drug delivery systems and medical devices. However, the potential application of PCL for bone scaffolds has been hindered by its insufficient load-bearing properties and poor biomineralization (bioactivity).

The aim of this research was to improve the properties of PCL for bone tissue engineering applications via the incorporation of cellulose nanocrystals (CNCs). CNCs are highly crystalline rod-like particles that are derived from various sources of cellulose found in nature by acid hydrolysis. They possess inherent advantages, such as rigidity, high aspect ratio, and ease of surface modification with different functional groups. One of the main focuses of this research is to highlight the potential use of CNCs in bone tissue engineering by developing a novel bioactive PCL/CNC nanocomposite scaffold that will integrate the properties of both the bioresorbable polymer and natural nanomaterial. The CNCs are hypothesized to act as a multi-functional reinforcing additive resulting in enhanced mechanical properties as well as an increased biomineralization rate. Thus, the overall goal of this project is a nanocomposite material, based on PCL and surface-oxidized CNCs (SO-CNCs), for 3D printing of scaffolds that

stimulate bone formation, provide adequate mechanical support during healing, and are gradually absorbed by the body (Figure 1.1).

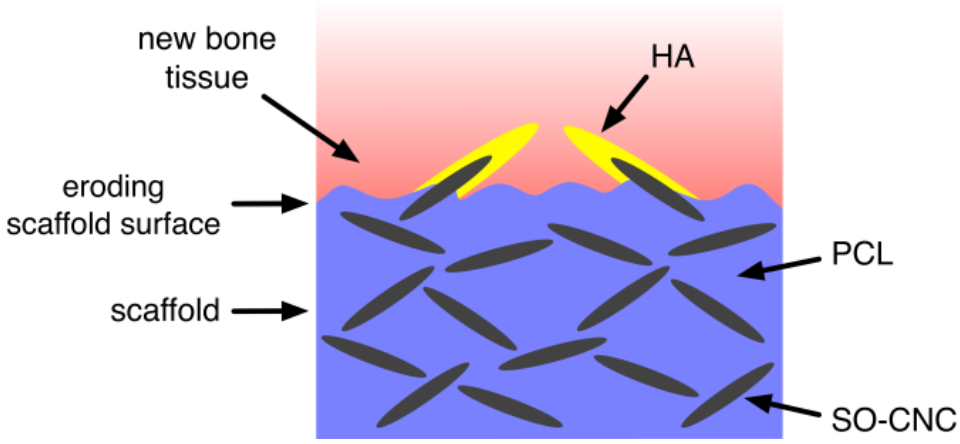

Figure 1.1. SO-CNCs provide mechanical reinforcement to the PCL scaffold and induce hydroxyapatite (HA) formation in the new bone tissue upon PCL resorption.

The objectives of this research are to:

1. Determine the effects of surface oxidation on the bioactivity (biomineralization) of CNCs *in vitro*
2. Assess the physical/chemical properties of SO-CNC/PCL nanocomposites
3. Evaluate the mechanical performance of the SO-CNC/PCL scaffolds
4. Assess the biocompatibility of CNCs and 3D printed films and scaffolds *in vitro*

Chapter 2. Literature review

2.1. Introduction

The skeletal and muscular systems are often grouped together and called the musculoskeletal system because the interaction between the two systems plays an important role in body locomotion. Bone is a rigid organ of the human skeletal system. It provides humans with important physiological functions including structural support, protection of the internal organs, blood production, mineral storage, and homeostasis. These functions become crucial in the case of skeletal system disorders (e.g., diseases and fractures) because the disorders may cause severe long-term pain and, physical disability [1]. Skeletal system disorders can be caused by genetic abnormalities, nutritional deficiencies (e.g., vitamin D, calcium, and phosphorus) and hormonal disorders [1]. Also, skeletal system disorders are related to population aging, obesity, poor physical activity and accident rate.

The United Nations/World Health Organization proclaimed 2000-2010 as the Bone and Joint Decade to emphasize the severity of musculoskeletal system disorders [2, 3]. In spite of the widespread prevalence of musculoskeletal conditions (Figure 2.1), they are relatively under-recognized as they are a lower mortality risk compared to other medical conditions. However, musculoskeletal disorders are lifelong, painful, and often restrict daily activity causing a high morbidity cost.

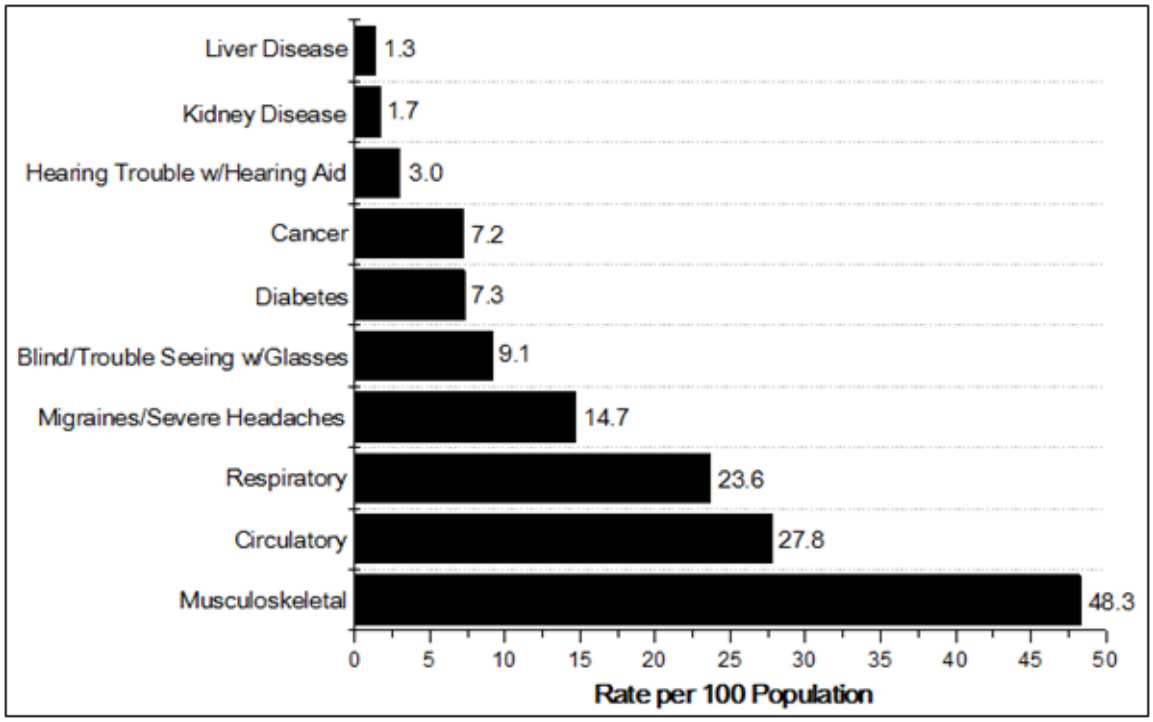

Figure 2.1. Prevalence of self-Reported Primary Medical Conditions for Persons Aged 18 and over, United States 2005. Joshua J. Jacobs, G.B.J.A., John-Erik Bell, Stuart L. Weinstein, John P. Dormans, Steve M. Gnatz, Nancy Lane, J. Edward Puzas, E. William St. Clair, Edward H. Yelin. *The Burden of Musculoskeletal Diseases in the United States*. Available from: http://www.boneandjointburden.org/ [4]. Used under fair use, 2015.

In the U.S., for example, health care for musculoskeletal conditions costs up to $254 billion (USD) per year, and accounts for more than 130 million patient visits in 2000 [5-7]. Specifically, the clinical need for bone-related treatment is increasing due to an extended human life span and increased accident rate. Up to 15 million people are injured or disabled each year in road accidents [5-7]. An average of 24% of hip fracture patients aged 50 and over die in the year following their fracture, and only 15% of hip fracture patients can walk across a room unaided at six months after a hip fracture [8]. Medical

expenses relating to fracture, reattachment, and replacement of hip and knee joint was estimated to be over $20 billion (USD) in 2003, and predicted to increase to over $74 billion (USD) by the year 2015 [7, 9].

From a therapeutic perspective, bone grafts have been a primary concern for the treatment of injured or diseased bone that may not be capable of self-healing. So far, the most common treatments for bone grafts are autologous (from a patient's own tissue) and allogeneic (from another person's tissue) transplantations as restorative therapies. Worldwide, approximately 2.2 million (more than 500,000 in the U.S.) orthopedic procedures including autografts and allografts are performed annually [10, 11]. Although the traditional grafting methods have benefits in certain cases, there are several disadvantages, such as morbidity associated with a secondary surgical site, limited availability of graft material, infection, and disease transmission [12].

Therefore, tissue engineering as an alternative treatment could play a valuable role in the development of functional bone grafts. Bone scaffolds are a promising tissue engineering approach to replacing and mimicking the properties of natural bone tissue. As temporary matrices for bone growth, bone scaffolds help provide a specific environment and architecture for native tissue regeneration [12]. A variety of materials including metals, ceramics, and natural/synthetic polymers have been investigated in the development of scaffolds that fulfill the requirements for bone tissue engineering. Although there has been considerable progress, much more remains to be done to improve the materials.

For instance, metals such as titanium, stainless steel, and cobalt-chromium provide immediate mechanical integrity at the implantation site [13]. However, metallic implants can cause corrosion which is a primary concern for the biomaterials scientist. Also, the excessively high elastic modulus relative to natural bone may induce a "stress shielding" response. Furthermore, the lack of biodegradability requires additional surgery [14-17]. Ceramics such as alumina (bioinert), bioglass (bioactive), and hydroxyapatite (HA, biodegradable), have been broadly used as biomaterials because of their high compressive strength, wear resistance, and stiffness, but are not suitable for applications in which torsion, bending, or shear stress are involved because of their brittle nature and very low tensile strength [13].

As alternatives, both synthetic and natural polymers have been widely investigated for biomedical applications. The main advantages of natural biodegradable polymers, such as collagen and polysaccharides, are their good biocompatibility, biodegradability, chemical versatility, and abundance [18-20]. Also, synthetic bioresorbable polymers can be degraded through hydrolytic processes and the degradation rate can be tailored [21, 22]. Because of their tunability, processability, biocompatibility and versatility, the importance of polymers is likely to increase in the field of bone tissue engineering. Even though polymeric materials have great potential as bone scaffolds for mimicking natural bone tissue, the low mechanical stability of biodegradable and bioresorbable polymeric materials currently precludes them from being a viable option in load-bearing bone scaffold applications.

2.2. Bone scaffolds

2.2.1. Bone tissue properties

As a rigid mineralized connective tissue, bone is a remarkable organ of the human skeletal system and performs several critical physiological functions in the human body. Bone provides structural support and sites of muscle attachment for locomotion, protects vital internal organs, produces hematopoietic and mesenchymal stem cells, and retains reserve stores of calcium, phosphate, and magnesium ions to maintain homeostasis [22-24].

Bone is composed of 65% mineral and 35% organic matrix. The bone mineral is largely impure HA, $Ca_{10}(PO_4)_6(OH)_2$, and also contains other components including carbonate, magnesium, fluoride, and citrate. The mineral phase of bone plays important roles in both the mechanical strength of bone and mineral ion homeostasis. The organic matrix consists of collagen (90%) and non-collagenous proteins, such as osteocalcin, osteonectin, osteopontin, and bone sialoprotein. Also, its hierarchical structural organization makes bone a strong and tough nanocomposite [25]. Bone tissue (or osseous tissue) differs from bone itself as an organ made up of other components, including bone marrow, blood vessels, and periosteum.

2.2.1.1. Anatomy and mechanical properties of bone

Bone in the adult skeleton is divided into two architectural forms at the macrostructure level: the external structure (cortical or compact bone) and the internal structure

(cancellous or trabecular bone) shown in Figure 2.2 [23, 26, 27]. Cortical bone represents around 80% and cancellous bone around 20% of the total bone mass of the skeleton, although different proportions of these two architectural forms can be found at various locations [28]. Cortical bone is very dense (~10% porosity) and forms the outer region of bones. Therefore, it provides most of the supportive and protective function of the skeletal system [28]. In contrast, cancellous bone has a sponge-like morphology (50-90% porosity), and thus its mechanical properties are as much as 10 times inferior to those of cortical bone [28]. The mechanical properties of cortical and cancellous bones are summarized in Table 2.1.

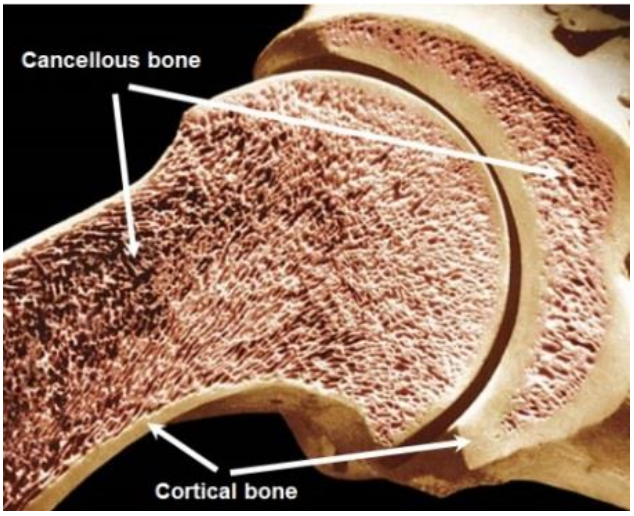

Figure 2.2. Longitudinal section of the humerus, showing outer cortical bone and inner cancellous bone. Britannica., I.E.; Available from: http://www.britannica.com/EBchecked/media/101316/Longitudinal-section-of-the-humerus-showing-outer-compact-bone-and [29]. Used under fair use, 2015.

Table 2.1. Mechanical properties of human bone. Athanasiou, K.A., et al., *Fundamentals of biomechanics in tissue engineering of bone.* Tissue Engineering, 2000. 6(4): p. 361-381 [30]. Used under fair use, 2015.

Type of bone	Type of test	Strength	Young's modulus
Cortical bone	Compression	90 - 167 MPa	4.9 - 15.5 GPa
(compact bone)	Tension	89 - 151 MPa	6.0 - 17.3 GPa
	Bending	150 - 185 MPa	5.4 - 15.8 GPa
	Torsion	7.41 ± 3.2 MPa	5.0 ± 0.2 GPa
Cancellous bone	Compression	0.6 - 13.7 MPa	12 - 900 MPa
(trabecular bone)	Tension	2.54 ± 1.18 MPa	483 MPa
	Bending	1.3 - 8.9 MPa	49 - 336 MPa

It is important to understand the structural organization of bone because the mechanical properties of bone are closely related to its components. The hierarchical structural organization of bone is shown in Figure 2.3. The basic components of bone consist of bone crystals (or apatite crystals), collagen molecules, and non-collagenous organic proteins. Plate-like apatite crystals are located in the space between the ends of collagen molecules, which assemble into collagen fibrils. Collagen fibers, which are bundles of collagen fibrils, are surrounded and infiltrated by mineral. At the sub-microstructure level, orthogonal arrangements and continuously twisted plywood-like structures of mineralized collagen fibers form the lamella [31]. The fundamental functional unit of cortical bone, the osteon, is comprised of the concentrically arranged and wrapped lamellae and a central canal called the Haversian canal (Figure 2.4). Concentric layers of

bone matrix (lamella) enclose a central blood vessel within Haversian canals. Osteocytes are interspersed between the lamella in very small spaces known as lacunae. Lacunae and Haversian canals are connected via microscopic channels (canaliculi) that provide a pathway for tissue fluid to reach the bone cells [25]. The outside of most bone is covered by a membrane called the periosteum which is a layer of fibrous connective tissue and undifferentiated cells. An internal periosteum (or the endosteum) is a membrane of osteoclasts, osteoblasts, and bone lining cells.

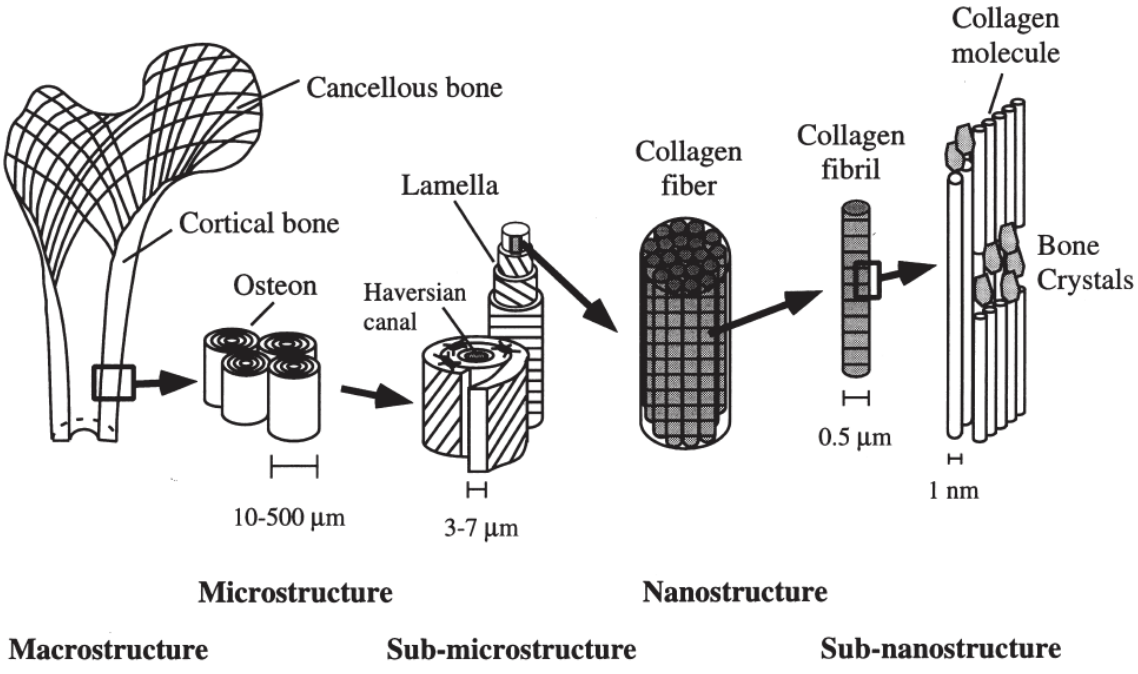

Figure 2.3. Hierarchical structural organization of bone. Rho, J.Y., L. Kuhn-Spearing, and P. Zioupos, *Mechanical properties and the hierarchical structure of bone.* Medical Engineering & Physics, 1998. 20(2): p. 92-102 [32]. Used under fair use, 2015.

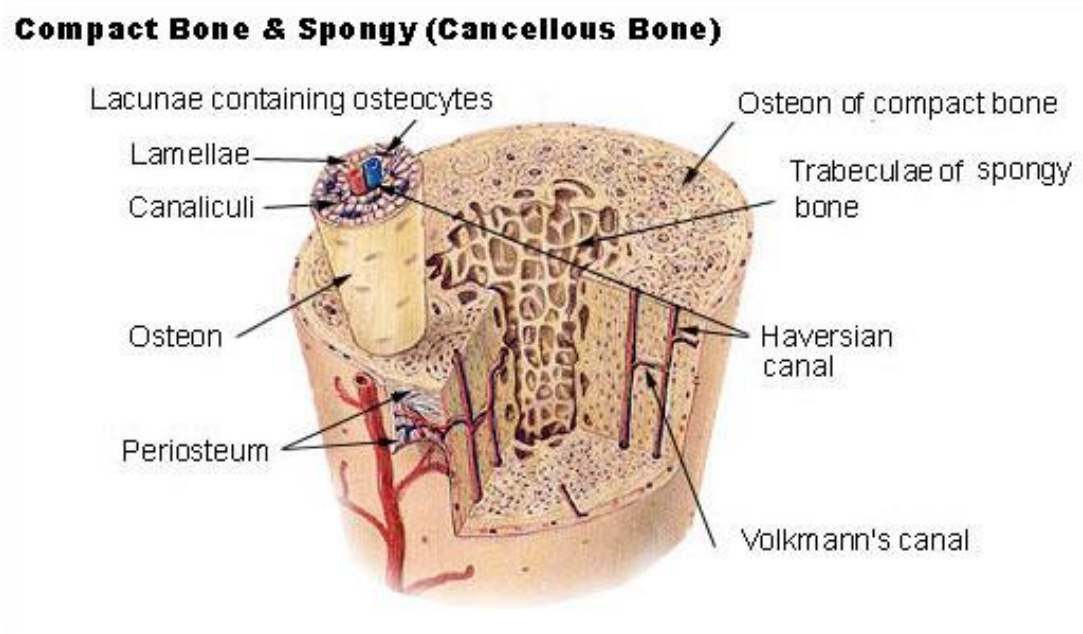

Figure 2.4. The microscopic structure of cortical and cancellous bone. U.S. National Institutes of Health. 2006; Available from: http://training.seer.cancer.gov/anatomy/skeletal/tissue.html [33]. Used under fair use, 2015.

2.2.1.2. Bone cells, bone formation, and mineralization

Bone has the ability to heal itself without scar tissue formation. In addition to its self-healing property, bone has the capacity to adapt to its environmental conditions such as mechanical and physiological changes by remodeling its mass, shape, and properties because bone is active and contains cells that respond to the environment throughout life.

There are several cell types found in bone tissue. The osteoprogenitor cells originating from mesenchymal stem cells are found in bone marrow, and have the capacity to differentiate into other cell types such as osteoblasts (or bone forming cells) which

produce bone tissue. Mesenchymal stem cells are pluripotent cells which can differentiate into several cell types for connective tissue formation including bone, muscle, tendon, cartilage, and adipose. On the other hand, hematopoietic stem cells are able to differentiate into blood cells, macrophages, monocytes, T cells, and B cells, related to the blood and immune system.

Osteoblasts are specialized fibroblasts which are mononuclear cells located on the surface of bone. They are bone forming cells that synthesize unmineralized organic matrix (or osteoid) and regulate the flux of mineral salts such as calcium and phosphate which are precipitated within the matrix in the extracellular fluid. Also, osteoblasts secrete various bone proteins (e.g., collagen, osteonectin, fibronectic, vitronectin, osteopontin, and bone sialoproteins) and regulate the matrix mineralization by secretion of the alkaline phosphate enzyme. Bone lining cells are inactive osteoblasts which line the surface of bone. Osteoclasts derived from the hematopoietic stem cell are bone resorbing cells and thus play an important role in bone remodeling. They secrete acids and enzymes (collagenase) to break down the bone matrix. Entrapped mature osteoblasts in the bone matrix are differentiated into osteocytes and serve a signaling and sensory role by communicating with the adjacent osteocytes and other cell types through lacunae and canaliculi (Figure 2.5).

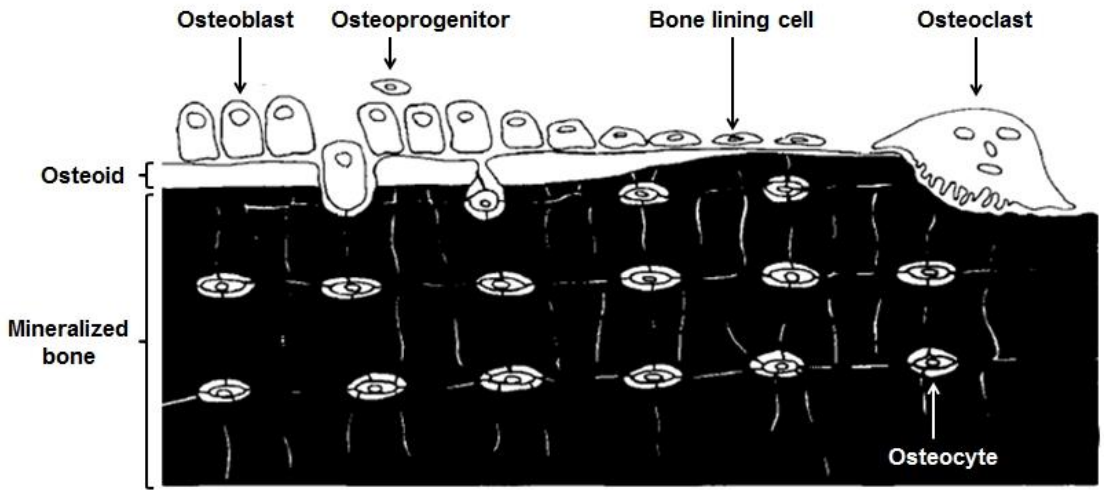

Figure 2.5. Schematic representation of the topographic relationship among bone cells. Marks, S.C. and S.N. Popoff, *Bone Cell Biology - the Regulation of Development, Structure, and Function in the Skeleton.* American Journal of Anatomy, 1988. 183(1): p. 1-44 [34]. Used under fair use, 2015.

Bone formation can occur either by intramembranous ossification, which is a direct transformation of connective tissue, or intracartilaginous (or endochondral) ossification which is a replacement of a previously formed cartilaginous model [35]. In terms of the increase in the number of cells and fibers, both bone formation processes are similar and the shape and growth of new bone tissue is genetically determined. Intramembranous ossification or membrane bone formation generates the bulk of future cortical bone, while endochondral ossification or cartilage bone formation generates the bulk of future cancellous bone [35].

In general, the mineral phase found in various living organisms, such as vertebrate bones, mammalian teeth, fish scales, and some chitin-containing crustacean composites is

known as HA or calcium phosphate [36]. In particular, the chemical composition of the mineral phase in biomineralized tissues such as bones and teeth consists of $Ca_{10}(PO_4, CO_3)_6(OH)_2$ called carbonated HA (also known as "dahllite"), and is similar to geological HA, $Ca_5(PO_4)_3(OH)$, both having a Ca/P ratio of 1.67 [37-39]. However, natural bones exhibit different properties, such as a low degree of crystallinity [40] and variation of the Ca/P ratio [41] because the body utilizes the mineral phase as a reservoir to maintain homeostasis with respect to calcium, magnesium, and phosphate ions.

To understand the different properties of bone mineral in relation to age, sex, diet, disease, and genetic issues, it is necessary to understand the biomineralization process. This is a physiological process regulated by interactions of minerals and organic extracellular molecules in the body, and controlled by various intra- and intercellular signaling pathways and genes [42]. Initially, calcium phosphate ions are actively deposited and concentrated within matrix vesicles to form HA crystals [42]. They penetrate into the matrix vesicles and create calcification nodules in the extracellular fluid [42]. After that, HA crystals proliferate within and between collagen fibrils [42]. There are several factors that affect the rate of HA crystal proliferation, such as phosphate ion concentration, pH, and the presence of proteoglycans and non-collagenous extracellular matrix proteins [43, 44].

In addition, the resorption of bone and new bone formation, so-called "bone remodeling," maintains the health of bone throughout life, and is regulated by circulating hormones and cytokines [42]. As mentioned earlier, osteoclasts break down the mineralized matrix

by acidifying the surface and degrading the mineralized matrix. Osteoblasts secrete primarily type I collagen to form an unmineralized organic matrix, or osteoid, and this matrix is then mineralized. After mineralization, the osteoblasts undergo apoptosis or differentiate into osteocytes when the cells become entrapped in the mineralized matrix [42].

2.2.2. Tissue engineering approach using bone scaffolds

Traditional and current therapeutic treatments for damaged tissues or organs by autologous, allogenic, and xenogenic (from different species) approaches have been considered. In the case of critical-sized bone defects, for example, the defect site can be replaced either by bone grafts such as autografts, allografts, and xenografts or by various artificial implants made from metal or ceramics. However, those approaches impose several limitations including donor site morbidity, infection, donor bone supply shortage, corrosion, stress shielding, and secondary surgery. Therefore, the field of tissue engineering as an alternative approach has emerged and been intensively developed over a period of decades to overcome the problems associated with the replacement of damaged tissues or organs.

One of the most commonly used definitions of tissue engineering, by Langer and Vacanti [45], is

"an interdisciplinary field of research that applies the principles of engineering and the life sciences towards the development of biological substitutes that restore, maintain, or improve tissue function."

Recently, Williams [46] has described tissue engineering as:

"the creation (or formation) of new tissue for the therapeutic reconstruction of the human body, by the deliberate and controlled stimulation of selected target cells through a systematic combination of molecular and mechanical signals."

It is generally desired that engineered tissues possess certain properties, such as biocompatibility, bioactivity, bioresorbability, and the capacity for tissue ingrowth. Engineered bone tissues, in particular, need to be rigid and biomineralizable. Bone scaffolds are a promising approach for replacing and mimicking the properties of natural bone tissue. Porous 3D scaffolds play an essential role as temporary structural templates to guide new tissue formation. However, there is no ideal scaffold to satisfy all the criteria required for bone tissue engineering applications.

2.2.2.1. Requirements for bone scaffolds

The requirements for bone scaffolds are based on three distinct but closely related concepts associated with bone regeneration by tissue engineering: osteoinduction, osteoconduction, and osseointegration [47].

Osteoinduction is defined as the recruitment of immature cells such as primitive, undifferentiated and pluripotent cells and the stimulation of these cells to differentiate into the bone forming cell lineage (e.g., preosteoblasts). This process is initiated through cell signaling pathways using inductive agents, such as bone morphogenic proteins which are the part of the transforming growth factor β (TGF-β) superfamily of ligands.

Osteoconduction leads to bone growth on a surface of implant material where this process depends on the differentiated bone cells originated by osteoinduction [48, 49]. This process can be achieved through interaction between the scaffold materials and cells by attachment and proliferation. In this sense, thus, osteoconduction has a close relationship with osteoinduction. Osseointegration implies a stable interface after direct contact between living bone tissue and implant material without fibrous tissue growth.

Langer's group described several key parameters for a desirable scaffold material including (i) biocompatibility, (ii) biodegradability, (iii) mechanical strength, and (iv) processibility [50]. In other words, the scaffold material should (i) promote cell attachment, longevity, and maintenance of cell function without any undesirable tissue response such as inflammation, (ii) not produce toxic by-products during degradation, (iii) provide enough mechanical strength with a macroporous scaffold structure, and (iv) be easily processed into a desired configuration.

Likewise, Hutmacher's group has suggested the following characteristics for an ideal scaffold [51]. A scaffold should (i) have a highly porous 3D structure with an interconnected pore network that may help cell growth and the flux of nutrients as well as metabolic waste, (ii) be biocompatible and bioresorbable, (iii) provide appropriate surface chemistry for cell attachment, proliferation, and differentiation, and (iv) have similar mechanical properties to those of the tissues at the implantation site.

2.3. Polymeric biomaterials for bone scaffolds

In the last few decades, numerous biomaterials have found widespread use in the field of tissue engineering. Although the concepts and boundaries of biomaterials are continuously changing, one of the recent definitions of a biomaterial, by Williams [46], is:

"a biomaterial is a substance that has been engineered to take a form which, alone or as part of a complex system, is used to direct, by control of interactions with components of living systems, the course of any therapeutic or diagnostic procedure, in human or veterinary medicine."

In addition, one of the important factors that distinguishes a biomaterial from any other material is its ability to sustain long term contact with living tissues in the body without causing any harm to those tissues, so-called biocompatibility [52]. Williams [52] suggested the following definition of the term biocompatibility:

"The biocompatibility of a scaffold or matrix for a tissue engineering product refers to the ability to perform as a substrate that will support the appropriate cellular activity, including the facilitation of molecular and mechanical signaling systems, in order to optimize tissue regeneration, without eliciting any undesirable local or systemic response in the eventual host."

On the other hand, the meaning of biodegradable and bioresorbable are often misused when the terminologies are used to describe the properties of polymeric biomaterials in

tissue engineering. It is important to point out the clear definitions before they are used to describe the properties or phenomenon of such biodegradable or bioresorbable polymers. Therefore, the definitions of ‘biodegradable’ and ‘bioresorbable’ are defined by Vert [53] as shown in Table 2.2.

Biomaterials can be classified into three basic types: metals, ceramics, and polymers. Among these materials, polymeric biomaterials have great inherent benefits of adjustable properties such as biocompatibility, biodegradation/bioresorption, and processibility for tissue engineering applications. According to their origin or source, polymeric biomaterials can be divided into two categories: synthetic polymers and natural polymers. Table 2.3 categorizes polymeric biomaterials on the basis of their origin.

Table 2.2. Definitions of biodegradable and bioresorbable. Vert, M., et al., *Bioresorbability and Biocompatibility of Aliphatic Polyesters.* Journal of Materials Science-Materials in Medicine, 1992. 3(6): p. 432-446 [53]. Used under fair use, 2015.

Biodegradable	Solid polymeric materials and devices which break down due to macromolecular degradation with dispersion *in vivo* but no proof for the elimination from the body (this definition excludes environmental, fungi, or bacterial degradation). Biodegradable polymeric systems or devices can be attacked by biological elements so that the integrity of the system, and in some cases but not necessarily, of the macromolecules themselves, is affected and gives fragments or other degradation by-products. Such fragments can move away from their site of action but not necessarily from the body.
Bioresorbable	Solid polymeric materials and devices which show bulk degradation and further resorb *in vivo*; i.e., polymers which are eliminated through natural pathways either because of simple filtration of degradation by-products or after their metabolization. Bioresorption is thus a concept which reflects total elimination of the initial foreign material and of bulk degradation by-products (low molecular weight compounds) with no residual side effects. The use of the word 'bioresorbable' assumes that elimination is shown conclusively.

Table 2.3. Classification of polymeric biomaterials. Ikada, Y. and H. Tsuji, *Biodegradable polyesters for medical and ecological applications.* Macromolecular Rapid Communications, 2000. 21(3): p. 117-132 [54]. Used under fair use, 2015.

Synthetic polymers		**Natural polymers**	
Sub-classification	examples	Sub-classification	Examples
1. Aliphatic polyesters		**1. Plant origin**	
1.1 Glycol and dicarboxylic acid polycondensates	Poly(ethylene succinate), Poly(butylene terephthalate)	1.1 Polysaccharides	Cellulose, Starch, Alginate
1.2 Polylactides	Polyglycolide, Polylactides	**2. Animal origin**	
1.3 Polylactones	Poly(ε-caprolactone)	2.1 Polysaccharides	Chitin (Chitosan), Hyaluronate
		2.2 Proteins	Collagen (Gelatin), Albumin
2. Polyols	Poly(vinyl alcohol)		
		3. Microbial origin	
3. Polycarbonates	Poly(ester carbonate)	3.1 Polyesters	Poly(3-hydroxyalkanoate)
4. Miscellaneous	Polyanhydrides, Polyphosphazenes, Poly(orthoesters), Poly(α-cyanoacrylate)s		

2.3.1. Synthetic polymers (Bioresorbable polymers)

Numerous synthetic polymers including polylactic acid (PLA), polyglycolic acid (PGA), and their copolymers (PLGA), polyanhydrides, polyorthoesters, PCL, polycarbonates, and polyfumarates have been studied for use in orthopedic implants [55]. In particular, the bioresorption properties of polymers play an important role in tissue engineering applications. Therefore, aliphatic polyesters have received special attention because of the potentially hydrolyzable ester linkages, and thus aliphatic polyester-based polymers are among the preferred materials for developing scaffolds.

As hydrolyzable structural materials, aliphatic polyesters can be classified into two types on the basis of their origin. For example, bacterial poly(β-hydroxy acid)s (β-PHA) are natural polymers whereas some aliphatic polyesters are synthesized by polycondensation of either hydroxyacids or diacids and dialcohols. With respect to monomer bonding one can distinguish between polyhydroxyalkanoate (PHA) and poly(alkylene dicarboxylate). PHA is a polymer derived from hydroxycarboxylic acids (HO-R-COOH), which can be divided in to α-, β-, ω-hydroxy acids based on the position of the OH group relative to the COOH end group. On the other hands, poly(alkylene dicarboxylate) is synthesized by the condensation reaction between monomers containing hydroxyl or carboxyl terminal groups [54, 56]. A classification of aliphatic polyesters is given in Table 2.4.

Table 2.4. Classification of aliphatic polyesters. Ikada, Y. and H. Tsuji, *Biodegradable polyesters for medical and ecological applications.* Macromolecular Rapid Communications, 2000. 21(3): p. 117-132 [54]. Used under fair use, 2015.

Polymers	Chemical structure	Examples
Poly(α-hydroxyacid)s	$-(O\text{-}CHR\text{-}CO)_n-$	R=H: Poly(glycolide) (PGA) $R=CH_3$: Poly(L-lactide) (PLLA)
Poly(3-hydroxyalkanoate)s	$-(O\text{-}CHR\text{-}CH_2\text{-}CO)_n-$	$R=CH_3$, C_2H_5: Poly(3-hydroxybutyrate-co-hydroxyvalerate) (PHBV)
Poly(ω-hydroxyalkanoate)s	$-(O\text{-}(CH_2)_m\text{-}CO)_x-$	m=3: Poly(γ-butyrolactone) m=4: Poly(δ-valerolactone) m=5: Poly(ε-caprolactone)
Poly(alkylene dicarboxylate)	$-(O\text{-}(CH_2)_m\text{-}O\text{-}CO\text{-}(CH_2)_n\text{-}CO)_x-$	m=2, n=2: Poly(ethylene succinate) (PES) m=4, n=2: Poly(butylene succinate) (PBS) m=4, n=2, 4: Poly(butylene succinate-co-butylene adipate (PBSA)

2.3.1.1. Poly(ε-caprolactone) (PCL)

As mentioned earlier, a bioresorbable polymer is a polymer that degrades hydrolytically in living systems such as humans and animals, and whose by-products can be completely eliminated from the body through metabolic pathways [57]. Consequently, aliphatic polymers that are bioresorbable have been very attractive for biomedical applications. The most important reason for attracting such attention is that the scaffolds made of bioresorbable polymers do not require a secondary surgical procedure, which causes significant pain and generates costs, in order to remove the implants after healing.

PCL was one of the earliest aliphatic polyesters being studied by the Carothers group during the 1930s [58]. It can be synthesized either by the condensation of 6-hydroxycaproic (6-hydroxyhexanoic) acid or by the ring-opening polymerization (ROP) of ε-caprolactone (ε-CL) [59]. However, ROP of cyclic monomers such as ε-CL, using various catalysts such as anionic, cationic, and monomer-activated, is a more common method for the synthesis of PCL, the reaction schemes for which are shown in Figure 7.

PCL is a hydrophobic and semi-crystalline linear polymer which belongs to the family of poly(ω-hydroxy esters) and has been approved by the U.S. Food and Drug Administration for use in drug delivery devices, sutures, long-term implants, and adhesion barriers. PCL has a low glass transition temperature (T_g: ~ -60 °C) and a low melting temperature (T_m: ~ 60 °C), and good solubility in many organic solvents. As a consequence, it has long been used for biomedical applications, specifically in drug delivery systems and medical devices [60-62]. Moreover, its good processibility is another advantage over other polymers considered for biomedical applications.

The hydrolytic degradation of polyesters via surface or bulk degradation pathways is a widely accepted phenomenon [63]. The rate of degradation varies depending upon polymer backbone structure, i.e., repeating unit, composition, sequence length, molecular weight, morphology (e.g., crystallinity, size of spherulites, orientation), hydrophilicity, surface area, and additives [64]. The intracellular degradation of PCL has been attributed to random hydrolytic chain scission of the ester linkages, causing a decrease in molecular weight, followed by uptake by phagosomes of macrophages, giant cells and by fibroblasts

[65]. The degradation mechanism of PCL is shown in Figure 2.7. The hydrolysis intermediates are degraded to 6-hydroxycaproic acid and converted to acetyl coenzyme A, which enters the citric acid cycle and is eliminated from the body [66].

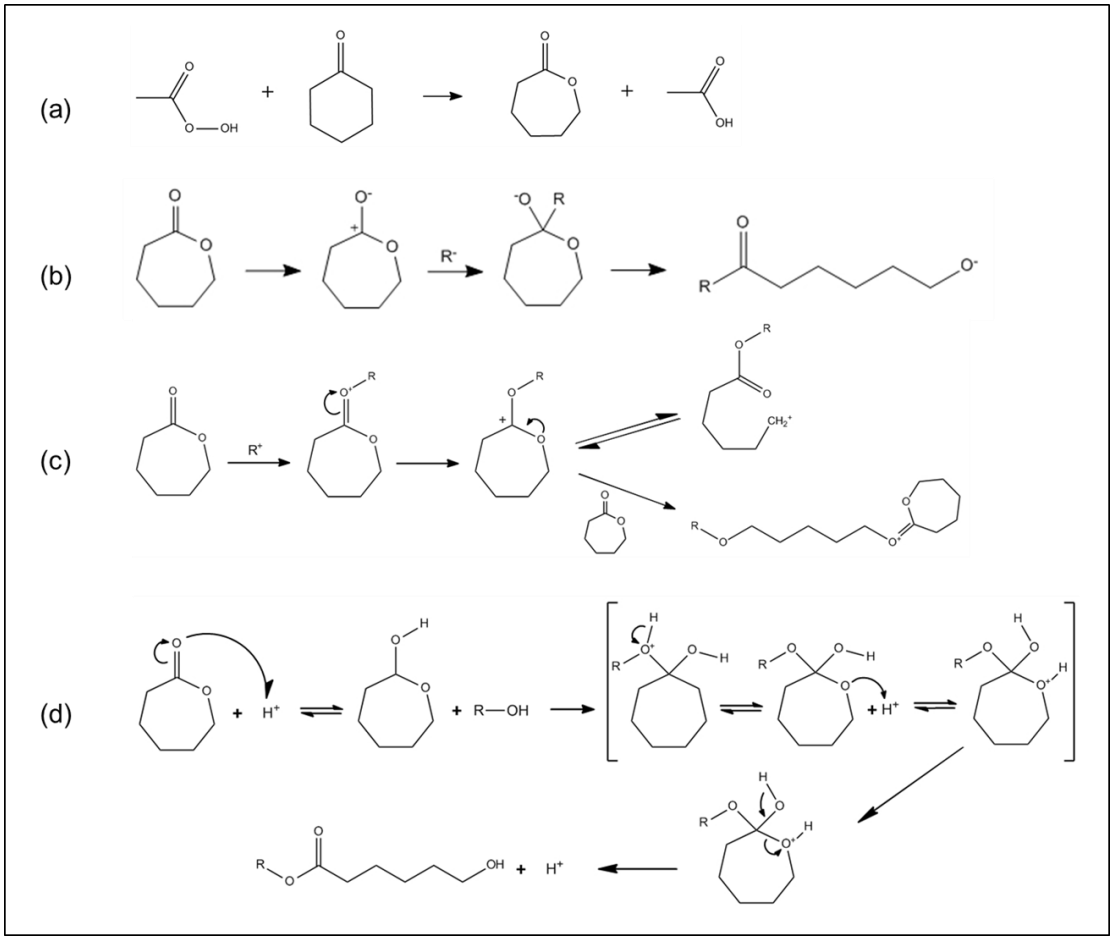

Figure 2.6. Production of ε-caprolactone from cyclohexanone [67] (a) and mechanism of the initiation step for anionic [68] (b), cationic [68, 69] (c), and monomer-activated [70] (d) ring-opening polymerization of PCL. Labet, M. and W. Thielemans, *Synthesis of polycaprolactone: a review.* Chemical Society Reviews, 2009. 38(12): p. 3484-3504 [59]. Used under fair use, 2015.

The degradation of PCL is much slower (> 24 months) than that of other bioresorbable polyesters such as PLA, PGA, and their copolymers [63]. For some tissue engineering applications, a faster degradation is necessary. However, rapid degradation can also cause inflammatory reactions *in vivo* because of the acidity of the degradation by-products [71]. Sanchez *et al.* [72] have identified several by-products of PCL degradation, including succinic, butyric, valeric, and caproic acids (pK_a: 4.88). As a consequence, PCL is more suitable for implantable medical devices that require long-term performance, such as bone scaffolds and controlled release devices, where the polymer resorbed slowly by the body without generating an acidic environment. In such cases, PCL is more attractive than other bioresorbable polymers because of its slow degradation *in vivo*. There are several studies on PCL-based scaffolds that fulfill the requirements of bone tissue engineering which will be discussed later. However, PCL has been rarely studied in load-bearing applications that require strong mechanical properties. In spite of several efforts, it is a still difficult and challenging issue to improve the relatively poor mechanical properties of PCL in bone scaffolds.

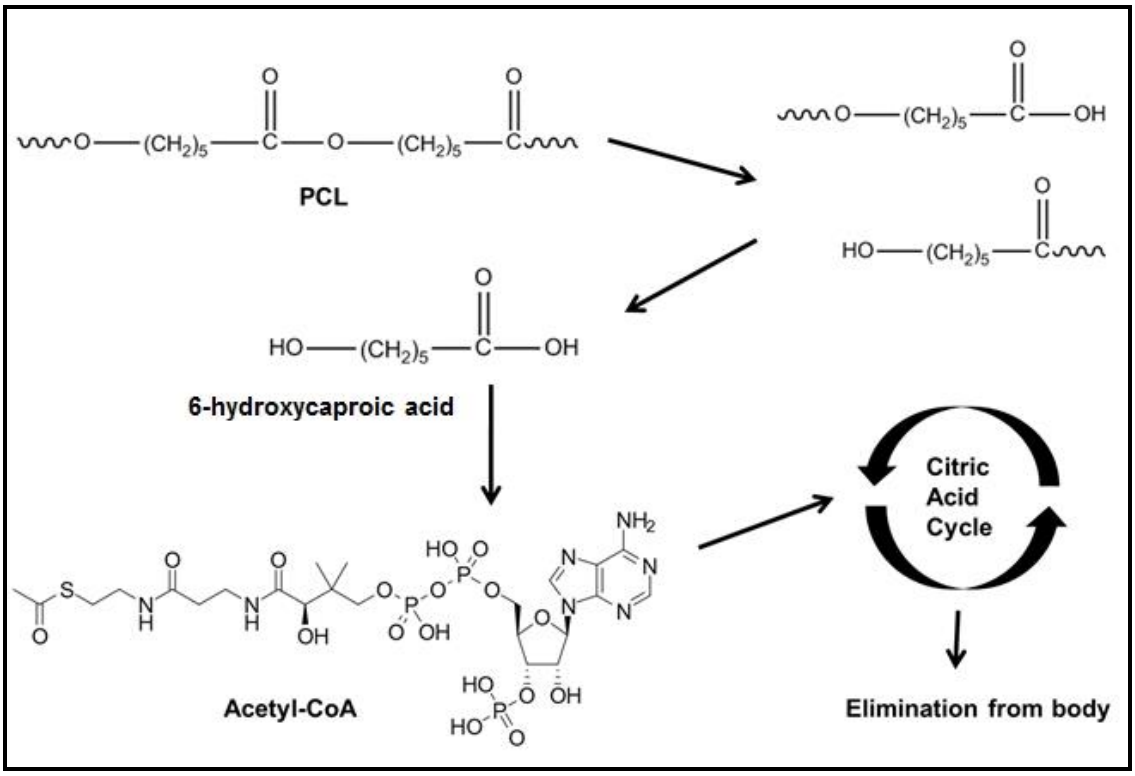

Figure 2.7. The degradation mechanism of PCL via hydrolysis. Woodruff, M.A. and D.W. Hutmacher, *The return of a forgotten polymer—Polycaprolactone in the 21st century.* Progress in Polymer Science, 2010. 35**(10): p. 1217-1256 [63]. Used under fair use, 2015.**

2.3.2. Natural polymers

Besides synthetic polymers, natural polymers, such as proteins and polysaccharides have also been widely used in biomedical applications. They can be derived either from plant or animal sources and the most common natural polymers are collagen, gelatin (denatured collagen), silk, and the polysaccharides, such as cellulose, chitosan, alginate, starch, and hyaluronic acid. Among other things, the biocompatibility and support of cellular functions (e.g., cell adhesion, proliferation, and differentiation) of

polysaccharide-based polymers make them good candidates for tissue engineering applications [73]. Several investigations have shown enhanced osteoinduction and osteoconduction properties of polysaccharides, such as chitosan- [74-78], alginate-[79-81], and starch-based [82-84] materials, in bone tissue engineering applications. In general, however, natural polymers do not provide enough mechanical stability to stand alone as bone scaffolds [85]. The insufficient mechanical properties make the use of both synthetic and natural polymers as load-bearing scaffold materials difficult and it is a critical challenge that must be addressed.

2.3.2.1. Cellulose and cellulose nanocrystals (CNCs)

Cellulose-based materials and cellulose derivatives have been widely used in various areas for centuries. Cellulose is one of the most common organic compounds and attractive renewable resources found in living organisms, such as plants, animals, and bacteria. It is a polysaccharide and a high-molecular weight linear homopolymer consisting of repeating β-D-glucopyranosyl units linked by (1→4)-glycosidic linkages, as shown in Figure 9.

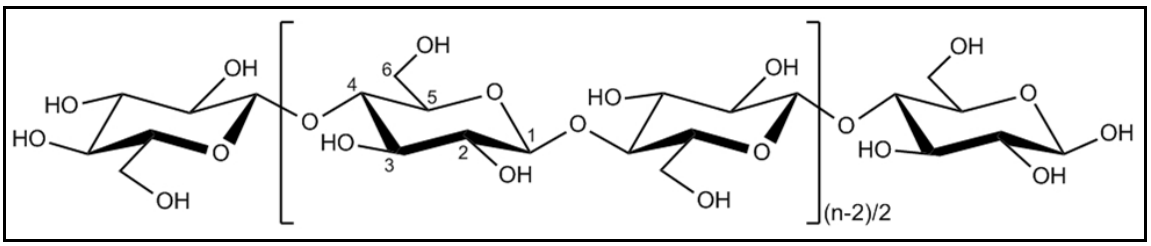

Figure 2.8. Molecular structure of cellulose.

Cellulose chains are organized via intra- and intermolecular hydrogen bonding that assembles the chains firmly in the form of a microfibril. Because of the strong hydrogen bonding interactions, cellulose exhibits relatively high tensile moduli (e.g., up to 800 MPa [86, 87]) relative to other polysaccharides. The structure of a microfibril can be divided into two distinct regions, highly ordered (crystalline) and less ordered (non-crystalline or amorphous) regions. The non-crystalline (or amorphous) regions of cellulose are susceptible to acid-catalyzed cleavage, and thus breakdown into individual crystalline domains, called CNCs. The average dimensions of CNCs (from plant source) are 5-70 nm in diameter and 100-250 nm in length [88]. Also, the mechanical properties of CNCs are significantly higher than those of microfibrils. Several studies have been performed to measure the mechanical properties of CNCs and the obtained results for elastic modulus were in the range of 50 to 220 GPa, depending on the cellulose source, measurement technique, and preparation method [89-91].

It is well known that CNCs can be prepared either by sulfuric acid or by hydrochloric acid hydrolysis. The chemical and physical properties of CNCs vary with the hydrolysis conditions (e.g., acid type, acid concentration, reaction temperature, and reaction time) and the cellulose source used [92]. For example, sulfuric acid hydrolysis introduces sulfate groups to the surface of the CNCs through the esterification of hydroxyl groups. These negatively charged CNCs form stable aqueous colloidal suspensions because of the electrostatic stabilization via the attraction/repulsion forces of electrical double layers [93].

For biomaterials, one of the most important requirements in biomedical applications is biocompatibility. In the literature, the biocompatibility of cellulose-based materials has been reported as promising for tissue engineering application [94-99]. Therefore, they have been studied in various fields of tissue engineering, such as membrane design [100-104], liver [105, 106] and pancreas [107] tissue engineering, wound healing [108, 109], and bone regeneration [95, 110, 111]. Recently, for example, disc-electrospun nanofiber webs using cellulose acetate butyrate have been shown to enhance cellular growth [112]. Also, the low water solubility of cellulose-based materials enables them to maintain their original shape in scaffolds contrary to other polysaccharides [113]. Improved biomineralization and mechanical properties have been reported for scaffolds composed of bacterial cellulose fibers and $CaCO_3$ particles [114].

In summary, natural polymers, such as cellulose, have great advantages given their sustainable and inherent biocompatible nature whereas bioresorbable polymers provide excellent processibility, tunability, and biocompatibility. However, the lack of mechanical stability of both synthetic and natural polymers limits their applications in hard tissue engineering devices, such as bone scaffolds, such as bone scaffold. Because of the significantly better mechanical properties of nanoscale materials, compared to those of bulk materials, bio-based nanofillers derived from natural polymers (e.g., CNCs) may be able to overcome this issue by enhancing the mechanical properties and functions of bioresorbable polymer matrices through a reinforcing effect.

2.4. Design of polymeric bone scaffolds

Scaffolds are the major components of the bone tissue engineering approach. The design of scaffolds is of utmost importance because it is closely related to scaffold performance. Materials and structural configurations are critical criteria for the design of scaffolds and should be carefully considered in order to optimize the performance in targeted applications. As discussed above, scaffolds used in bone tissue engineering applications are evaluated on the basis of several criteria, including 3D structure, mechanical stability, pore size, interconnectivity of pores, and cell adhesion. The main requirement for the scaffold is that it supports bone tissue regeneration through osteoconduction, osteoinduction, and/or osseointegration.

The main goal of this project is to design polymeric scaffolds for critical-sized bone defects. By definition, a critical-sized bone defect is the smallest tissue defect that will not completely heal over the lifespan of an animal and will not heal without intervention [115-117]. Thus, the mechanical stability of a scaffold, which is largely affected by the choice and configuration of the material, is a key parameter in the repair of critical-sized defects, which require long-term performance of the scaffolds during tissue regeneration.

2.4.1. Bio-based polymeric nanocomposites

Over the last few decades, the use of nanomaterials as reinforcing additives has been attracting attention in many research areas for various applications because of the unique properties imparted to the material at the nanoscale. In particular, nanomaterials have

been widely used in biomedical fields, such as drug/gene delivery and tissue engineering [118-121]. As scaffold materials, bio-based polymeric nanocomposites could compensate for the shortcomings of bioresorbable polymers, such as poor mechanical properties and lack of biomineralization (bioactivity), by incorporating naturally derived nanoparticles as reinforcing additives. In order to offer the desired properties, however, polymeric nanocomposites must have favorable interparticle and filler-matrix interactions. Compared to the traditional composites with conventional filler materials, nanocomposites can offer similar or improved properties, specifically tensile strength, stiffness, toughness, and heat deflection temperature, at significantly lower filler loading levels. The enhanced mechanical properties of polymeric nanocomposites are mainly due to the high interfacial area (hundreds of m^2/g of materials) of stiffer nanoparticles (fillers), aspect ratio, and interparticle distance of the nanoparticles [122]. In the case of elongated nanoparticles, percolation above a threshold fraction of the nanoparticles plays a significant role in the formation of a rigid network [122]. The threshold fraction depends strongly upon the shape factor and dispersion of nanoparticles [122]. Theoretically, percolation is a statistical concept that refers to lattice models of the long-range cluster formation of interconnected particles in random systems. The critical concentration for the onset of connectivity is usually defined as the percolation threshold [123].

One area of particular interest in this project is the development of bioresorbable polymer-based nanocomposites with naturally derived nanoparticles, CNCs, for bone scaffolds. However, many of the naturally derived nanoparticles (e.g., polysaccharide-

based nanoparticles) have hydrophilic groups (e.g., hydroxyl, carboxyl, and amino groups) while bioresorbable polymers (e.g., aliphatic polyesters) exhibit a relatively hydrophobic nature. Thus, it is difficult to achieve a homogeneous or adequate dispersion of the hydrophilic nanoparticles in the hydrophobic polymeric matrix. This lack of homogeneity can lead to undesirable properties, such as particle aggregation and phase separation. In the following sections, bio-based polymeric nanocomposites for bone scaffolds with enhanced mechanical properties and biomineralization through the use of nanoparticles are discussed.

2.4.1.1. Mechanical properties

As mentioned earlier, bone responds to its surrounding environment and physiological changes by remodeling (i.e., bone resorption or formation) throughout life. Therefore, it is an important design criterion that the scaffolds possess mechanical properties similar to those of the natural bone tissue around the defect sites. A mechanical mismatch between the scaffold and surrounding bone tissue could induce bone resorption (by a stress shielding effect) or failure of the scaffolds at the defect sites [124, 125].

Despite numerous efforts to improve the mechanical properties of bioresorbable polymers, it is still a daunting task to mimic natural bones, especially with highly porous structures. One feasible approach to address this issue may be to utilize the characteristics of nanocomposites. Several studies have reported mechanical enhancement of bioresorbable polymers by either inorganic or organic nanoparticles.

HA, for instance, has been widely used in bone scaffold materials not only because of its high compressive strength but also because of its good biocompatibility. More importantly, the structural similarity between HA and the minerals found in natural bone, i.e., carbonated HA, suggests osteoconductive properties as well as enhanced bone formation [126, 127]. Nano- and micro-HA/poly(L-lactic acid) (PLLA) composite scaffolds with high porosity (> 90%) and pore sizes from 50 to 500 μm were prepared using thermally induced phase separation techniques [128]. The compressive modulus of the PLLA scaffolds (4.3 MPa) was improved to 8.3 MPa by a nano-HA content of 50% [128]. More recently, porous poly-D-L-lactide (PDLLA) composite scaffolds filled with different amounts of nano-HA (0, 20, 40, 60 wt %) were fabricated by a technique combining polymer coagulation, cold compression molding, and salt leaching [129]. A nano-HA content of 60 wt % increased the compressive modulus of the unfilled PDLLA scaffolds from 51.6 ± 4.7 MPa to 91.3 ± 1.2 MPa [129]. Interestingly, however, another study with the lower nano-HA contents (0, 5, 10, 20 wt %) in a PCL matrix produced somewhat different results [130]. The scaffolds were prepared by a mixed particle leaching and freeze extraction process and the obtained scaffolds had porosities around 88 % with pore sizes of <10 μm and 200-400 μm. The compressive modulus of PCL scaffolds (0.55 ± 0.12 MPa) was highest at the nano-HA content of 10 wt % (1.11 ± 0.19 MPa) and decreased to 0.71 ± 0.10 MPa with a nano-HA content of 20 wt %. PCL-based bone scaffolds containing a nano-HA (0, 0.5, 1 wt %) were also fabricated by electrospining and the obtained scaffolds had pore sizes and porosities of 4.7-5.6 μm and 82-86%, respectively [131]. The tensile strength of the scaffolds was improved from 2.84 ± 0.51 MPa at 0 wt % to 3.93 ± 0.05 MPa at 1 wt %.

However, the mechanical properties of nano-HA containing polymer nanocomposite scaffolds fabricated by 3D printing techniques, which may be better because of well-controlled pore size and shape compared to those achieved by other techniques have seldom been reported. A possible reason could the difficulty of processing with HA [132]. Also, many studies focused only on a specific type of mechanical test (i.e., compression test), which may be due to the limitations of HA, such as low fracture toughness and inherent brittleness, for its load-bearing applications. In spite of those limitations, many studies have reported the use HA as filler for bone scaffold applications since it exhibits good osteoconductive and bone forming properties as well as bonding ability with surrounding bone tissues [128, 133-135].

In recent years, carbon nanotubes are also widely studied for biomedical applications, including nanoscale fillers for mechanical enhancement. For example, Mikos' group has reported poly(propylene fumarate) (PPF)-based nanocomposite scaffolds filled with carbon nanotubes for bone tissue engineering applications [136-138]. They observed a significant improvement in the compressive modulus (74% increase) and flexural modulus (69% increase) of PPF nanocomposites with functionalized single-walled carbon nanotube (SWNT) at a 0.05 wt % loading [136]. At a loading level of 0.1 wt %, the compressive and flexural moduli were increased 3-fold [137]. Later, the group produced PPF-based nanocomposite scaffolds filled with ultra-short SWNT (0.5 wt % and 0.83 wt %), fabricated by a thermal-crosslinking particulate-leaching technique, with porosities of 75, 80, 85, and 90 vol% [138]. The mechanical properties of the scaffolds

were higher than or similar to the corresponding properties for the PPF matrix and higher porosity significantly decreased the overall mechanical properties of the scaffolds [138]. Another recent study demonstrated the mechanical enhancement of PCL-based nanocomposite scaffolds through addition of multiwall carbon nanotubes (MWNT) [139]. The MWNT (0.25-2 wt %)/PCL nanocomposite scaffolds were fabricated by a solution evaporation technique. The compressive modulus was increased by 54.5% with respect to that of pure PCL samples. The compressive modulus of MWNT/PCL nanocomposite scaffolds ranged from 340 to 400 MPa which is in the lower range of the values reported for human trabecular bone [139].

Lastly, we will discuss a promising class of nanoparticles produced from sustainable natural sources, namely polysaccharide-based nanoparticles. Although many studies have attempted to incorporate polysaccharide-based nanoparticles (derived from, e.g., cellulose, starch, chitin, and so on.) into bioresorbable polymers, this approach has rarely been reported for bone tissue engineering applications (e.g., 3D porous structures for bone scaffolds) that require mechanical enhancement. However, such nanocomposites could be used for bone scaffold applications in the near future.

In general, nanoparticles derived from cellulose and chitin exhibit rod-like morphologies, whereas starch nanoparticles are plate-like particles [140]. Since the percolation threshold depends strongly on the aspect ratio of the particles, rod-like particles, which have higher aspect ratios, provide better mechanical reinforcing effects in polymer matrices. Among

polysaccharide-based nanoparticles, CNCs have drawn significant interest as nano-fillers for mechanical reinforcement of polymer matrices [140].

Dufresne and coworkers have studied PCL-based nanocomposites filled with CNCs [141-143]. The group compared the mechanical properties of nanocomposite films containing both unmodified and PCL-grafted CNCs fabricated by the casting/evaporation technique [141, 143]. The addition of PCL-grafted CNCs to the PCL matrix significantly improved the tensile modulus of the nanocomposite films, from 230 MPa at 0 wt % filler loading to 585 MPa at 40 wt %, but unmodified CNCs achieved a maximum value of 338 MPa at 20 wt % filler loading, decreasing to 253 MPa at 30 wt % [143]. The dispersion of the PCL-grafted CNCs in the PCL matrix was better than that of the unmodified CNCs, resulting in more effective reinforcing effects probably by inhibiting aggregation or phase separation that could occur in to the unmodified CNCs. In addition, the thermoformability of the PCL-grafted CNCs nanocomposite was verified by compression molding and injection molding [142]. The tensile modulus of the nanocomposite prepared by compression molding followed by an injection molding process was greatly enhanced by ca. 230%. The authors claimed that the "graft from" strategy contributed to long and dense "plasticizing" tails of PCL on the CNCs surface, which were the key for thermoforming [142].

Over the past few decades, CNCs have been widely studied as reinforcing fillers in polymer matrices because of their superior mechanical properties as well as high surface area-to-volume ratios [87, 144-148]. Concerning bioresorbable polymers such as

hydrophobic aliphatic polyesters, for biomedical applications, a homogeneous dispersion of the hydrophilic nanoparticles containing hydroxyl, carboxyl, and amino groups, in the polymer matrix is critically important to achieve mechanical reinforcement of the resulting nanocomposites. Several methods have been reported for improvement of the dispersion of CNCs in polymer matrices during processing of the nanocomposites. For example, CNCs were transferred from an aqueous to a nonaqueous system (i.e., organic media) [149-152] to increase the compatibility during mixing process. Also, surface modification [147, 153], grafting-onto [141, 154], and grafting-from [143] approaches have been applied. For applications in the biomedical field, however, one must be careful not to use using toxic chemicals (e.g., organic solvents) during those processes, so that the final products contain no residual chemicals that can cause serious side effects in the body.

2.4.1.2. Biomineralization (bioactivity)

Biomineralization is the complex process by which organisms form minerals [39]. It is important to understand the process for the development of scaffold materials in bone tissue engineering applications because this phenomenon is closely associated with bone formation (osteoconduction) ability of the scaffolds *in vivo*.

The mineralization process requires several factors including supersaturated solutions, nucleating conditions, and growth control developers (inductors and inhibitors) [155]. One should, however, keep in mind that mineralization of bone (see section 2.1.2. bone cells, formation, and mineralization) only occurs if bone-forming cells (osteoblasts) and

other biological factors are intimately involved and regulated properly in the body which is a very complex process to mimic. As a prerequisite for further considerations (i.e., *in vivo* implantation), therefore, the ability of a biomimetic bone scaffold to induce mineralization has been extensively investigated *in vitro*. To date, a large amount of work has been performed on *in vitro* mineralization, specifically HA formation on bone scaffold materials. Even though the *in vitro/in vivo* correlation is not well established, they may help to understand the process or mechanism of bone mineralization in development of a better scaffold material or system for bone tissue regeneration.

The major component of the inorganic phase of bone is a calcium phosphate mineral, called HA ($Ca_{10}(PO_4)_6(OH)_2$), that is a type of apatite containing OH^- with very specific features such as stoichiometry, composition, and crystallinity [156, 157]. Since the first structural identification of the calcium phosphate mineral in bone was made by X-ray diffraction in 1926 [158], a significant amount of research has been performed in various scientific fields from different points of view. Consequently, it is now well established that there are distinct differences in structure and chemical composition between HA forms on the basis of their origin, such as geological HA, synthetic HA, and bone apatite crystals [159]. Furthermore, the Ca/P molar ratio of bone apatite crystals differs from the stoichiometric HA ratio of 1.67 because of various substitutions and vacancies [160]. Such variations of bone apatite crystals could be caused by different locations within the bone tissues, age, health status, and physiological changes that occur because bone has a capacity to adapt to environmental conditions by remodeling its mass, shape, and properties throughout life [37].

From a tissue engineering perspective, on the other hand, materials used for bone scaffolds should be designed to promote tissue regeneration. Therefore, it is immensely important to understand the mechanism by which mineralization, and specifically HA (or calcium phosphate mineral) formation, occurs on the scaffolds in order to fabricate better materials for bone tissue engineering applications. Although for several decades a significant amount of research has focused on the process of calcium phosphate formation, the matter is still under debate. Nevertheless, the many studies have done much to advance our understanding of the mechanism of calcium phosphate formation.

In 1975, Posner *et al.* [161] proposed that the $Ca_9(PO_4)_6$ cluster is the transient solution precursor of an amorphous calcium phosphate (ACP), and the clusters rearrange into the HA configuration, taking up OH^- and Ca^{2+} in the process. Similarly, Onuma *et al.* [162] claimed a cluster growth model for HA formation in simulated body fluid. In other studies, it has been proposed that ACP is formed first and the transformed into octacalcium phosphates (OCP) as a transient phase, which is then hydrolyzed to form carbonated HA, such as that found in the mineral phase of mature bone [163-165]. Several recent studies also supported the above proposed mechanism or process, i.e., that the formation of calcium-based biominerals proceeds through a pre-nucleation cluster or an ACP that is subsequently transformed into an apatite crystal [159, 166-169].

In addition, Dey *et al.* demonstrated the process of HA mineralization through the role of pre-nucleation clusters by surface-induced calcium phosphate crystallization [170]. The

proposed mechanism is shown in Figure 2.9. A similar study has been reported previously in which archidic acid ($CH_3(CH_2)_{18}COOH$) monolayers with carboxyl groups, prepared by the Langmuir-Blodgett method on substrates, acted as a nucleation center for HA formation [171].

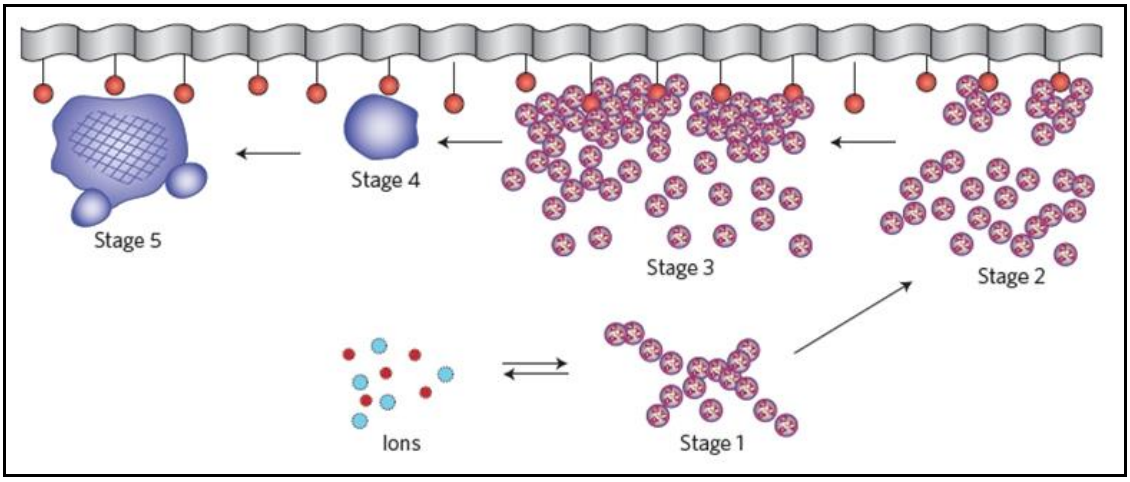

Figure 2.9. Schematic diagram of surface-directed mineralization of calcium phosphate in simulated body fluid at 37 °C. Stage 1: loose aggregation of pre-nucleation clusters in equilibrium with ions in solutions. Stage 2: pre-nucleation clusters aggregate in the presence of the monolayer with loose aggregates still present in solution. Stage 3: aggregation leads to densification near the monolayer. Stage 4: nucleation of amorphous spherical particles only at the monolayer surface. Stage 5:development of crystallinity following the oriented nucleation directed by the monolayer. Dey, A., et al., *The role of prenucleation clusters in surface-induced calcium phosphate crystallization.* Nature Materials, 2010. 9(12): p. 1010-1014. Colfen, H., *Biomineralization a Crystal-Clear View.* Nature Materials, 2010. 9(12): p. 960-961 [170, 172]. Used under fair use, 2015.

From the studies above, it is noteworthy that not only the solution chemistry in terms of ion activity but also the surface chemistry of the substrate impact both the nucleation/growth of biominerals and the supersaturation of the growth environments during the mineralization process [39]. In a sense, though, the surface chemistry of scaffold materials seems to have a greater impact on developing better materials for bone tissue engineering in terms of biomineralization (bioactivity or osteoconductivity). In order to evaluate the mineralization ability of biomimetic bone scaffold materials *in vitro*, the mineralization process must be carefully controlled by considering several key factors such as solubility, supersaturation, and energetics, which affect the structure and chemical composition of apatite [36].

In an effort to provide an environment that resembles the human body, simulated body fluid (SBF) containing ion concentrations similar to those of the inorganic constituents of human blood plasma was first used by Kokubo *et al.* [173]. Since then, SBF has been commonly used to reproduce or mimic the biological environment in *in vitro* mineralization studies evaluating the mineralization ability of various substrates, and a series of different SBF formulations, shown in Table 2.5, have been reported [156, 173-176].

Table 2.5. Total ion concentrations (mM) of human blood plasma and SBFs. Kokubo, T. and H. Takadama, *How useful is SBF in predicting in vivo bone bioactivity?* Biomaterials, 2006. 27(15): p. 2907-2915 [174]. Used under fair use, 2015.

	Na^+	K^+	Mg^{2+}	Ca^{2+}	Cl^-	SO_4^{2-}	$H_2PO_4^-$	HCO_3^-	pH
Human blood plasma	142.0	5.0	1.5	2.5	103.0	0.5	1.0	27.0	7.2-7.4
Original SBF	142.0	5.0	1.5	2.5	147.8	0.5	1.0	4.2	7.4
Revised SBF	142.0	5.0	1.5	2.5	103.0	0.5	1.0	27.0	7.4
Newly improved SBF	142.0	5.0	1.5	2.5	103.0	0.5	1.0	4.2	7.4

Recently, Kokubo and Takadama reviewed correlations between apatite formation on the surface of various materials in SBF (*in vitro*) and their *in vivo* bioactivity [174]. They concluded that there is no correlation between apatite formation in SBF with several concentration levels (e.g., 1.5x SBF) and its *in vivo* mineralization on a material, whereas the results obtained using 1x SBF correlated well with *in vivo* bioactivity [174]. This last point is crucial for the successful development of new bioactive bone scaffold materials on the basis of predictions from apatite formation on their surfaces in SBF. Although numerous studies using SBF with several-fold concentrations have reported that HA formation with a Ca/P ratio of ~1.67 on the proposed bone scaffold materials occurs during *in vitro* biomimetic mineralization, it must be pointed out that the use of such fluids does not allow conclusions with regard to the ability of biomineralization or bioactivity of the bone scaffold materials *in vivo*.

Another important aspect that is relevant for developing bone scaffold materials in terms of biomineralization (or bioactivity) is the surface chemistry of the substrate. Biologically, non-collagenous proteins (e.g., osteonectin, osteopontin, osteocalcin, and bone sialoprotein) are believed to play crucial roles in the induction of amorphous and liquid-phase mineral precursors of the biomineralization process [177]. Also, these proteins contain anionic residues (e.g., polysapartic acid and polyglutamic acid), which have a high affinity for calcium ions due to the prevalence of carboxyl groups [178, 179]. Consequently, several functional groups (e.g., carboxylic acid, sulfate and phosphate groups) have been incorporated into natural and synthetic polymers to develop a biomineralizable (bioactive) material for bone tissue engineering [36].

Tanahashi *et al.* [180] examined the growth rate of apatite formation on self-assembled monolayers (SAMs) with different terminal functional groups in SBF (Figure 2.10). The most potent functional group for apatite formation was the negatively charged -PO_4H_2 followed by the -COOH group. However, nonionic groups ($CONH_2$ and OH) and a positively charged group (NH_2) showed weaker nucleating ability, and it was found that apatite formation was inhibited on CH_3-terminated SAMs. These findings indicate that, surface modification is a good strategy for enhancing the biomineralization ability of polymer-based bone scaffold materials. In our research, on the other hand, one of the main areas of focus is the potential use of CNCs as a multi-functional additive in bone tissue engineering. We hypothesize that the poor biomineralization ability (bioactivity) of PCL can be improved by addition of surface modified CNCs. The formation and growth rate of apatite for different functional groups increases in the order $CONH_2$ < COOH <

PO_4H_2 and CH_3 < NH_2 < OH [180]. Although phosphate functional groups can be introduced into cellulose through phosphorylation using phosphoric acid (H_3PO_4) and phosphorus pentaoxide (P_2O_5) [181, 182], crosslinking and gel formation render the introduction of these groups difficult (Figure 2.11). Therefore, the –COOH group was chosen for this research to accelerate the apatite nucleation on CNCs.

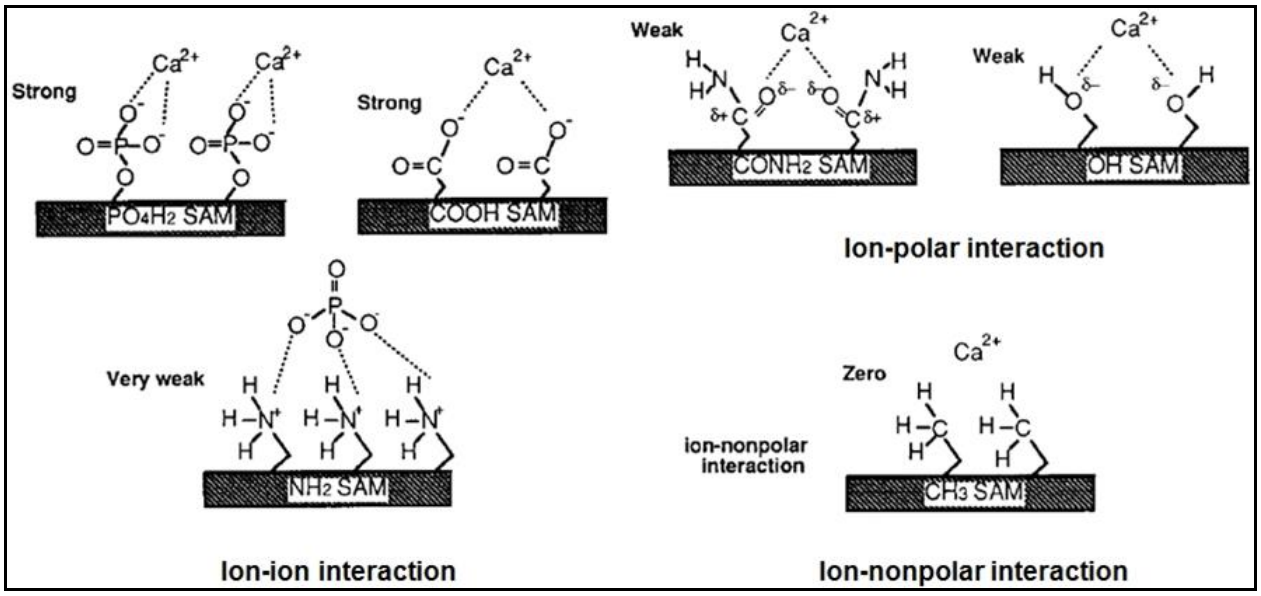

Figure 2.10. Various interaction modes between calcium phosphate ions and surface functional groups as an initial step for apatite formation. Tanahashi, M. and T. Matsuda, *Surface functional group dependence on apatite formation on self-assembled monolayers in a simulated body fluid.* Journal of biomedical materials research, 1997. 34(3): p. 305-315 [180]. Used under fair use, 2015.

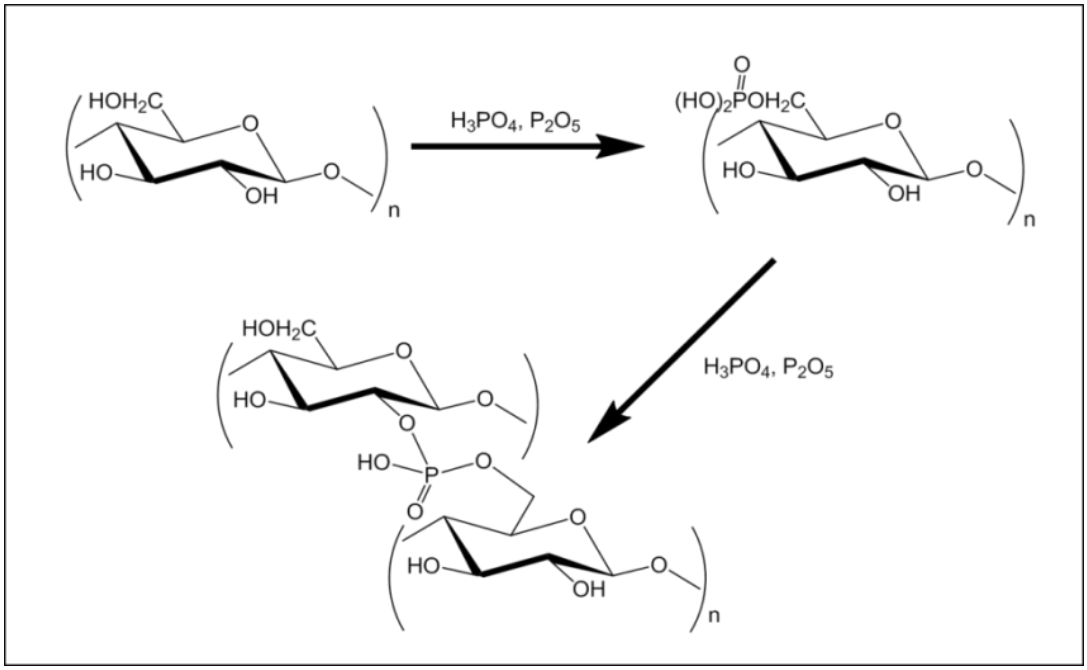

Figure 2.11. Mechanism of cellulose phosphorylation.

2.4.2. Fabrication techniques of three dimensional (3D) porous scaffolds

In addition to the choice of materials, the porosity and architecture of scaffolds are important because they profoundly influence metabolite transportation, cell ingrowth, and vascularization by providing spatial organization composed of structural elements [51, 183]. The structural characteristics, including pore size/shape and interconnectivity of pores, in 3D constructions are determined mainly by the fabrication techniques. Furthermore, the mechanical stability of the scaffolds varies with the fabrication techniques, and the pore size/shape and interconnectivity of the pores have inverse relationships with the mechanical stability of the scaffolds [183]. Therefore, ideal scaffolds should be fabricated by striking a balance between the structural elements (pore

size/shape and interconnectivity of pores) and mechanical stability in order to optimize performance of the scaffolds for the desired applications.

The pore sizes within the scaffolds should be carefully controlled and tailored to the application since different pore sizes are required for different cell types and tissue regeneration. For example, it has been reported that the optimum pore size for osteoid development is about 40~100 μm and for bone regeneration about 100-400 μm [184, 185]. Also, Green *et al.* [186] suggested that different pore diameters are required to stimulate fibrovascular growth (15-50 μm) and osteoid formation (50-150 μm), with pores in the range of 150-500 μm leading directly to mineralized bone. In addition to pore size, the interconnectivity of the pores within 3D porous scaffolds dictates the regeneration of specific tissues [187].

The mechanical stability, however, is no less important than the structural elements for hard tissue regeneration, such as bone scaffolds. The inverse relationship between the structural elements and mechanical stability makes 3D porous scaffolds more difficult to design for load-bearing tissue applications. The mechanical properties of both dense and porous materials are shown in Figure 2.12. Although the mechanical properties of scaffolds mainly depend on the materials used, the fabrication method, which can control the pore size/shape and interconnectivity of pores, also contributes significantly to the properties of scaffolds.

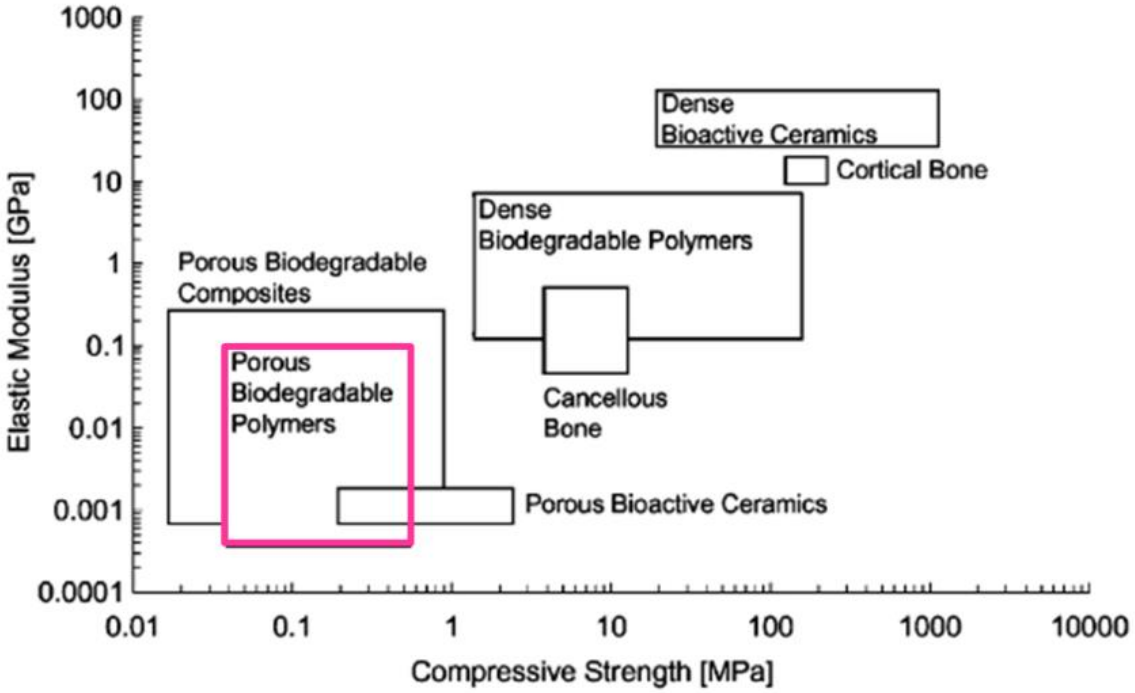

Figure 2.12. Mechanical properties between dense and porous materials. Rezwan, K., et al., *Biodegradable and bioactive porous polymer/inorganic composite scaffolds for bone tissue engineering.* Biomaterials, 2006. 27(18): p. 3413-3431 [188]. Used under fair use, 2015.

A number of fabrication techniques have been developed for the fabrication of 3D porous structures, and each technique has its benefits and limitations. Some of the common techniques (e.g., solvent-casting and particulate leaching, thermally induced phase separation, gas-forming, fiber bonding, and electrospinning) are briefly introduced here.

Mikos *et al.* [189] developed a solvent casting and particulate leaching method to prepare highly porous poly(L-lactic acid) membranes. In a first step, a leachable porogen, such as salt particles or paraffin spheres, is added to a polymer solution, followed by solvent casting of the mixture. The porogen, which determines the pore size, is then leached out

and leaves pores within the polymer matrix. The advantages of this method are that it is simple and easy to carry out. However, the disadvantages include limited mechanical properties of the resulting scaffolds, heterogeneity of the pores and poor interconnectivity of pores, as well as the presence of residual porogen and solvent [190].

Schungens *et al.* [191, 192] first applied the thermally-induced phase separation technique for PLA scaffolds. They used both solid-liquid phase separation (e.g., poly(D,L-lactide) and poly(L-lactide) in 1,4-dioxane) and liquid-liquid phase separation (e.g., polylactide solutions in an 87/13 dioxane/water mixture) followed by quenching of the mixture at a certain temperature. The technique produces high anisotropy foams with an average pore size of 100 μm and isotropic foams with interconnected pores of 1-10 μm in diameter. The main advantage of this technique is that the porosity (< 97%), diameter, and morphology of the pores, and their orientation can be modified by changing the polymer concentration, solvent system, and temperature gradient [40]. However, the use of organic solvents may lead to potentially toxic residues in the scaffolds.

The gas foaming technique was reported by Mooney *et al.* [193] to produce highly porous scaffolds by the use of high-pressure carbon dioxide at room temperature without the need for organic solvents. The group first saturated a synthetic bioresorbable polymer, poly(D,L-lactic-co-glycolic acid), by exposing to high pressure CO_2 gas for 72 h at room temperature. Thermodynamic instability of the CO_2 dissolved in the polymer resulted in the creation of gas bubbles within the polymer matrix. Porosities of up to 93% and pore

sizes of -100 μm could be achieved using this technique and the porosity could be controlled during the processing [193]. The main drawback of the 3D porous structures fabricated using this method is their poor interconnectivity of pores as well as their non-porous surfaces.

The fiber bonding technique was developed by Cima *et al.* [187]. The group used a PGA fiber-based felt and the fibers were entangled to yield a bilaminated mesh. The fiber-based matrices fit the criteria of high porosity and high surface area per unit volume required by liver, cartilage, and cell transplantation applications, while the scaffolds are poorly suited for load-bearing applications because they provide no structural support [187].

The process of using electrostatic forces to form synthetic fibers has been known for over 100 years. This process, known as electrospinning, utilizes a high voltage source to inject charge of a certain polarity into a polymer solution or melt, which is then accelerated toward a collector of opposite polarity. In 1987, Annis and Bornat published work examining electrospun polyurethane mats for use as vascular prostheses [194]. The electrospinning process affords the opportunity to engineer scaffolds with micro to nanoscale topography and high porosity similar to the natural extracellular matrix (ECM). The inherently high surface-to-volume ratio of electrospun scaffolds can enhance cell attachment, drug loading, and mass transfer properties. By varying the processing and solution parameters, the fiber orientation (aligned vs. random) and porosity/pore size (cell infiltration) of the electrospun scaffold can be controlled and optimized for individual

applications [195]. Although several investigators have evaluated this technique for bone scaffolds [196-199], the mechanical properties of the electrospun mesh were insufficient for load-bearing applications. For example, Thomas et al. [196] investigated the mechanical properties of electrospun PCL scaffolds by changing the processing parameters (e.g., different collector rotation speed) and obtained tensile moduli in the range 2 to 33 MPa.

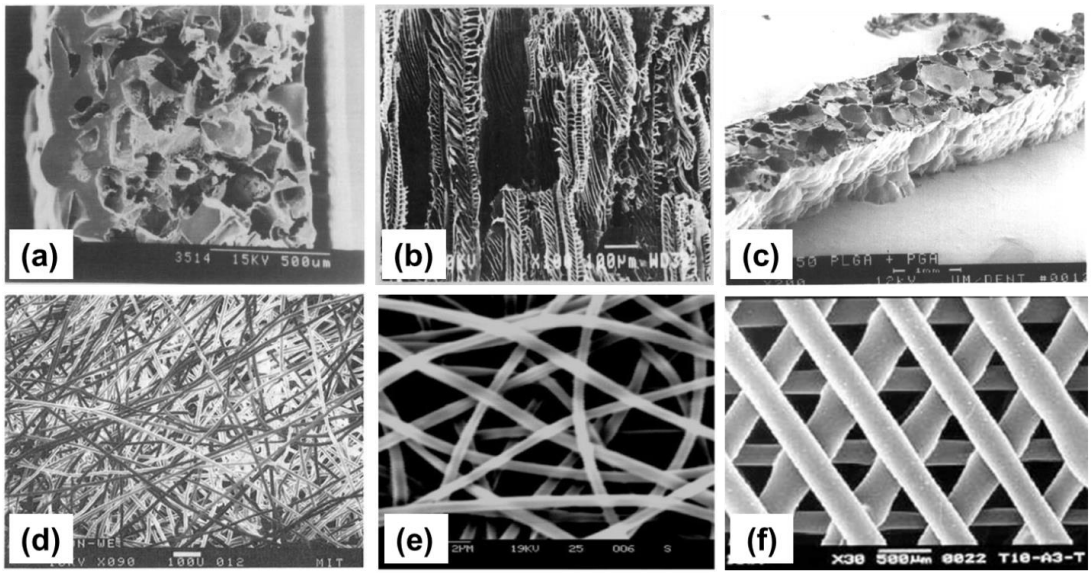

Figure 2.13. 3D porous scaffolds fabricated by different techniques. (a) solvent cast and particulate leaching. Mikos, A.G., et al., *Preparation and Characterization of Poly(L-Lactic Acid) Foams.* Polymer, 1994. 35(5): p. 1068-1077 [189], (b) thermally induced phase separation. Schugens, C., et al., *Polylactide macroporous biodegradable implants for cell transplantation .2. Preparation of polylactide foams by liquid-liquid phase separation.* Journal of biomedical materials research, 1996. 30(4): p. 449-461 [192], (c) gas foaming. Mooney, D.J., et al., *Novel approach to fabricate porous sponges of poly(D,L-lactic-co-glycolic acid) without the use of organic solvents.* Biomaterials, 1996. 17(14): p. 1417-1422 [193], (d) fiber bonding. Cima, L.G., et al., *Tissue Engineering by Cell Transplantation Using Degradable Polymer Substrates.*

Journal of Biomechanical Engineering-Transactions of the Asme, 1991. 113(2): p. 143-151 [187], electrospinning. Sui, G., et al., *Poly-L-lactic acid/hydroxyapatite hybrid membrane for bone tissue regeneration.* Journal of biomedical materials research. Part A, 2007. 82(2): p. 445-54 [197], (f) 3D printing. Zein, I., et al., *Fused deposition modeling of novel scaffold architectures for tissue engineering applications.* Biomaterials, 2002. 23(4): p. 1169-1185 [200]. Used under fair use, 2015.

Consequently, the conventional scaffold fabrication techniques mentioned above do not offer precise control over the structural elements within the scaffold [201]. Scaffolds for critical-sized bone defects require careful control of the pore size/shape, spatial distribution of pores, and construction of internal channels or interconnectivity. Therefore, we will use a different technique, specifically 3D printing, which allows precise control of the necessary parameters in order to improve the mechanical stability of 3D porous scaffolds (Figure 2.13).

2.4.2.1. Three dimensional (3D) printing

3D printing technology was developed and patented by the Massachusetts Institute of Technology in 1993 [202]. However, the first to develop this technology was Charles Hull in 1984, who named it Stereo lithography [203]. Other technologies, including Fused Deposition Modeling and Rapid Prototyping, are based on a similar concept, called Solid Freeform Fabrication, where a 3D object designed using a computer-aided design (CAD program) is built with raw materials, such as metals, ceramics, and polymers, in a layer-by-layer fashion.

In 1998, one of the earliest efforts to fabricate a scaffold for tissue engineering applications using a 3D printing technique was reported by Kim et al. [204]. The group used copolymers of polylactide-co-glycolide (PLGA, 85:15) to fabricate microporous 3D scaffolds with interconnected pores of 800 μm and combined 3D printing with the salt-leaching method to create micro-pores of 45-150 μm. Also, Lam et al. [183] demonstrated that a 3D printing technique can be used to fabricate 3D porous structures with enhanced mechanical properties using a mixture of natural polymers (e.g., cornstarch, dextran, and gelatin) and water-based binder. In comparison with other 3D porous fabrication techniques, current 3D printing techniques allow the fabrication of scaffolds mimicking natural bones with precisely controlled structure, and thus make it possible to customize the scaffold with regard to defect sites (Figure 2.14).

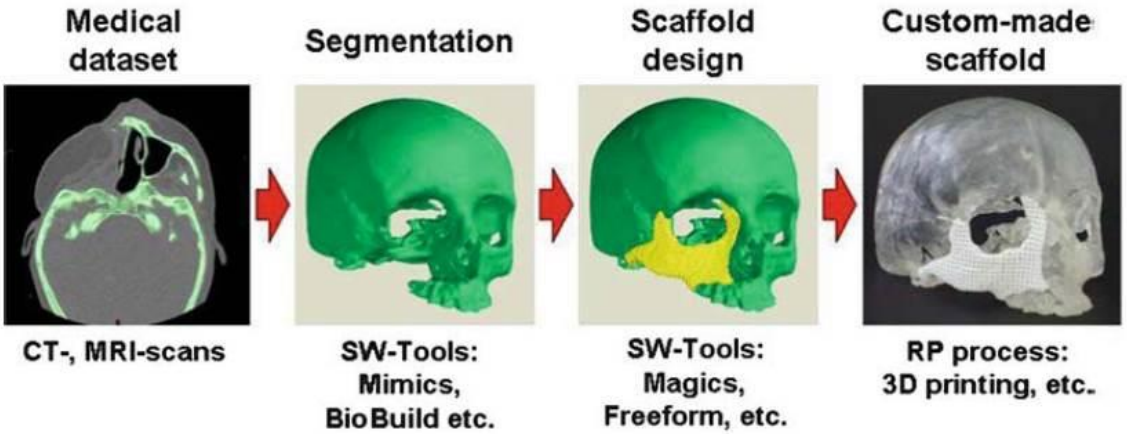

Figure 2.14. 3D printing process for customized bone scaffolds for critical sized defects. Schieker, M., et al., *Biomaterials as Scaffold for Bone Tissue Engineering.* European Journal of Trauma, 2006. 32(2): p. 114-124 [12]. Used under fair use, 2015.

In summary, precise control of scaffold properties, such as pore geometry, size, and interconnectivity, is critical to achieve an optimal environment for bone formation. Although each fabrication technique has benefits for certain materials and targeted applications, 3D printing provides several advantages including accuracy, uniformity, and reproducibility. Thus, 3D-printed PCL/SO-CNC nanocomposite scaffolds presumably will provide better mechanical stability for critical sized bone defects. In addition, the 3D printed scaffolds can be infused with bioresorbable hydrogels to add auxiliary functions, such as osteoinductive properties via encapsulated cells or embedded growth factors, thus providing a more robust approach to bone tissue engineering.

2.5. References

1. Woolf, A.D. and B. Pfleger, *Burden of major musculoskeletal conditions.* Bull World Health Organ, 2003. **81**(9): p. 646-56.

2. Dick, H., et al., *The Bone and Joint Decade 2000–2010.* Acta Orthopaedica, 1998. **69**(3): p. 219-220.

3. Lidgren, L., *The Bone and Joint Decade 2000-2010: An update.* Acta Orthopaedica, 2000. **71**(1): p. 3-6.

4. Joshua J. Jacobs, G.B.J.A., John-Erik Bell, Stuart L. Weinstein, John P. Dormans, Steve M. Gnatz, Nancy Lane, J. Edward Puzas, E. William St. Clair, Edward H. Yelin. *The Burden of Musculoskeletal Diseases in the United States*. Available from: http://www.boneandjointburden.org/.

5. Pleis, J.R. and M. Lethbridge-Cejku, *Summary health statistics for U.S. adults: National Health Interview Survey, 2005.* Vital and health statistics. Series 10, Data from the National Health Survey, 2006(232): p. 1-153.

6. *The Bone and Joint Decade: Global Alliance for Musculoskeletal Health*. Available from: http://bjdonline.org/.

7. *National osteoporosis foundation. Learn about Osteoporosis*. Available from: http://www.nof.org/node/40.

8. *World health organization.*; Available from: http://www.who.int/chp/topics/rheumatic/en/index.html.

9. Kurtz, S.M., et al., *Future Clinical and Economic Impact of Revision Total Hip and Knee Arthroplasty.* J Bone Joint Surg Am, 2007. **89**(suppl_3): p. 144-151.

10. Greenwald, A.S., et al., *Bone-Graft Substitutes: Facts, Fictions, and Applications.* J Bone Joint Surg Am, 2001. **83**(2_suppl_2): p. S98-103.

11. Lewandrowski, K.-U., et al., *Bioresorbable bone graft substitutes of different osteoconductivities: a histologic evaluation of osteointegration of poly(propylene glycol-co-fumaric acid)-based cement implants in rats.* Biomaterials, 2000. **21**(8): p. 757-764.

12. Schieker, M., et al., *Biomaterials as Scaffold for Bone Tissue Engineering.* European Journal of Trauma, 2006. **32**(2): p. 114-124.

13. M. J.Yaszemski, J.B.O., L. Lu, B. L. Currier, *Bone Engineering*. 1 st edition ed. 1994: Em squared, Toronto

14. Hughes, T.B., *Bioabsorbable implants in the treatment of hand fractures - An update.* Clinical Orthopaedics and Related Research, 2006(445): p. 169-174.

15. Lopez-Heredia, M.A., et al., *Rapid prototyped porous titanium coated with calcium phosphate as a scaffold for bone tissue engineering.* Biomaterials, 2008. **29**(17): p. 2608-2615.

16. Simon, J.A., J.L. Ricci, and P.E. Di Cesare, *Bioresorbable fracture fixation in orthopedics: a comprehensive review. Part I. Basic science and preclinical studies.* American journal of orthopedics, 1997. **26**(10): p. 665-71.

17. Simon, J.A., J.L. Ricci, and P.E. Di Cesare, *Bioresorbable fracture fixation in orthopedics: a comprehensive review. Part II. Clinical studies.* American journal of orthopedics, 1997. **26**(11): p. 754-62.

18. Bensaid, W., et al., *A biodegradable fibrin scaffold for mesenchymal stem cell transplantation.* Biomaterials, 2003. **24**(14): p. 2497-2502.

19. Lee, C.H., A. Singla, and Y. Lee, *Biomedical applications of collagen.* International Journal of Pharmaceutics, 2001. **221**(1-2): p. 1-22.

20. Salgado, A.J., O.P. Coutinho, and R.L. Reis, *Bone tissue engineering: State of the art and future trends.* Macromolecular Bioscience, 2004. **4**(8): p. 743-765.

21. Porter, J.R., T.T. Ruckh, and K.C. Popat, *Bone Tissue Engineering: A Review in Bone Biomimetics and Drug Delivery Strategies.* Biotechnology Progress, 2009. **25**(6): p. 1539-1560.

22. Yaszemski, M.J., et al., *Evolution of bone transplantation: molecular, cellular and tissue strategies to engineer human bone.* Biomaterials, 1996. **17**(2): p. 175-185.

23. Baroli, B., *From natural bone grafts to tissue engineering therapeutics: Brainstorming on pharmaceutical formulative requirements and challenges.* Journal of pharmaceutical sciences, 2009. **98**(4): p. 1317-75.

24. R., B., *Anatomy and ultrastructure of bone. In: Favus M, editor. Primer on the metabolic bone diseases and disorders of mineral metabolism.* 1993, Raven Press: New York. p. 3-9.

25. Wilson, O.C., ed. *Bone inspired nanocomposites. In New research on nanocomposites. Edited by Luis M. Krause and Jonas T. Walter* 2008, Nova Science Publishers, Inc.: New York. 57-78.

26. Buckwalter, J.A., et al., *Bone biology. I: Structure, blood supply, cells, matrix, and mineralization.* Instructional course lectures, 1996. **45**: p. 371-86.

27. Buckwalter, J.A., et al., *Bone biology. II: Formation, form, modeling, remodeling, and regulation of cell function.* Instructional course lectures, 1996. **45**: p. 387-99.

28. Sikavitsas, V.I., J.S. Temenoff, and A.G. Mikos, *Biomaterials and bone mechanotransduction.* Biomaterials, 2001. **22**(19): p. 2581-93.

29. Britannica., I.E.; Available from: http://www.britannica.com/EBchecked/media/101316/Longitudinal-section-of-the-humerus-showing-outer-compact-bone-and.

30. Athanasiou, K.A., et al., *Fundamentals of biomechanics in tissue engineering of bone.* Tissue Engineering, 2000. **6**(4): p. 361-381.

31. Giraudguille, M.M., *Twisted Plywood Architecture of Collagen Fibrils in Human Compact-Bone Osteons.* Calcified Tissue International, 1988. **42**(3): p. 167-180.

32. Rho, J.Y., L. Kuhn-Spearing, and P. Zioupos, *Mechanical properties and the hierarchical structure of bone.* Medical Engineering & Physics, 1998. **20**(2): p. 92-102.

33. *U.S. National Institutes of Health.* 2006; Available from: http://training.seer.cancer.gov/anatomy/skeletal/tissue.html.

34. Marks, S.C. and S.N. Popoff, *Bone Cell Biology - the Regulation of Development, Structure, and Function in the Skeleton.* American Journal of Anatomy, 1988. **183**(1): p. 1-44.

35. Summerlee, A.J., *1 Bone formation and development.* 2002.

36. Stupp, S.I., et al., *Biomimetic Systems for Hydroxyapatite Mineralization Inspired By Bone and Enamel.* Chemical Reviews, 2008. **108**(11): p. 4754-4783.

37. Boskey, A.L., *Mineralization of bones and teeth.* Elements, 2007. **3**(6): p. 385-391.

38. Gower, L.B., et al., *Bone structure and formation: A new perspective.* Materials Science & Engineering R-Reports, 2007. **58**(3-5): p. 77-116.

39. Weiner, S. and P.M. Dove, *An overview of biomineralization processes and the problem of the vital effect.* Biomineralization, 2003. **54**: p. 1-29.

40. Ma, P.X. and R.Y. Zhang, *Microtubular architecture of biodegradable polymer scaffolds.* Journal of biomedical materials research, 2001. **56**(4): p. 469-477.

41. Liou, S.-C., et al., *Structural characterization of nano-sized calcium deficient apatite powders.* Biomaterials, 2004. **25**(2): p. 189-196.

42. Kawasaki, K., A.V. Buchanan, and K.M. Weiss, *Biomineralization in Humans: Making the Hard Choices in Life.* Annual Review of Genetics, 2009. **43**: p. 119-142.

43. Anderson, H.C., *Molecular-Biology of Matrix Vesicles.* Clinical Orthopaedics and Related Research, 1995(314): p. 266-280.

44. Anderson, H.C., R. Garimella, and S.E. Tague, *The role of matrix vesicles in*

growth plate development and biomineralization. Frontiers in Bioscience-Landmark, 2005. **10**: p. 822-837.

45. Langer, R. and J.P. Vacanti, *Tissue Engineering.* Science, 1993. **260**(5110): p. 920-926.

46. Williams, D.F., *On the nature of biomaterials.* Biomaterials, 2009. **30**(30): p. 5897-5909.

47. Albrektsson, T. and C. Johansson, *Osteoinduction, osteoconduction and osseointegration.* European spine journal : official publication of the European Spine Society, the European Spinal Deformity Society, and the European Section of the Cervical Spine Research Society, 2001. **10 Suppl 2**: p. S96-101.

48. Frost, H.M., *The Biology of Fracture-Healing - an Overview for Clinicians .1.* Clinical Orthopaedics and Related Research, 1989(248): p. 283-293.

49. Frost, H.M., *The Biology of Fracture-Healing - an Overview for Clinicians .2.* Clinical Orthopaedics and Related Research, 1989(248): p. 294-309.

50. Cohen, S., et al., *Design of synthetic polymeric structures for cell transplantation and tissue engineering.* Clinical materials, 1993. **13**(1-4): p. 3-10.

51. Hutmacher, D.W., *Scaffolds in tissue engineering bone and cartilage.* Biomaterials, 2000. **21**(24): p. 2529-43.

52. Williams, D.F., *On the mechanisms of biocompatibility.* Biomaterials, 2008. **29**(20): p. 2941-2953.

53. Vert, M., et al., *Bioresorbability and Biocompatibility of Aliphatic Polyesters.* Journal of Materials Science-Materials in Medicine, 1992. **3**(6): p. 432-446.

54. Ikada, Y. and H. Tsuji, *Biodegradable polyesters for medical and ecological applications.* Macromolecular Rapid Communications, 2000. **21**(3): p. 117-132.

55. Agrawal, C.M. and R.B. Ray, *Biodegradable polymeric scaffolds for musculoskeletal tissue engineering.* Journal of biomedical materials research, 2001. **55**(2): p. 141-150.

56. Vert, M., *Aliphatic polyesters: Great degradable polymers that cannot do everything.* Biomacromolecules, 2005. **6**(2): p. 538-546.

57. Edlund, U. and A.C. Albertsson, *Degradable polymer microspheres for controlled drug delivery.* Degradable Aliphatic Polyesters, 2002. **157**: p. 67-112.

58. Natta, F.J.v., J.W. Hill, and W.H. Carothers, *Studies of Polymerization and Ring Formation. XXIII.1 ε-Caprolactone and its Polymers.* Journal of the American Chemical Society, 1934. **56**(2): p. 455-457.

59. Labet, M. and W. Thielemans, *Synthesis of polycaprolactone: a review.* Chemical Society Reviews, 2009. **38**(12): p. 3484-3504.

60. Chandra, R. and R. Rustgi, *Biodegradable polymers.* Progress in Polymer Science, 1998. **23**(7): p. 1273-1335.

61. Okada, M., *Chemical syntheses of biodegradable polymers.* Progress in Polymer Science, 2002. **27**(1): p. 87-133.

62. Nair, L.S. and C.T. Laurencin, *Biodegradable polymers as biomaterials.* Progress in Polymer Science, 2007. **32**(8-9): p. 762-798.

63. Woodruff, M.A. and D.W. Hutmacher, *The return of a forgotten polymer—Polycaprolactone in the 21st century.* Progress in Polymer Science, 2010. **35**(10): p. 1217-1256.

64. Holland, S.J., Tighe, B.J., *In: Advances in Pharmaceutical Sciences*. Vol. 6, Chap 4, p 101. 1992: Academic, San Diego, CA.

65. Woodward, S.C., et al., *The Intracellular Degradation of Poly(Epsilon-Caprolactone).* Journal of biomedical materials research, 1985. **19**(4): p. 437-444.

66. Albertsson, A.C., Karlsson, S., *Controlled degration by artificial and biological processes.* 1997. p 739-80.: In: Hatada, K., Kitayama, T., Vogl, O. editors. Macromolecular design of polymeric materials. New York/Basel/Hong Kong, Marcel Dekker Inc.

67. Clark, M.C.R.G.C.A.B.L.D.J.M.J.H., *Process for the oxidation of cyclohexanone to epsilon-caprolactone*. 2003, Solvay.

68. Khanna, A., et al., *Molecular modeling studies of poly lactic acid initiation mechanisms.* Journal of Molecular Modeling, 2008. **14**(5): p. 367-374.

69. Stridsberg, K., M. Ryner, and A.-C. Albertsson, *Controlled Ring-Opening Polymerization: Polymers with designed Macromolecular Architecture*, in *Degradable Aliphatic Polyesters*. 2002, Springer Berlin Heidelberg. p. 41-65.

70. Kim, M.S., et al., *Ring-Opening Polymerization of ε-Caprolactone by Poly(ethylene glycol) by an Activated Monomer Mechanism.* Macromolecular Rapid Communications, 2005. **26**(8): p. 643-648.

71. Bergsma, J.E., et al., *Late Degradation Tissue-Response to Poly(L-Lactide) Bone Plates and Screws.* Biomaterials, 1995. **16**(1): p. 25-31.

72. Sanchez, J.G., A. Tsuchii, and Y. Tokiwa, *Degradation of polycaprolactone at 50 degrees C by a thermotolerant Aspergillus sp.* Biotechnology Letters, 2000. **22**(10): p. 849-853.

73. Khan, F. and S.R. Ahmad, *Polysaccharides and Their Derivatives for Versatile Tissue Engineering Application.* Macromolecular Bioscience, 2013: p. n/a-n/a.

74. Zhang, Y. and M.Q. Zhang, *Three-dimensional macroporous calcium phosphate bioceramics with nested chitosan sponges for load-bearing bone implants.* Journal of biomedical materials research, 2002. **61**(1): p. 1-8.

75. Li, Z.S., et al., *Chitosan-alginate hybrid scaffolds for bone tissue engineering.* Biomaterials, 2005. **26**(18): p. 3919-3928.

76. Cuy, J.L., et al., *Adhesive protein interactions with chitosan: Consequences for valve endothelial cell growth on tissue-engineering materials.* Journal of Biomedical Materials Research Part A, 2003. **67A**(2): p. 538-547.

77. Di Martino, A., M. Sittinger, and M.V. Risbud, *Chitosan: A versatile biopolymer for orthopaedic tissue-engineering.* Biomaterials, 2005. **26**(30): p. 5983-5990.

78. Muzzarelli, R.A.A., et al., *Stimulatory Effect on Bone-Formation Exerted by a Modified Chitosan.* Biomaterials, 1994. **15**(13): p. 1075-1081.

79. Simmons, C.A., et al., *Dual growth factor delivery and controlled scaffold degradation enhance in vivo bone formation by transplanted bone marrow stromal cells.* Bone, 2004. **35**(2): p. 562-569.

80. Alsberg, E., et al., *Cell-interactive alginate hydrogels for bone tissue engineering.* Journal of Dental Research, 2001. **80**(11): p. 2025-9.

81. Alsberg, E., et al., *Regulating bone formation via controlled scaffold degradation.* Journal of Dental Research, 2003. **82**(11): p. 903-8.

82. Salgado, A.J., et al., *Preliminary study on the adhesion and proliferation of human osteoblasts on starch-based scaffolds.* Materials Science and Engineering: C, 2002. **20**(1–2): p. 27-33.

83. Salgado, A.J., O.P. Coutinho, and R.L. Reis, *Novel starch-based scaffolds for bone tissue engineering: Cytotoxicity, cell culture, and protein expression.* Tissue Engineering, 2004. **10**(3-4): p. 465-474.

84. Silva, G.A., et al., *Starch-based microparticles as vehicles for the delivery of active platelet-derived growth factor.* Tissue Engineering, 2007. **13**(6): p. 1259-1268.

85. Shanmugasundaram, N., et al., *Collagen-chitosan polymeric scaffolds for the in vitro culture of human epidermoid carcinoma cells.* Biomaterials, 2001. **22**(14): p. 1943-1951.

86. Bledzki, A.K. and J. Gassan, *Composites reinforced with cellulose based fibres.* Progress in Polymer Science, 1999. **24**(2): p. 221-274.

87. Mohanty, A.K., M. Misra, and G. Hinrichsen, *Biofibres, biodegradable polymers and biocomposites: An overview.* Macromolecular Materials and Engineering, 2000. **276**(3-4): p. 1-24.

88. Klemm, D., et al., *Nanocelluloses: A New Family of Nature-Based Materials.* Angewandte Chemie-International Edition, 2011. **50**(24): p. 5438-5466.

89. Diddens, I., et al., *Anisotropic Elastic Properties of Cellulose Measured Using Inelastic X-ray Scattering.* Macromolecules, 2008. **41**(24): p. 9755-9759.

90. Sturcova, A., G.R. Davies, and S.J. Eichhorn, *Elastic modulus and stress-transfer properties of tunicate cellulose whiskers.* Biomacromolecules, 2005. **6**(2): p. 1055-1061.

91. Rusli, R. and S.J. Eichhorn, *Determination of the stiffness of cellulose nanowhiskers and the fiber-matrix interface in a nanocomposite using Raman spectroscopy.* Applied Physics Letters, 2008. **93**(3).

92. Kargarzadeh, H., et al., *Effects of hydrolysis conditions on the morphology, crystallinity, and thermal stability of cellulose nanocrystals extracted from kenaf bast fibers.* Cellulose, 2012. **19**(3): p. 855-866.

93. Lu, P. and Y.L. Hsieh, *Preparation and properties of cellulose nanocrystals: Rods, spheres, and network.* Carbohydrate Polymers, 2010. **82**(2): p. 329-336.

94. Miyamoto, T., et al., *Tissue Biocompatibility of Cellulose and Its Derivatives.* Journal of biomedical materials research, 1989. **23**(1): p. 125-133.

95. Martson, M., et al., *Biocompatibility of cellulose sponge with bone.* European Surgical Research, 1998. **30**(6): p. 426-432.

96. Martson, M., et al., *Is cellulose sponge degradable or stable as implantation material? An in vivo subcutaneous study in the rat.* Biomaterials, 1999. **20**(21): p. 1989-1995.

97. Bowry, S.K. and T.H. Rintelen, *Synthetically modified cellulose (SMC) - A cellulosic hemodialysis membrane with minimized complement activation.* Asaio Journal, 1998. **44**(5): p. M579-M583.

98. Helenius, G., et al., *In vivo biocompatibility of bacterial cellulose.* Journal of Biomedical Materials Research Part A, 2006. **76A**(2): p. 431-438.

99. Petersen, N. and P. Gatenholm, *Bacterial cellulose-based materials and medical devices: current state and perspectives.* Applied Microbiology and Biotechnology, 2011. **91**(5): p. 1277-1286.

100. Sevillano, G., et al., *Cellulose Acetate Membrane Improves Some Aspects of Red Blood Cell Function in Haemodialysis Patients.* Nephrology Dialysis

Transplantation, 1990. **5**(7): p. 497-499.

101. Burhop, K.E., et al., *Biocompatibility of Hemodialysis Membranes - Evaluation in an Ovine Model.* Journal of Laboratory and Clinical Medicine, 1993. **121**(2): p. 276-293.

102. Chang, Q., et al., *A fluorescence lifetime-based solid sensor for water.* Analytica Chimica Acta, 1997. **350**(1-2): p. 97-104.

103. Kostov, Y., et al., *Membranes for Optical Ph Sensors.* Analytica Chimica Acta, 1993. **280**(1): p. 15-19.

104. Entcheva, E.G. and L.K. Yotova, *Analytical Application of Membranes with Covalently Bound Glucose-Oxidase.* Analytica Chimica Acta, 1994. **299**(2): p. 171-177.

105. Kino, Y., et al., *Multiporous cellulose microcarrier for the development of a hybrid artificial liver using isolated hepatocytes.* Journal of Surgical Research, 1998. **79**(1): p. 71-76.

106. Yang, M.B., J.P. Vacanti, and D.E. Ingber, *Hollow Fibers for Hepatocyte Encapsulation and Transplantation - Studies of Survival and Function in Rats.* Cell transplantation, 1994. **3**(5): p. 373-385.

107. Risbud, M.V. and R.R. Bhonde, *Suitability of cellulose molecular dialysis membrane for bioartificial pancreas: In vitro biocompatibility studies.* Journal of biomedical materials research, 2001. **54**(3): p. 436-444.

108. Cullen, B., et al., *The role of oxidised regenerated cellulose/collagen in chronic wound repair and its potential mechanism of action.* International Journal of Biochemistry & Cell Biology, 2002. **34**(12): p. 1544-1556.

109. Ovington, L.G., *Overview of matrix metalloprotease modulation and growth factor protection in wound healing. Part 1.* Ostomy/wound management, 2002. **48**(6 Suppl): p. 3-7.

110. Katoh, R. and M.R. Urist, *Surface adhesion and attachment factors in bone morphogenetic protein-induced chondrogenesis in vitro.* Clinical Orthopaedics and Related Research, 1993(295): p. 295-304.

111. Takata, T., H.L. Wang, and M. Miyauchi, *Migration of osteoblastic cells on various guided bone regeneration membranes.* Clinical Oral Implants Research, 2001. **12**(4): p. 332-338.

112. Huang, C., et al., *Disc-electrospun cellulose acetate butyrate nanofibers show enhanced cellular growth performances.* Journal of Biomedical Materials Research Part A, 2013. **101A**(1): p. 115-122.

113. Entcheva, E., et al., *Functional cardiac cell constructs on cellulose-based scaffolding.* Biomaterials, 2004. **25**(26): p. 5753-5762.

114. Liu, X., et al., *A Promising Hybrid Scaffold Material: Bacterial Cellulose In-situ Assembling Biomimetic Lamellar CaCO3.* Materials Letters, (0).

115. Schmitz, J.P. and J.O. Hollinger, *The Critical Size Defect as an Experimental-Model for Craniomandibulofacial Nonunions.* Clinical Orthopaedics and Related Research, 1986(205): p. 299-308.

116. Takagi, K. and M.R. Urist, *The Reaction of the Dura to Bone Morphogenetic Protein (Bmp) in Repair of Skull Defects.* Annals of Surgery, 1982. **196**(1): p. 100-109.

117. Spicer, P.P., et al., *Evaluation of bone regeneration using the rat critical size calvarial defect.* Nature Protocols, 2012. **7**(10): p. 1918-1929.

118. Panyam, J. and V. Labhasetwar, *Biodegradable nanoparticles for drug and gene delivery to cells and tissue.* Advanced drug delivery reviews, 2003. **55**(3): p. 329-47.

119. Kataoka, K., A. Harada, and Y. Nagasaki, *Block copolymer micelles for drug delivery: design, characterization and biological significance.* Advanced drug delivery reviews, 2001. **47**(1): p. 113-31.

120. Shi, J., et al., *Nanotechnology in drug delivery and tissue engineering: from discovery to applications.* Nano letters, 2010. **10**(9): p. 3223-30.

121. Mironov, V., V. Kasyanov, and R.R. Markwald, *Nanotechnology in vascular tissue engineering: from nanoscaffolding towards rapid vessel biofabrication.* Trends in Biotechnology, 2008. **26**(6): p. 338-44.

122. Brechet, Y., et al., *Polymer based nanocomposites: Effect of filler-filler and filler-matrix interactions.* Advanced Engineering Materials, 2001. **3**(8): p. 571-577.

123. Henry, C.A., *The incorporation of nanomaterials into polymer media*. 2010. p. 35: In: Rakesh, K. Gupta, Elliot Kennel, Kwang-Jea Kim. Polymer Nanocomposites Handbook. CRC press.

124. Liu, H., E.B. Slamovich, and T.J. Webster, *Increased osteoblast functions among nanophase titania/poly(lactide-co-glycolide) composites of the highest nanometer surface roughness.* Journal of Biomedical Materials Research Part A, 2006. **78A**(4): p. 798-807.

125. Sultana, N., *In: Biodegradable polymer-based scaffolds for bone tissue engineering*. 2013: SpringerBriefs in Applied Sciences and Technology.

126. McMahon, R.E., et al., *Development of nanomaterials for bone repair and*

regeneration. Journal of biomedical materials research. Part B, Applied biomaterials, 2013. **101**(2): p. 387-97.

127. Webster, T.J., et al., *Enhanced functions of osteoblasts on nanophase ceramics.* Biomaterials, 2000. **21**(17): p. 1803-10.

128. Wei, G. and P.X. Ma, *Structure and properties of nano-hydroxyapatite/polymer composite scaffolds for bone tissue engineering.* Biomaterials, 2004. **25**(19): p. 4749-57.

129. Chen, L., et al., *Mechanical properties and in vitro evaluation of bioactivity and degradation of dexamethasone-releasing poly-d-l-lactide/nano-hydroxyapatite composite scaffolds.* Journal of the Mechanical Behavior of Biomedical Materials, 2013. **22**: p. 41-50.

130. Rodenas-Rochina, J., J.L. Ribelles, and M. Lebourg, *Comparative study of PCL-HAp and PCL-bioglass composite scaffolds for bone tissue engineering.* Journal of materials science. Materials in medicine, 2013. **24**(5): p. 1293-308.

131. Wutticharoenmongkol, P., et al., *Preparation and characterization of novel bone scaffolds based on electrospun polycaprolactone fibers filled with nanoparticles.* Macromolecular Bioscience, 2006. **6**(1): p. 70-7.

132. Cooke, F.W., *Ceramics in orthopedic surgery.* Clinical Orthopaedics and Related Research, 1992(276): p. 135-46.

133. Arts, J.J.C., et al., *The use of a bioresorbable nano-crystalline hydroxyapatite paste in acetabular bone impaction grafting.* Biomaterials, 2006. **27**(7): p. 1110-1118.

134. Venugopal, J.R., et al., *Nanobioengineered electrospun composite nanofibers and osteoblasts for bone regeneration.* Artificial Organs, 2008. **32**(5): p. 388-397.

135. Webster, T.J., et al., *Specific proteins mediate enhanced osteoblast adhesion on nanophase ceramics.* Journal of biomedical materials research, 2000. **51**(3): p. 475-483.

136. Shi, X.F., et al., *Rheological behaviour and mechanical characterization of injectable poly(propylene fumarate)/single-walled carbon nanotube composites for bone tissue engineering.* Nanotechnology, 2005. **16**(7): p. S531-S538.

137. Shi, X.F., et al., *Injectable nanocomposites of single-walled carbon nanotubes and biodegradable polymers for bone tissue engineering.* Biomacromolecules, 2006. **7**(7): p. 2237-2242.

138. Shi, X.F., et al., *Fabrication of porous ultra-short single-walled carbon nanotube nanocomposite scaffolds for bone tissue engineering.* Biomaterials, 2007. **28**(28): p. 4078-4090.

139. Pan, L.L., et al., *Multiwall carbon nanotubes/polycaprolactone composites for bone tissue engineering application.* Colloids and Surfaces B-Biointerfaces, 2012. **93**: p. 226-234.

140. Dufresne, A., *Polysaccharide nano crystal reinforced nanocomposites.* Canadian Journal of Chemistry, 2008. **86**(6): p. 484-494.

141. Habibi, Y. and A. Dufresne, *Highly filled bionanocomposites from functionalized polysaccharide nanocrystals.* Biomacromolecules, 2008. **9**(7): p. 1974-1980.

142. Chen, G.J., et al., *A Novel Thermoformable Bionanocomposite Based on Cellulose Nanocrystal-graft-Poly(epsilon-caprolactone).* Macromolecular Materials and Engineering, 2009. **294**(1): p. 59-67.

143. Habibi, Y., et al., *Bionanocomposites based on poly(epsilon-caprolactone)-grafted cellulose nanocrystals by ring-opening polymerization.* Journal of Materials Chemistry, 2008. **18**(41): p. 5002-5010.

144. Favier, V., et al., *Nanocomposite Materials from Latex and Cellulose Whiskers.* Polymers for Advanced Technologies, 1995. **6**(5): p. 351-355.

145. Favier, V., H. Chanzy, and J.Y. Cavaille, *Polymer Nanocomposites Reinforced by Cellulose Whiskers.* Macromolecules, 1995. **28**(18): p. 6365-6367.

146. Favier, V., et al., *Mechanical percolation in cellulose whisker nanocomposites.* Polymer Engineering and Science, 1997. **37**(10): p. 1732-1739.

147. Grunert, M. and W.T. Winter, *Nanocomposites of cellulose acetate butyrate reinforced with cellulose nanocrystals.* Journal of Polymers and the Environment, 2002. **10**(1-2): p. 27-30.

148. Eichhorn, S.J., et al., *Review: Current international research into cellulosic fibres and composites.* Journal of Materials Science, 2001. **36**(9): p. 2107-2131.

149. Kvien, I., B.S. Tanem, and K. Oksman, *Characterization of cellulose whiskers and their nanocomposites by atomic force and electron microscopy.* Biomacromolecules, 2005. **6**(6): p. 3160-3165.

150. Samir, M.A.S.A., et al., *Preparation of cellulose whiskers reinforced nanocomposites from an organic medium suspension.* Macromolecules, 2004. **37**(4): p. 1386-1393.

151. Marcovich, N.E., et al., *Cellulose micro/nanocrystals reinforced polyurethane.* Journal of Materials Research, 2006. **21**(4): p. 870-881.

152. van den Berg, O., J.R. Capadona, and C. Weder, *Preparation of homogeneous dispersions of tunicate cellulose whiskers in organic solvents.* Biomacromolecules, 2007. **8**(4): p. 1353-1357.

153. Gousse, C., et al., *Surface silylation of cellulose microfibrils: preparation and rheological properties.* Polymer, 2004. **45**(5): p. 1569-1575.

154. Araki, J., M. Wada, and S. Kuga, *Steric stabilization of a cellulose microcrystal suspension by poly(ethylene glycol) grafting.* Langmuir, 2001. **17**(1): p. 21-27.

155. Magalhães, M.C.F., P.A.A.P. Marques, and R.N. Correia, *Calcium and Magnesium Phosphates: Normal and Pathological Mineralization*, in *Biomineralization – Medical Aspects of Solubility*. 2007, John Wiley & Sons, Ltd. p. 71-123.

156. Tas, A.C., *Synthesis of biomimetic Ca-hydroxyapatite powders at 37 degrees C in synthetic body fluids.* Biomaterials, 2000. **21**(14): p. 1429-1438.

157. Wopenka, B. and J.D. Pasteris, *A mineralogical perspective on the apatite in bone.* Materials Science & Engineering C-Biomimetic and Supramolecular Systems, 2005. **25**(2): p. 131-143.

158. de Jong, W.F., *La Substance Minérale Dans les Os.* Recueil des Travaux Chimiques des Pays-Bas, 1926. **45**(6): p. 445-448.

159. Rey, C., et al., *Bone mineral: update on chemical composition and structure.* Osteoporosis International, 2009. **20**(6): p. 1013-1021.

160. Boskey, A., *Assessment of bone mineral and matrix using backscatter electron imaging and FTIR imaging.* Current Osteoporosis Reports, 2006. **4**(2): p. 71-75.

161. Posner, A.S. and F. Betts, *Synthetic Amorphous Calcium-Phosphate and Its Relation to Bone-Mineral Structure.* Accounts of Chemical Research, 1975. **8**(8): p. 273-281.

162. Onuma, K. and A. Ito, *Cluster growth model for hydroxyapatite.* Chemistry of Materials, 1998. **10**(11): p. 3346-3351.

163. Christoffersen, J., et al., *A Contribution to the Understanding of the Formation of Calcium Phosphates.* Journal of Crystal Growth, 1989. **94**(3): p. 767-777.

164. Brown, W.E. and L.C. Chow, *Chemical Properties of Bone Mineral.* Annual Review of Materials Science, 1976. **6**(1): p. 213-236.

165. Crane, N.J., et al., *Raman spectroscopic evidence for octacalcium phosphate and other transient mineral species deposited during intramembranous mineralization.* Bone, 2006. **39**(3): p. 434-42.

166. Pouget, E.M., et al., *The Initial Stages of Template-Controlled CaCO3 Formation Revealed by Cryo-TEM.* Science, 2009. **323**(5920): p. 1455-1458.

167. Mahamid, J., et al., *Mapping amorphous calcium phosphate transformation into*

crystalline mineral from the cell to the bone in zebrafish fin rays. Proceedings of the National Academy of Sciences of the United States of America, 2010. **107**(14): p. 6316-6321.

168. Gebauer, D., A. Volkel, and H. Colfen, *Stable Prenucleation Calcium Carbonate Clusters.* Science, 2008. **322**(5909): p. 1819-1822.

169. Beniash, E., et al., *Transient amorphous calcium phosphate in forming enamel.* Journal of Structural Biology, 2009. **166**(2): p. 133-143.

170. Dey, A., et al., *The role of prenucleation clusters in surface-induced calcium phosphate crystallization.* Nature Materials, 2010. **9**(12): p. 1010-1014.

171. Sato, K., et al., *Crystal Orientation of Hydroxyapatite Induced by Ordered Carboxyl Groups.* Journal of colloid and interface science, 2001. **240**(1): p. 133-138.

172. Colfen, H., *Biomineralization a Crystal-Clear View.* Nature Materials, 2010. **9**(12): p. 960-961.

173. Kokubo, T., *Bioactive glass ceramics: properties and applications.* Biomaterials, 1991. **12**(2): p. 155-63.

174. Kokubo, T. and H. Takadama, *How useful is SBF in predicting in vivo bone bioactivity?* Biomaterials, 2006. **27**(15): p. 2907-2915.

175. Ohtsuki, C., et al., *Apatite Formation on the Surface of Ceravital-Type Glass-Ceramic in the Body.* Journal of biomedical materials research, 1991. **25**(11): p. 1363-1370.

176. Ohtsuki, C., T. Kokubo, and T. Yamamuro, *Mechanism of Apatite Formation on Cao-Sio2-P2o5 Glasses in a Simulated Body-Fluid.* Journal of Non-Crystalline Solids, 1992. **143**(1): p. 84-92.

177. Gower, L.B., *Biomimetic model systems for investigating the amorphous precursor pathway and its role in biomineralization.* Chemical Reviews, 2008. **108**(11): p. 4551-627.

178. Thula, T.T., et al., *Mimicking the Nanostructure of Bone: Comparison of Polymeric Process-Directing Agents.* Polymers, 2011. **3**(1): p. 10-35.

179. Oldberg, A., A. Franzen, and D. Heinegard, *The primary structure of a cell-binding bone sialoprotein.* The Journal of biological chemistry, 1988. **263**(36): p. 19430-2.

180. Tanahashi, M. and T. Matsuda, *Surface functional group dependence on apatite formation on self-assembled monolayers in a simulated body fluid.* Journal of biomedical materials research, 1997. **34**(3): p. 305-315.

181. Granja, P.L., et al., *Cellulose phosphates as biomaterials. I. Synthesis and characterization of highly phosphorylated cellulose gels.* Journal of Applied Polymer Science, 2001. **82**(13): p. 3341-3353.

182. Granja, P.L., et al., *Cellulose phosphates as biomaterials. II. Surface chemical modification of regenerated cellulose hydrogels.* Journal of Applied Polymer Science, 2001. **82**(13): p. 3354-3365.

183. Lam, C.X.F., et al., *Scaffold development using 3D printing with a starch-based polymer.* Materials Science and Engineering: C, 2002. **20**(1–2): p. 49-56.

184. Brekke, J.H. and J.M. Toth, *Principles of tissue engineering applied to programmable osteogenesis.* Journal of biomedical materials research, 1998. **43**(4): p. 380-98.

185. Whang, K., et al., *Engineering bone regeneration with bioabsorbable scaffolds with novel microarchitecture.* Tissue Engineering, 1999. **5**(1): p. 35-51.

186. Green, D., et al., *The potential of biomimesis in bone tissue engineering: lessons from the design and synthesis of invertebrate skeletons.* Bone, 2002. **30**(6): p. 810-815.

187. Cima, L.G., et al., *Tissue Engineering by Cell Transplantation Using Degradable Polymer Substrates.* Journal of Biomechanical Engineering-Transactions of the Asme, 1991. **113**(2): p. 143-151.

188. Rezwan, K., et al., *Biodegradable and bioactive porous polymer/inorganic composite scaffolds for bone tissue engineering.* Biomaterials, 2006. **27**(18): p. 3413-3431.

189. Mikos, A.G., et al., *Preparation and Characterization of Poly(L-Lactic Acid) Foams.* Polymer, 1994. **35**(5): p. 1068-1077.

190. Park, T.G. and Y.S. Nam, *Porous biodegradable polymeric scaffolds prepared by thermally induced phase separation.* Journal of biomedical materials research, 1999. **47**(1): p. 8-17.

191. Schugens, C., et al., *Biodegradable and macroporous polylactide implants for cell transplantation .1. Preparation of macroporous polylactide supports by solid-liquid phase separation.* Polymer, 1996. **37**(6): p. 1027-1038.

192. Schugens, C., et al., *Polylactide macroporous biodegradable implants for cell transplantation .2. Preparation of polylactide foams by liquid-liquid phase separation.* Journal of biomedical materials research, 1996. **30**(4): p. 449-461.

193. Mooney, D.J., et al., *Novel approach to fabricate porous sponges of poly(D,L-lactic-co-glycolic acid) without the use of organic solvents.* Biomaterials, 1996. **17**(14): p. 1417-1422.

194. Annis, D., et al., *An elastomeric vascular prosthesis.* Transactions - American Society for Artificial Internal Organs, 1978. **24**: p. 209-14.

195. Sill, T.J. and H.A. von Recum, *Electrospinning: applications in drug delivery and tissue engineering.* Biomaterials, 2008. **29**(13): p. 1989-2006.

196. Thomas, V., et al., *Mechano-morphological studies of aligned nanofibrous scaffolds of polycaprolactone fabricated by electrospinning.* Journal of biomaterials science. Polymer edition, 2006. **17**(9): p. 969-84.

197. Sui, G., et al., *Poly-L-lactic acid/hydroxyapatite hybrid membrane for bone tissue regeneration.* Journal of biomedical materials research. Part A, 2007. **82**(2): p. 445-54.

198. Nie, H., et al., *Three-dimensional fibrous PLGA/HAp composite scaffold for BMP-2 delivery.* Biotechnology and Bioengineering, 2008. **99**(1): p. 223-34.

199. Burger, C. and B. Chu, *Functional nanofibrous scaffolds for bone reconstruction.* Colloids and surfaces. B, Biointerfaces, 2007. **56**(1-2): p. 134-41.

200. Zein, I., et al., *Fused deposition modeling of novel scaffold architectures for tissue engineering applications.* Biomaterials, 2002. **23**(4): p. 1169-1185.

201. Sachlos, E. and J.T. Czernuszka, *Making tissue engineering scaffolds work. Review: the application of solid freeform fabrication technology to the production of tissue engineering scaffolds.* European cells & materials, 2003. **5**: p. 29-39; discussion 39-40.

202. Emanuel, M.S., Somerville; John, S. Haggerty, Lincoln; Michael, J. Cima, Lexington; Paul, A. Williams, Concord, all of Mass., *Three-dimensional printing techniques*. 1993, Massachusetts Institute of Technology, Cambridge, Mass.

203. Charles, W.H., *Apparatus for production of three-dimensional objects by stereolithography*. 1986, UVP, Inc., San Gabriel, Calif: United States Patent.

204. Kim, S.S., et al., *Survival and function of hepatocytes on a novel three-dimensional synthetic biodegradable polymer scaffold with an intrinsic network of channels.* Annals of Surgery, 1998. **228**(1): p. 8-13.

Chapter 3. Bioactive cellulose nanocrystals-poly(ε-caprolactone) nanocomposites for bone tissue engineering applications

3.1. Abstract

We investigated the potential use of cellulose nanocrystals (CNCs) as multi-functional additives that can enhance the insufficient properties, such as poor mechanical properties and low biomineralization (bioactivity) of poly(ε-caprolactone) (PCL) for load-bearing bone tissue engineering applications. To this end, an *in vitro* biomineralization study on both sulfuric acid hydrolyzed-CNCs (SH-CNCs) and surface oxidized-CNCs (SO-CNCs) has been performed in order to evaluate the bioactivity of surface functional groups, sulfate and carboxyl groups, respectively. In addition, PCL composites containing different concentrations of the SO-CNCs were prepared using melt compounding extrusion and the physical/chemical properties of the nanocomposites were evaluated. From the biomineralization study, the carboxyl groups on the surface of CNCs (SO-CNCs) were more effective than the sulfate groups (SH-CNCs) in terms of calcium ion binding capacity, which could play an important role in the biomineralization process by the induction of mineral formation *in vivo*. The SO-CNCs exhibited a prominent effect on the mechanical reinforcement of PCL matrices. Therefore, the SO-CNCs are expected to play a critical role and are being considered as a potential candidate for reinforcing

nanofillers in the development of scaffold materials for bone tissue engineering applications.

3.2. Introduction

The use of nanomaterials as reinforcing additives has been attracting attention in many research areas for various applications over the last few decades because of the unique properties imparted to the material at the nanoscale. The biomedical engineering field, in particular, has emerged rapidly, and the potential effects of nanomaterials have been shown in drug/gene delivery and tissue engineering applications [1-4]. For example, bone scaffolds as temporary matrices for bone growth are a promising tissue engineering approach to replacing and mimicking the properties of natural bone tissue by providing a specific environment and architecture for native tissue regeneration [5]. Various of materials have been investigated to develop scaffolds. Relative to other materials, such as ceramics and metals, polymers have great inherent benefits of adjustable properties including biodegradation/bioresorption, versatility and processibility for tissue engineering applications. However, polymeric materials present critical challenges that need to be addressed, namely, inferior strength, stiffness, and bioactivity as bone scaffolds. Compared to traditional polymer composites with conventional filler materials, polymer nanocomposites can offer similar or improved properties at significantly lower filler loading levels. The enhanced mechanical properties of polymeric nanocomposites are mainly due to the high interfacial area (hundreds of m^2/g of materials) of stiffer nanoparticles, aspect ratio, and interparticle distance of the nanoparticles [6].

Therefore, one area of particular interest in this project is the development of bioresorbable polymer-based nanocomposite materials with naturally derived nanoparticles for bone scaffolds. The requirements for bone scaffolds are based on three distinct but closely related concepts associated with bone regeneration by tissue engineering: osteoinduction, osteoconduction, and osseointegration [7-9]. Thus, it is an important design criterion that the scaffolds possess adequate properties, similar to those of the natural bone tissue around the defect sites. For instance, a mechanical mismatch between the scaffold and surrounding bone tissue could induce bone resorption (e.g., a stress shielding effect) or failure of the scaffolds at the defect sites [10, 11]. Several studies have reported mechanical improvement of polymer-based nanocomposites by incorporating different types of nanoparticles, such as calcium phosphate mineral (also called hydroxyapatite (HA), $Ca_{10}(PO_4)_6(OH)_2$) [12-15] and carbon nanotubes [16-19]. Over the past few decades, cellulose nanocrystals (CNCs) have drawn significant interest as nano-fillers in polymer matrices [20-23]. CNCs are elongated rod-like nanoparticles derived from cellulose-containing natural resources (e.g., wood, plant, tunicate, algae, bacterial) [24] and have gained attention in various research fields because of their unique characteristics including superior mechanical properties, reactive surface properties, biodegradability, biocompatibility, low ecotoxicological risk and comparatively low cost [25-28].

In addition to the mechanical properties, the bioactivity in terms of bone formation (osteoconduction) ability of the scaffolds is also an important requisite for the development of scaffold materials in bone tissue engineering applications. Therefore, the

ability of a biomimetic bone scaffold to induce mineralization (i.e., HA formation *in vitro*) has been extensively investigated. In this sense, it is noteworthy that not only the solution chemistry in terms of ion activity but also the surface chemistry of the substrate may impact both the nucleation/growth of biominerals and the supersaturation of the growth environments during the mineralization process [29-32]. Tadashi Kobubo *et al.* reviewed correlations between apatite formation on the surface of various materials in SBF *in vitro* and their *in vivo* bioactivity [33]. They concluded that there is no correlation between apatite formation in SBF at several concentration levels (e.g., 1.5x SBF) and its *in vivo* mineralization on a material, whereas the results obtained using 1x SBF correlated well with *in vivo* bioactivity [33]. This last point is crucial for the successful development of new bioactive bone scaffold materials on the basis of predictions from apatite formation on their surfaces in SBF. Although numerous studies using SBF with several-fold differences in concentration have reported that HA formation with a Ca/P ratio of ~1.67 on the proposed bone scaffold materials occurs during *in vitro* biomimetic mineralization, it must be pointed out that the use of such fluids does not allow conclusions with regard to the ability to promote biomineralization, or the bioactivity of the bone scaffold materials *in vivo*.

Tanahashi *et al.* examined the rate of apatite formation on self-assembled monolayers (SAMs) with different terminal functional groups in SBF [34]. The most potent functional group for apatite formation was the negatively charged -PO_4H_2 followed by the -COOH group. However, nonionic groups ($CONH_2$ and OH) and a positively charged group (NH_2) showed weaker nucleating ability, and it was found that apatite formation

was inhibited on CH_3-terminated SAMs [34]. These findings indicate that, surface modification is a good strategy for enhancing the bioactivity in terms of mineralization of polymer-based bone scaffold materials.

Nevertheless, there have been no reports of the bioactivity of CNCs in SBF *in vitro*. Therefore, the overall goal of this research is to investigate the potential use of surface modified CNCs as multi-functional additives and their ability to enhance the mechanical properties and increase the biomineralization rate of poly(ε-caprolactone) PCL for bone tissue engineering applications. The role of the surface functional groups on the biomineralization rate was evaluated by comparison of sulfuric acid hydrolyzed CNCs (SH-CNCs) containing sulfate groups and surface-oxidized SH-CNCs (SO-CNCs) containing both sulfate groups and carboxyl groups. During the mineralization in SBF, it is expected that calcium ions tend to bind to the carboxylate moieties on the surface of SO-CNCs more effectively than those of the SH-CNCs. In addition, physical properties of SO-CNCs/PCL nanocomposites were assessed as a potential candidate for the bone scaffold material.

3.3. Experimental

3.3.1. Materials

Bleached softwood sulfite dissolving-grade pulp (Temalfa 93A) was kindly provided by Tembec Inc. Sulfuric acid (H_2SO_4, 96.2 wt %), acetonitrile (CH_3CN, HPLC Grade), dichloromethane (CH_2Cl_2), and sodium hydroxide (NaOH, 0.5M) were purchased from

Fisher Scientific. 2,2,6,6,-Tetramethyl-1-piperidinyloxy (TEMPO, $C_9H_{18}NO$, free radical, 98%), sodium hypochlorite solution (NaClO, reagent grade, available chlorine 10-15%), methanol (CH_3OH, anhydrous, 99.8%) polycaprolactone (PCL, $(C_6H_{10}O_2)_n$, M_n: 70,000-90,000) were purchased from Sigma-Aldrich. Sodium bromide (NaBr, 99+%, extra pure, anhydrous) was purchased from Acros organics.

3.3.2. Methods

3.3.2.1. CNCs preparation

CNCs were prepared from bleached, dissolving-grade softwood sulfite pulp (Temalfa 93A), kindly provided by Tembec Inc. (Témiscaming, QC, CA). Milled (60-mesh, Thomas Wiley® Mini-Mill, Thomas Scientific) pulp was hydrolyzed for 60 min with 64 wt % sulfuric acid (96.2 wt %, Fischer Scientific) at 45.5 ºC and an acid-to-pulp ratio of 10 mL/g. After 60 min, the reaction mixture was diluted by addition of cold (~4 ºC) deionized (DI) water (2500 mL, 18.2 MΩ·cm, Millipore Direct-Q5 Ultrapure Water System) and the acid was removed by centrifugation (4500 rpm for 20 min at 4 ºC, IEC CENTRA GP8R Refrigerated Centrifuge, Thermo Electron Corporation) followed by discarding of the supernatant. The sediment was redispersed in DI water and centrifuged. This step was repeated three times. Then, the collected sediment was transferred to dialysis tubing (Spectra/Por 4, molecular weight cut off of 12-14 kDa) and dialyzed against DI water (refreshed daily) for one week to remove the residual acid. After the dialysis, the CNC suspension was sonicated (BRANSONIC® 3510) for 30 min and filtered through a poly(vinylidene fluoride) (PVDF) syringe filter (0.45µm, Watman,

Ltd.). The final concentration of the obtained aqueous CNC suspension was obtained ~1 wt %.

Surface modification of the sulfuric-acid hydrolyzed CNCs, henceforth denoted SH-CNCs, was performed by (2,2,6,6-tetramethylpiperidin-1-yl)oxyl (TEMPO)-mediated oxidation according to the method of Araki *et al.* [35] with minor modifications based on the method of Habibi *et al.* [36]. Briefly, 500 g of 1 wt % aqueous SH-CNC suspension, 0.5 g of TEMPO (free radical, 98 %, Sigma-Aldrich), and 5 g of sodium bromide (NaBr, 99+ %, extra pure, anhydrous, Acros organics) were thoroughly mixed in a 1,000 mL flask with a magnetic stir bar at room temperature. The reaction was started by gradual addition of 50 mL sodium hypochlorite solution (reagent grade, available chlorine 10-15 %, Sigma-Aldrich) so that the pH of the reaction mixture remained in the range 10.2-10.5. The reaction was continued for three hours under addition of sodium hydroxide (0.5 M) to maintain the pH. The reaction was quenched by addition of 5 mL of methanol and the mixture was transferred to dialysis tubing and dialyzed against DI water (refreshed daily) for two weeks. Finally, the obtained aqueous suspension of surface-oxidized CNCs (SO-CNCs) was sonicated for 30 min and filtered through a 0.45 µm syringe filter. The concentration of both suspensions (SH-CNC and SO-CNC) was adjusted to 3 wt % with a rotary evaporator (Büchi Rotavapor R-200) using a water bath temperature of 40 ^{o}C.The stock suspensions were stored in a refrigerator until used.

3.3.2.2. Conductometric titration

The surface charge densities of SH-CNCs and SO-CNCs were determined by conductometric titration. The aqueous suspensions were placed over a small amount of ion-exchange resin (Rexyn®I-300 (H-OH), certified, research grade, Fisher Scientific) for 12 h and filtered through 1.0 µm syringe filters before the titration. The ion exchange resin treated SH-CNCs and SO-CNCs are denoted SH-CNC-I and SO-CNC-I, respectively. The titration of 45 mL of 0.20 wt % SH-CNC suspension was carried out after the addition of 5 mL of 0.01 M potassium chloride (KCl) to increase the ionic strength. Also, the titration of 40 mL of 0.20 wt % SO-CNC suspension was conducted after the addition of 20 mL of 0.01 M hydrochloric acid (HCl). The electrical conductivity was recorded with a pH/conductivity meter (Mettler Toledo SevenMulti S47 pH/conductivity meter with an InLab 730 conductivity probe) every 30 s after addition of 100 µL aliquots of 0.01 M sodium hydroxide (NaOH) by micropipette. The titrations were repeated once and the results were averaged. The surface charge density (σ) was calculated with the following equation [37]:

$$\sigma = \frac{C_{NaOH} \times V_{NaOH}}{C_{CNC} \times \alpha_{CNC}}$$

where C_{NaOH} is the concentration of NaOH, V_{NaOH} is the volume of NaOH at the equivalence point, C_{CNC} is the concentration of the CNC suspension, α_{CNC} is the amount of CNC suspension titrated. However, V_{NaOH} was defined as V_2-V_1 for the SO-CNCs since the initial decrease of conductivity is due to the neutralization of the excess protons of HCl and sulfate group. V_1 (1st equivalence point) is the volume of NaOH (L) consumed to

neutralize the excess protons of HCl as well as sulfate group. V_2 (2^{nd} equivalence point) is the volume of NaOH (L) consumed for those attached to the carboxyl groups, respectively.

3.3.2.3. Biomineralization of SH-CNCs and SO-CNCs *in vitro*

An in vitro biomineralization study was performed in simulated body fluid (SBF) at 37 ºC. SBF with nearly identical ion concentrations to those of human blood plasma was carefully prepared as described in Tadashi Kobubo *et al.* [33], denoted corrected SBF (c-SBF) in the article. For CNC mineralization, 100 mL portions of 1 wt % aqueous suspensions of either SH-CNCs or SO-CNCs were placed in dialysis tubing and suspended in 3,000 mL of SBF at 37 ºC for up to 800 h under stirring. The SBF was refreshed every 24 h. The mineralized CNCs were collected (10 mL) at different incubation time points and dialyzed against DI water for 48 h in order to remove the free ions from the SBF. The aqueous suspensions of both mineralized CNCs were stored at 4 °C prior to analysis.

3.3.2.4. Atomic force microscopy (AFM)

AFM samples of SH-CNCs and SO-CNCs were prepared from 0.002 wt % aqueous suspensions. After 10 min sonication, 15 µL of each CNC suspension was spin coated at 4,000 rpm for 1 min with a spin coater (Laurell model WS-400B-6NPP/LITE) onto a freshly cleaved mica disc (diameter: 0.5 in., Ted Pella) mounted with epoxy adhesive resin onto a standard microscope slide. The spin coated CNC samples were dried

overnight at 60 °C under vacuum. AFM samples of the PCL nanocomposites were prepared by immersion of nanocomposite filaments in liquid N_2 followed by fracture of the filament in flow direction of the melt compounding extrusion process. Fresh fracture surfaces were imaged under ambient conditions in tapping (AC) mode with an Asylum Research MFP3D-Bio atomic force microscope using standard silicon probes (Olympus OMCL-AC160TS, resonant frequency: ~300 kHz, spring constant: ~42 N/m, nominal tip radius: <10 nm). Images were recorded with a resolution of 512 points/scan and analyzed using IGOR pro software using identical parameters for the mask tool, flattening tool, z-scale, and phase range.

3.3.2.5. Inductively coupled plasma atomic emission spectroscopy (ICP-AES)

ICP-AES (Spectro ARCOS, Spectro Analytical Instruments, Inc.) was used for analyzing the concentrations of elements, such as sulfur (S), phosphorus (P), and calcium (Ca), before and after mineralization of the CNCs. Five milliliter of CNC suspensions (5 mg/mL) were treated with 25 mL of nitric acid (70%, TraceMetal Grade, Fisher Scientific) for two hours at 60 °C in an ultrasonic bath (40 kHz, 130 Watts). One milliliter of the thus digested suspension was added to 39 mL of DI water resulting in a final CNC concentration of 0.02 mg/mL in HNO_3 (2%). Measurements were carried out in triplicate and the results were averaged.

3.3.2.6. SO-CNC/PCL nanocomposite fabrication

The SO-CNCs were suspended in acetonitrile (CH_3CN, HPLC Grade, Fisher Scientific) by solvent exchange. The solvent exchange process was performed by addition of acetonitrile to the aqueous SO-CNC suspension. The mixture was centrifuged at 5,000 rpm in a centrifuge (SORVALL LEGEND X1R Centrifuge, Thermo Scientific) for 20 min and fresh acetonitrile was added to the collected sediment. This step was followed by homogenization (Power Gen 500, Sawtooth 10 x 95 mm, Fisher Scientific) for 5 min and sonication for 30 min. This process was repeated three times. PCL (Mw = 70,000-90,000, Sigma Aldrich) was dissolved in dichloromethane (Fisher Scientific). The ratio of PCL to dichloromethane was 1:10 (w/v). The solvent-exchanged SO-CNC suspension was sonicated at 40 °C for 30 min under stirring (300 rpm) and the PCL solution was slowly added before solvent casting into a glass petri dish. The cast film was allowed to dry at room temperature for 48 h, then placed in a vacuum oven at 40 °C for 24 h. The solvent cast films were cut into small pellets, then thoroughly rinsed with DI water and dried in a vacuum oven at 40 °C for 24 h. Finally, the pellets were extruded into a 3 mm (diameter) filament with a twin screw extruder (HAAKE MiniLab II, ThermoFisher Scientific) at 80 °C. The SO-CNCs/PCL nanocomposites were prepared with different SO-CNC contents ranging from 0 wt % (PCL0) to 10 wt % (PCL10).

3.3.2.7. Tensile test

Tensile tests of SO-CNCs/PCL nanocomposite filaments were performed with an MTS Sintech 10/GL Material Testing Workstation equipped with a 100 N load cell. A cross

head speed of 10 mm/min was used at ambient conditions (in air at room temperature) was used. Measurements were performed in quintuplicate and results were averaged. Measurements with yield near the grips were excluded.

3.3.2.8. Thermal analysis

DSC measurements were performed with a TA Instruments Q2000 differential scanning calorimeter that had been calibrated with indium and sapphire standards. Nitrogen, at a flow rate of 50 mL/min, was used as the purge gas. Approximately 5 mg of sample was placed in a standard aluminum DSC pan (TA Instrument). The DSC scans were done using heating/cooling/heating/cooling process with a heating rate of 10 °C/min and a temperature range of -75 to 100 °C. Experiments were done in triplicate. The glass transition temperature (T_g), melting temperature (T_m), crystallization temperature (T_c), and enthalpy of fusion, ΔH_f, were measured with the TA Instruments' Universal Analysis 2000 software. The degree of matrix crystallinity, X_c, was calculated from ΔH_f with the following equation [38]:

$$X_c = \frac{1}{(1-\omega_f)} \times \frac{\Delta H_{f_{sample}}}{\Delta H_{f_{PCL}}} \times 100\ \%$$

where ω_f is the weight fraction of the filler in the composite and $\Delta H_{f_{PCL}}$ is the heat of fusion of the matrix polymer at 100 % crystallinity. The percentage of crystallinity was estimated using a value of 139.5 J/g for the heat of fusion of 100 % crystalline PCL [39].

In addition, the thermal degradation temperatures of SO-CNC (film form) and PCL nanocomposites (PCL 0 and PCL 10) were determined by thermogravimetric analysis (TGA, TA Instruments TGA Q500) (see Appendix C). Approximately 10-15 mg of sample was placed into a platinum TGA sample pan. Thermogravimetric (TG) and derivative TG (DTG) curves between ~ 30°C and 500 °C were recorded with a heating rate of 10 °C/min using air as sample purge gas.

3.3.2.9. Contact angle measurements

For contact angle measurements, SO-CNCs/PCL nanocomposite films (~5 mm in width, ~2 mm in thickness) were prepared using a twin-screw extruder. Measurements were performed with a FTA 200 Dynamic Contact Angle Analyzer equipped with a motor-driven syringe. Approximately 1 µl droplets of each DI water and SBF were carefully deposited onto the sample surface using a syringe 250 µl syringe (Hamilton gastight®) with a stainless steel needle. Images were recorded within 2 s and the contact angle was analyzed with Drop Shape Analysis software (FTA32 Video 2.1). Measurements were carried out in triplicate and the results were averaged.

3.3.2.10. Optical light microscopy

Thin slices of approximately 50 µm thickness were microtomed off of the transverse surface (perpendicular to the flow direction) of the PCL nanocomposites using a sliding microtome (Model 860, American Optical Company). The microtomed slices were placed on regular microscopy cover glasses and heated to 300 °C for 10 min using the

TGA. After that, optical microscopy images were recorded with a Canon EOS 20D digital single-lens reflex camera (8.2. megapixels) mounted onto a Zeiss Axioskop 40 A POL microscope.

3.4. Results and discussion

CNCs were prepared from milled wood pulp by sulfuric acid hydrolysis. For an analysis of the effect of surface functional group on mineralization, sulfuric acid-hydrolyzed CNCs (SH-CNCs), carrying sulfate groups, were modified by TEMPO-mediated oxidation to give surface-oxidized CNCs (SO-CNCs), carrying primarily carboxyl groups. The surface charge density of SH-CNCs and SO-CNCs after treatment with ion exchange resin, denoted SH-CNC-I and SO-CNC-I, respectively, was determined by conductometric titration as shown in Figure 3.1. The initial decrease of conductivity in the titration curve of SH-CNC-I corresponds to the neutralization of partially dissociated sulfate groups. After the equivalence point, the conductivity increases due to the addition of excess NaOH (titrant). The amount of sulfate groups per mass of SH-CNC-I is calculated from the volume of NaOH at the equivalence point (V). The sulfate group density of SH-CNC-I was calculated to be 0.271 ± 0.002 mmol/g (compared to 0.316 ± 0.007 mmol/g for SH-CNC, see Appendix A). Titration curves of SO-CNC-I, on the other hand, exhibited two equivalence points. The first equivalence point (V_1) corresponds to the neutralization of added HCl and any remaining sulfate groups. The second equivalence point (V_2) corresponds to the neutralization of the carboxyl groups. Since TEMPO-mediated oxidation selectively oxidizes the primary hydroxyl groups of cellulose, the reaction results in the conversion of approximately one third of the

available surface hydroxyl groups not occupied by sulfate groups to carboxyl groups. The number of carboxyl groups per mass of SO-CNC-I was estimated from the volume of the titrant between the two equivalence points. The obtained surface charge density of SO-CNC-I was 1.997 ± 0.142 mmol/g (compared to 1.840 ± 0.004 mmol/g for SO-CNC, see Appendix A). Thus, the surface charge density of SO-CNC-I was about 7 times (6 times before ion exchange treatment) higher than that of SH-CNC-I. Additionally, ICP analysis was performed to measure the sulfur content of the CNCs before and after ion exchange treatment. Table 3.1 compares the sulfur contents (mg/g) of the CNC samples obtained by conductometric titration and ICP analysis (also see Appendix A). As seen in the table, the values obtained by conductometric titration and ICP analysis were in good agreement. Both the surface oxidation and treatment with ion exchange resin resulted in a decrease in the sulfur content of CNCs. According to the ICP data, surface oxidation caused a 21% reduction in the sulfur content (16% reduction after ion exchange resin treatment). These data demonstrate that SO-CNCs still contain about 80% of the initial sulfate groups but that carboxyl groups are the primary functional group on SO-CNCs, accounting for 86-89% of the anionic surface groups.

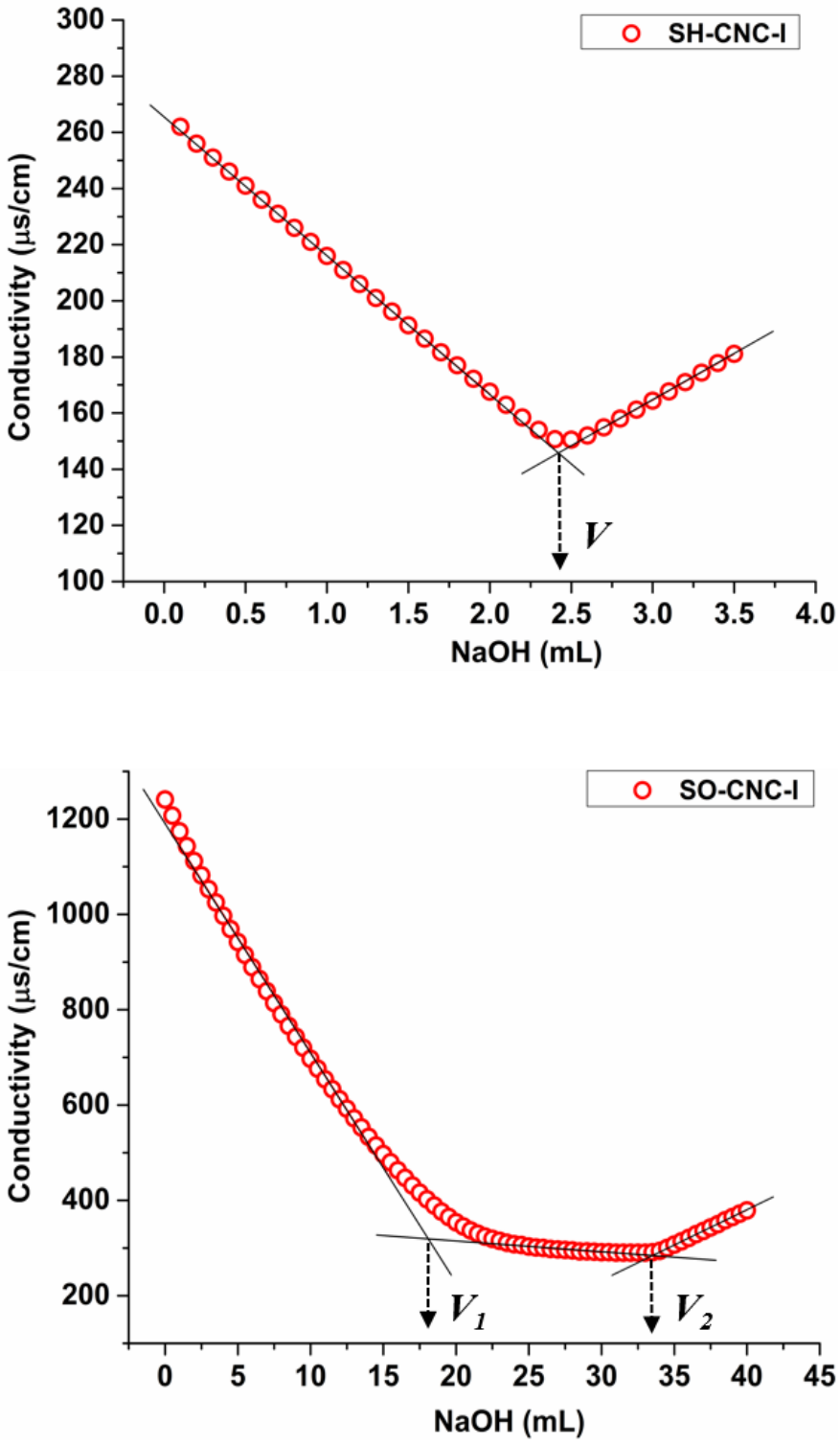

Figure 3.1. Conductometric titration curves for SH-CNC-I (top) and SO-CNC-I (bottom).

Table 3.1. Sulfur content of CNCs before and after treatment with ion exchange resin measured by conductometric titration and ICP analysis.

Sample	Sulfur content (mg/g)	
	Conductometric titration	ICP analysis
SH-CNC	10.11 ± 0.22	10.83 ± 0.20
SH-CNC-I	8.67 ± 0.05	9.00 ± 0.21
SO-CNC	-	8.56 ± 0.21
SO-CNC-I	-	7.59 ± 0.08

**** SH-CNC-I and SO-CNC-I indicate the ion exchange resin treatment.***

The effect of the type of surface group, sulfate *versus* carboxyl, on the *in vitro* mineralization of CNCs was evaluated by incubation of the CNCs in SBF. Figure 3.2 shows 3D AFM height images of CNCs before (0 h) and after incubation at 37 °C for 400 h. Both CNCs appeared significantly larger after mineralization. The mean particle dimensions were determined from AFM height images. Before mineralization, SH-CNCs and SO-CNCs had a mean length of 121.5 ± 23.8 nm and a mean height of 3.86 ± 1.1 nm in accordance with the literature [24]. The initial dimensions of SO-CNCs (mean length of 89.3 ± 22.7 nm and mean height of 2.23 ± 0.6 nm) were smaller, indicating an effect of the oxidation procedure on particle size. After 400 h of incubation in SBF, the size of CNCs was noticeably larger (Figure 3.2 b and d) than before (Figure 3.2 a and c). While the CNCs did not aggregate before incubation because of their negative surface charge (Figure 3.2 a and c), mineralized CNCs exhibited some degree of aggregation (Figures

3.2 b and d), possibly indicating a screening of their surface charge. Sonication was not performed during sample preparation for AFM analysis because it could affect the thickness of the mineral layer on the mineralized CNCs. For error minimization, only individual nanoparticles were used for height determination.

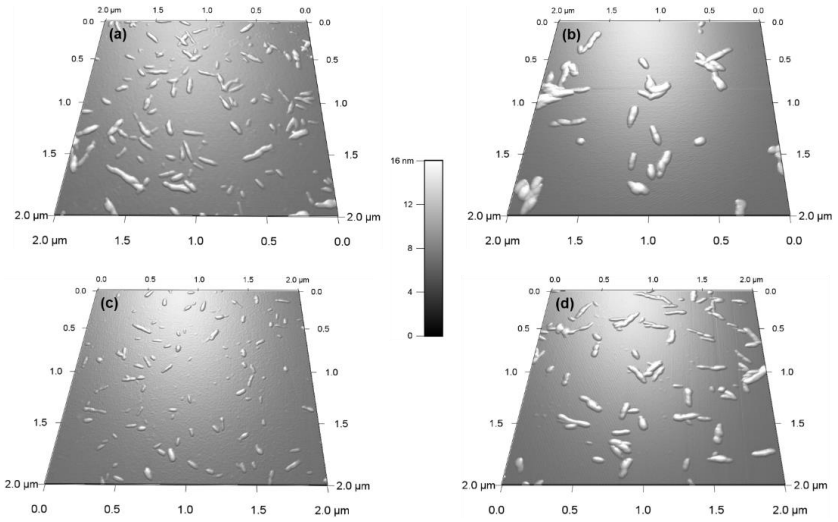

Figure 3.2. 3D AFM height images of SH-CNCs (a and b) and SO-CNCs (c and d) before (a and c)/after (b and d) 400 h incubation in SBF at 37 °C.

The extent of mineralization was quantified using height data because width and length data of CNCs have greater natural fluctuations. Moreover, as opposed to length and width measurements, AFM height measurements are not affected by tip broadening and therefore generally considered more accurate. The average height of the CNCs as a function of incubation time is shown in Figure 3.3. The initial mean height of SO-CNCs was smaller than that of SH-CNCs because of the effect of the oxidation process on particle size.

For the SH-CNCs, the height was significantly increased from 0 h (3.9 ± 1.1 nm) to 10 h (4.5 ± 1.0 nm) and from 10 h to 40 h (5.1 ± 0.7 nm), but no statistical difference (Least Significant Difference (LSD) test at the 0.05 level) was observed from 20 h (5.1 ± 0.7 nm) to 800 h (5.4 ± 1.1 nm). For the SO-CNCs, the height was increased from 0 h (2.2 ± 0.6 nm) to 10 h (3.4 ± 0.7 nm) and from 20 h (3.6 ± 0.8 nm) to 30 h (4.8 ± 0.6 nm), but there was no statistically significant difference between 30 h and 800 h (5.1 ± 1.4 nm). Although a similar trend for the height change was observed for both CNCs, the total increase in height was greater for the SO-CNCs (2.3 times) than for the SH-CNCs (1.4 times). Considering the rod-like shape of CNCs, the height increase indicates that the SO-CNCs exhibited a thicker coating (~1.45 nm thickness) with certain minerals than the SH-CNCs (~0.75 nm thickness). The thicker coating of the SO-CNCs could be due to their higher surface charge density or to the higher calcium affinity of the carboxyl group, compared to the sulfate group.

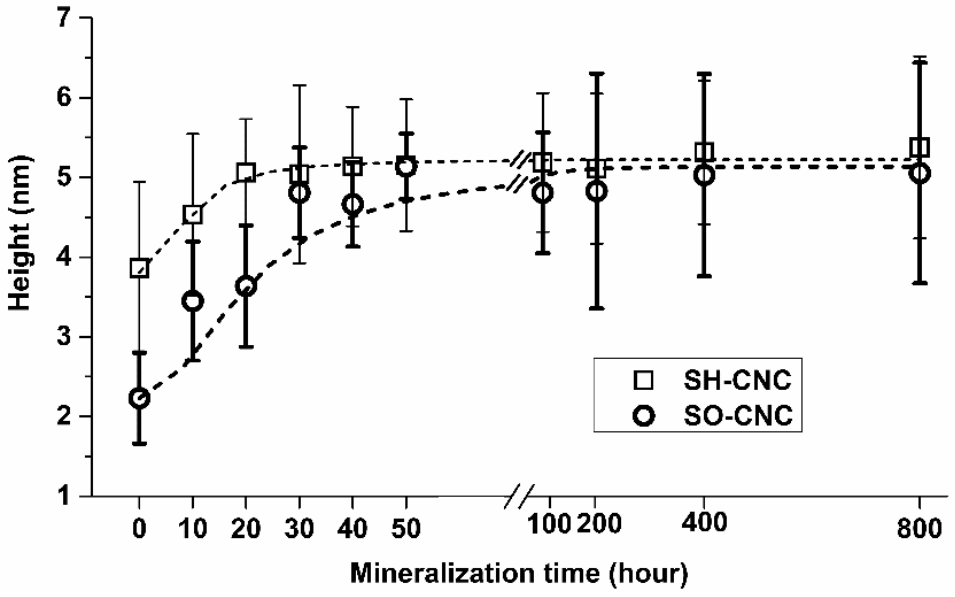

Figure 3.3. Height changes of CNCs during the incubation in SBF at 37 °C.

However, it is possible that the height increase could be due to the aggregation of CNCs in SBF. In order to illuminate this issue, the AFM phase images were analyzed to determine whether there were any differences on the surface properties of CNCs before and after the mineralization. The phase images were obtained simultaneously with the height images using tapping-mode of AFM under identical imaging conditions as described previously. Fig. 3 shows the phase images of CNCs. The AFM tapping-mode provides information about topography and properties of the specimen's surface, such as stiffness, viscoelasticity, or surface-adhesion energy measured by the phase shift (also known as phase lag) of the cantilever oscillation relative to the driving signal as reference [40-42]. In addition, the phase shift allows us to identify regions of different interactions by the amount of energy dissipated in the tip-sample interaction, and thus it was used to directly visualize the different surface charge characteristics [43-45]. Therefore, it should be possible to detect whether any changes to the surface of CNCs occurred during mineralization using the AFM phase image. In the present study, we assume that the size (thickness) increase results from a certain amount of mineral formation due to the deposition of ions on the surface of CNCs in SBF. Figure 3.4 shows the phase images of CNCs (shown in Figure 3.2) before (a and c) and after 400 h incubation (b and d) in SBF. The phase shift was clearly observed and the differences of SH-CNCs and SO-CNCs after the mineralization were 2.91 ± 1.37º and 5.10 ± 1.22º, respectively. Before the mineralization, the phase shift caused by the interactions between the CNCs and tip was 8.17º ± 1.11 (SH-CNCs, Figure 3.4 a) and 7.88º ± 0.98 (SO-CNCs, Figure 3.4 c) and there was no statistical difference (LSD test at the 0.05 level) between them. However, it was significantly decreased to 5.26º ± 0.81 (SH-CNCs, Fig. 3 b) and 2.78º ± 0.73 (SO-

CNCs, Figure 3.4 d), and also the decreased phase shifts observed with SH-CNCs and SO-CNCs were statistically different from one another. As described previously, the CNCs were prepared on a freshly cleaved mica disc. Mica is a silicate mineral (mainly composed of SiO_2: 45.57 % and Al_2O_3: 33.10 %) and the phase shift of the substrate was about ± 0.6º. The reason is that the hydrophobic substrate does not interact strongly with the AFM tip (hydrophilic silicon tip) resulting in a small phase shift [46] shown in reddish color (Figure 3.4). On the other hand, the hydrophilic CNCs were shown in bluish color caused by the phase shift. Interestingly, the phase lag of SO-CNCs was similar to that of the mica (mineral) substrate. However, the effect of sulfate group (SH-CNCs) was less pronounced. Therefore, the results from the phase image analysis indicated that the size (thickness) increase measured by the height images is not caused by the aggregation of CNCs but caused by certain mineral coating on the surface of CNCs during the mineralization. Even though the shift in phase difference was greater with the SO-CNCs than those of the SH-CNCs, a precise determination of components that altered the surface charge of CNCs could be challenging. However, there is high probability of such cationic depositions in SBF, possibly the calcium ion, on the negatively charged surface of CNCs by the sulfate groups (SH-CNCs) and the carboxyl groups (SO-CNCs), and thus the SO-CNCs showed more impact on the mineralization in terms of overall size increase resulting from ion depositions than the SH-CNCs.

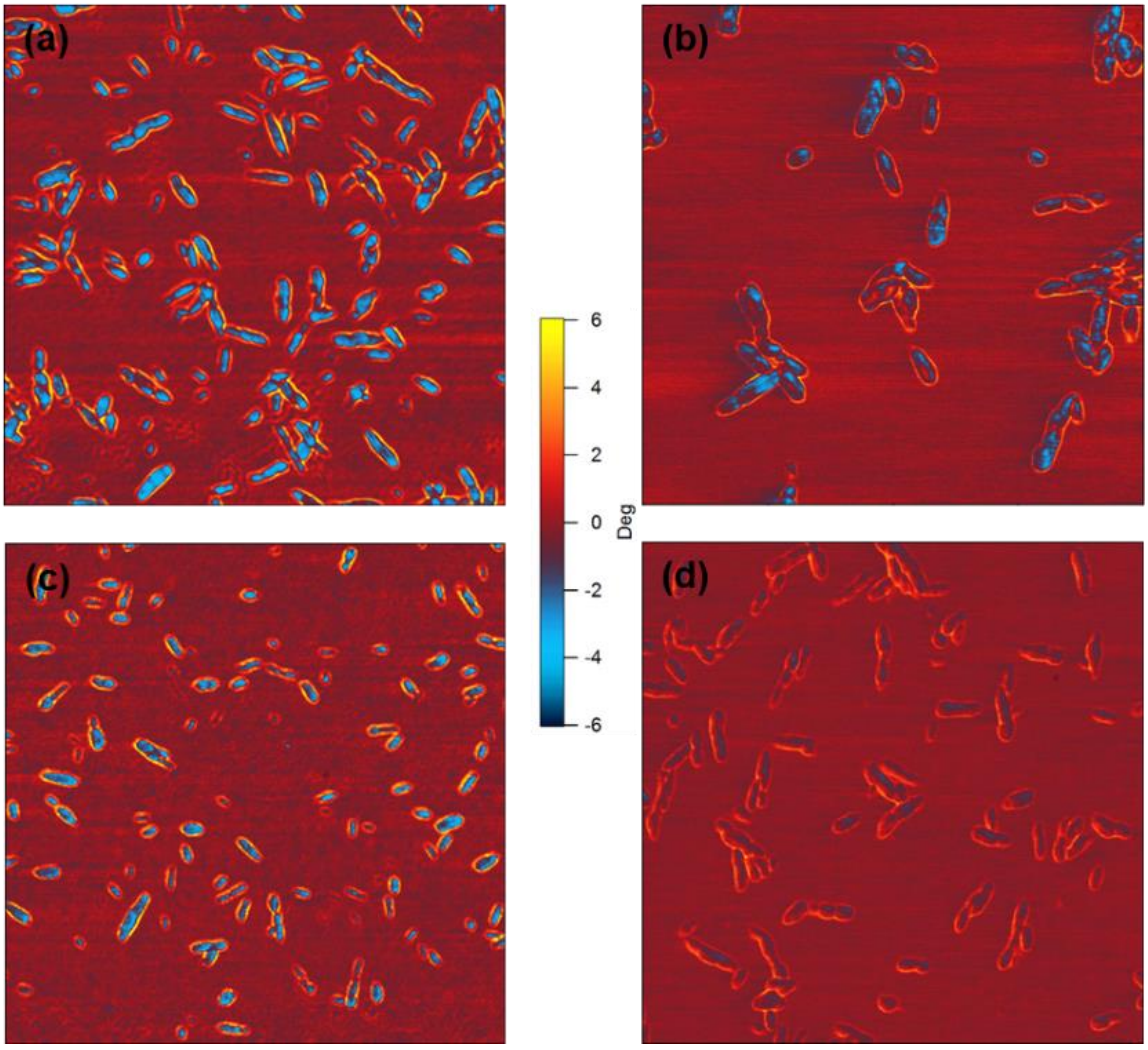

Figure 3.4. AFM phase images of SH-CNCs (a and b) and SO-CNCs (c and d) before (left)/after (right) 400 h incubation in SBF at 37 °C. Scan size: 2 µm x 2µm.

In addition, the elements deposited on the surface of the CNCs were analyzed using ICP. Considering the purpose of this study for bone tissue engineering applications, the most interesting elements are calcium and phosphorus ions in terms of a calcium phosphate mineral formation during the mineralization in SBF. A synthetic HA (≥ 97%, Sigma-Aldrich) was used as a control and stoichiometric HA ($Ca_{10}(PO_4)_6(OH)_2$) has the

composition with a Ca/P ratio of 2.15 by atomic weight (shown in table 1) and 1.67 by atomic ratio. Obviously, formation of HA was not observed based on the Ca/P ratios from this study. Moreover, significantly higher Ca/P ratios were obtained for both CNCs than are present in bone-like apatite.

We have attempted to identify the deposited layer on the CNCs with different techniques, such as X-ray diffraction (see Appendix B). However, no peak was observed that was comparable to those of HA. The mechanism of HA formation is very complicated and still under investigation. Dey *et al.* demonstrated that the development of oriented apatite crystals is induced by the densification of amorphous calcium phosphate (ACP) at a templating surface and before that calcium phosphate prenucleation clusters (0.87 ± 0.2 nm in diameter) aggregate in equilibrium with ions in solution (SBF) as an early stage [30]. In comparison with our studies, it could be possible that the negatively charged CNCs have strong affinity to bind some ions before the formation of pernucleation clusters since the CNCs were suspended in SBF. This experimental setup differs from others where the samples were secured (commonly at the bottom) during the experiment. Therefore, the significantly higher Ca/P ratios in this study are possibly due to the fact that negatively charged (e.g., sulfate and carboxyl groups) CNCs with free mobility have more chance to selectively bind calcium ions in SBF.

Table 3.2. ICP analysis of CNCs before and after mineralization.

	Analyte	Ca (mg/L)		P (mg/L)		Ca/P	
	Time (hour)	Average	STDEV	Average	STDEV	Average	STDEV
SH-CNC	0	< 0.021	-	< 0.015	0.001	-	-
	50	0.387	0.002	0.147	0.002	2.64	0.029
	800	0.292	0.001	0.035	0.001	8.25	0.327
SO-CNC	0	0.101	0.001	< 0.015	-	-	-
	50	4.61	0.025	0.118	0.004	39.0	1.40
	800	1.99	0.017	0.060	0.005	33.4	2.82
HA	-	147.0	1.93	68.5	0.132	2.15	0.028
2% HNO_3	-	< 0.021	-	< 0.015	-	-	-

**** Samples were prepared in aqueous 2% HNO_3, Data reported as mg/L, The "<" indicates concentrations less than the instrument detection limit. Time (h) indicates the incubation period at 37 ºC for the mineralization.***

Recently, similar results have been reported by Zurick *et al.* [47]. They reported that the primary noncollagenous proteins (e.g., bone sialoprotein, osteopontin, and dentin sialophosphoprotein) found in mineralized tissues play significant roles in the biomineralization process by the induction of biomimetic mineral formation [47]. Importantly, those proteins containing carboxy-terminal fragments are highly negatively charged molecules that have the capacity to bind calcium ions (i.e., calcium chelating properties). The results showed that the significantly larger Ca/P ratios (approximately 4~20) were obtained in the presence of these proteins thereby indicating a potential role in biomineralization [47, 48]. One should, however, keep in mind that mineralization of bone (or bone formation) only occurs if bone-forming cells (osteoblasts) and other biological factors are intimately involved and regulated properly in the body, which is a very complex process to mimic. Considering the AFM and ICP data analysis, the carboxyl groups more effectively bound calcium ions than did the sulfate groups, and

thus the SO-CNCs could be a better candidates for bone tissue engineering applications in terms of the mineralization (or bioactivity). Therefore, SO-CNCs as multi-functional additives were applied for fabrication of PCL-based nanocomposites.

It is a critical factor that the materials provide adequate mechanical properties as bone scaffolds for critical sized defects. Thus, mechanical properties of SO-CNCs/PCL nanocomposites were evaluated vs. SO-CNC content. As mentioned earlier, one area of particular interest in this study is the development of bioresorbable polymer-based nanocomposites with naturally derived nanoparticles for bone scaffold materials. However, many of the naturally derived nanoparticles (e.g., polysaccharide-based nanoparticles) have hydrophilic groups (e.g., hydroxyl, carboxyl, and amino groups) while bioresorbable polymers (e.g., aliphatic polyesters) exhibit a relatively hydrophobic nature. Thus, it is difficult and challenging to achieve a homogeneous dispersion of the hydrophilic nanoparticles in the hydrophobic polymer matrices. The lack of homogeneity can lead to undesirable properties, such as phase separation. Several methods have been reported for improvement of the dispersion of CNCs in polymer matrices. For example, CNCs were transferred from an aqueous to a nonaqueous system (e.g., organic media) [49-52], and surface modification of CNCs [53, 54], grafting-onto [22, 35], grafting-from [23] methods have been applied to increase the compatibility.

In the present study, we have attempted to alleviate the aggregation of SO-CNCs in the PCL matrix with minimal use of harmful organic solvents through a simple four-step process including (a) solvent exchange of aqueous SO-CNC suspension, (b) physical

mixing, (c) solvent casting, and (d) melt compounding extrusion shown in Figure 3.5. First, the SO-CNCs were dispersed in CH_3CN by solvent exchange and the PCL pellets were dissolved in CH_2Cl_2 which is miscible with CH_3CN. After that, the dissolved PCL was slowly added to the SO-CNCs suspended in CH_3CN under stirring at 40 °C in ultrasonic bath. The SO-CNCs/PCL nanocomposite filaments were prepared by solvent casting, followed by melt compounding extrusion using a twin-screw extruder.

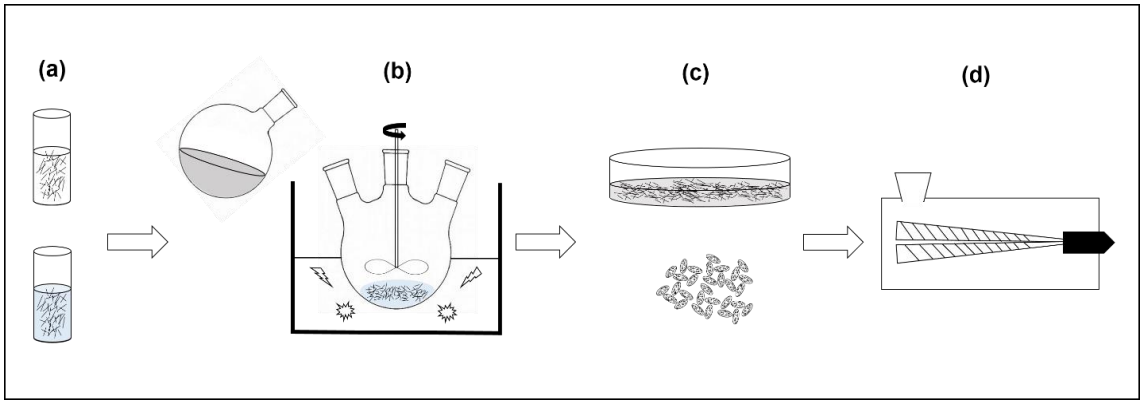

Figure 3.5. Schematic representation of SO-CNCs/PCL nanocomposites fabrication processes. (a) SO-CNCs were redispersed with acetonitrile by solvent exchange from an aqueous suspension. (b) Dissolved PCL in dichloromethane was slowly added to the solvent exchanged SO-CNC suspension and physically mixed in ultrasonic bath at 40 °C. (c) Solvent cast at room temperature followed by vacuum drying at 40 °C and the nanocomposites were cut to small pellets. (d) Melt compounding extrusion using a twin screw extruder at 80 °C.

The mechanical properties of the SO-CNCs/PCL nanocomposite filaments were established by tensile testing. Both the tensile strength and Young's (elastic) modulus are shown as a function of the SO-CNC content (wt %) in Figure 3.6. A reduction in ductility

was clearly observed with increasing SO-CNC content from the stress-strain curves. Pronounced mechanical reinforcement of PCL with addition of SO-CNCs was observed. The maximum values of both strength (18.2 ± 0.3 MPa) and Young's modulus (492.5 ± 44.1 MPa) were obtained at 10 wt % loading of SO-CNCs. These mechanical properties are very similar to those of human cancellous bone (tibia, tension test, strength: 2.54 ± 1.18 MPa, Young's modulus: 483 MPa [55]).

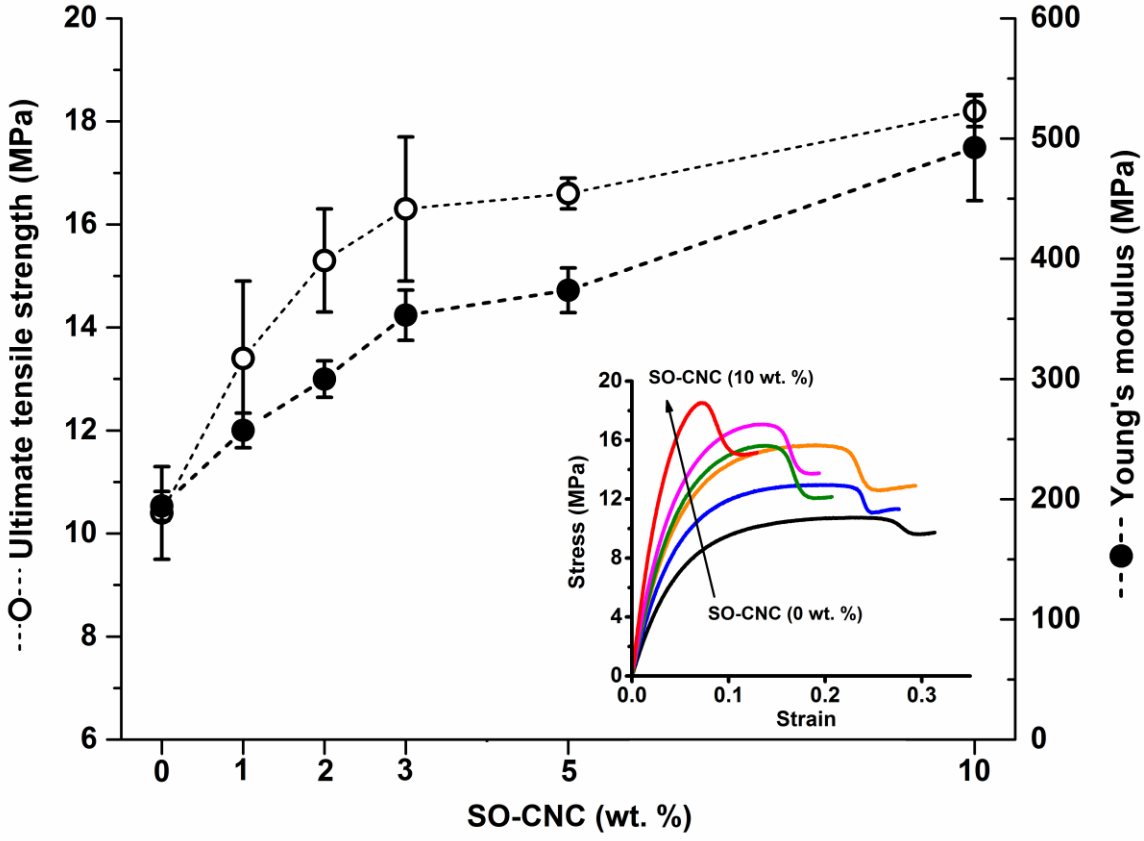

Figure 3.6. Mechanical properties of SO-CNCs/PCL nanocomposite filaments. Stress-strain curves of the nanocomposite filaments.

The thermal properties of the nanocomposites were evaluated by DSC (PCL0 and PCL10 are shown in Figure 3.7). The thermal transitions are summarized in Table 3.3. The 1st heating cycle from -75 °C to 100 °C was used to eliminate thermal histories during the nanocomposite fabrications, and identical DSC curves were observed for the 1st cooling and 2nd cooling cycles. The enthalpy of fusion, ΔH_f, was measured from the 2nd heating cycles (area under the melting peak) to calculate the crystallinity (X_c). The glass transition (T_g: ~ -64 °C) and melting (T_m: ~ 56 °C) temperatures were not influenced by the addition of SO-CNCs. However, the crystallization temperature (T_c) of the nanocomposites was increased about 4.5 °C with 1 wt % of SO-CNCs loading and it was slightly (about 1 °C) increased with the higher SO-CNC contents. The calculated ΔH_f gradually decreased from about 60 J/g (PCL0) to about 50 J/g (PCL10) and the crystallinity of the nanocomposites decreased from about 43 % to about 40 % with increasing SO-CNC content (from 0 to 10 wt %). A decrease in the degree of crystallinity is commonly observed with the presence of particulates. The particulates could act as nucleating agents and the filler-polymer interfaces act as heterogeneous nucleating sites [56]. The degree of perfection of the crystals can be affected by the restricted mobility of the chains, which does not allow the growth of well-developed lamellar crystals, and thus the degree of crystallinity was reduced [57]. The overall crystallization rate may also influenced by restricted diffusion of polymer chains to allow crystal growth, due to higher filler content [57]. Therefore, the SO-CNCs could act as nucleating agents as well as hindering crystal growth, by altering structural properties of the intercrystalline domain of PCL, resulting in decrease in crystallinity in SO-CNCs/PCL nanocomposites.

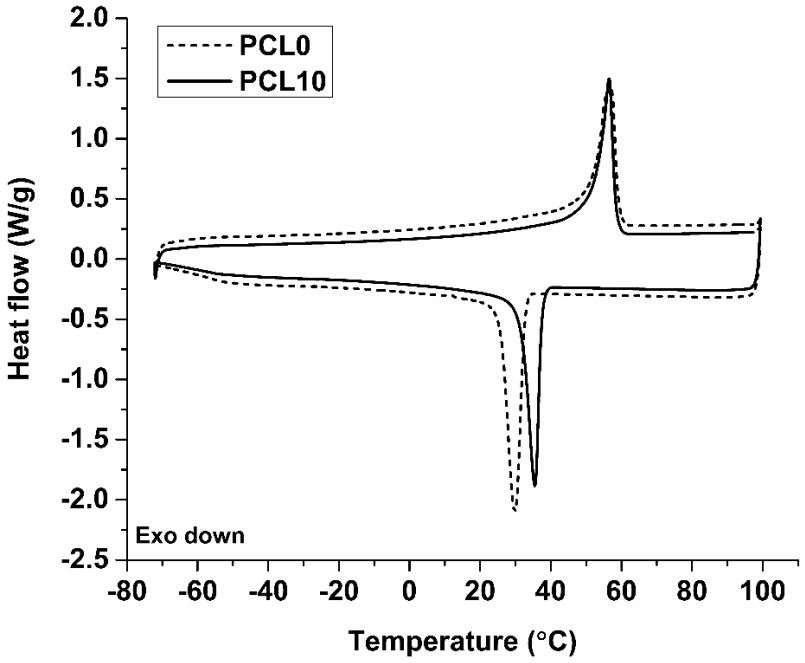

Figure 3.7. DSC curves (2nd heating and 2nd cooling) of PCL0 (0 wt % SO-CNC) and PCL10 (10 wt % SO-CNC content).

Table 3.3. Summary of mechanical properties, thermal transitions, crystallinity, and contact angle measurements of the SO-CNCs/PCL nanocomposites.

SO-CNC content	Mechanical properties		Thermal transitions			Crystallinity	Contact angle	
	Ultimate strength	Young's modulus	T_g	T_c	T_m	X_c	DI water	SBF
(wt %)	MPa	MPa	°C	°C	°C	%	°	°
0	10.4 ± 0.9	194.3 ± 12.1	-64.6 ± 0.6	30.2 ± 0.3	56.0 ± 0.6	42.9 ± 0.7	87.0 ± 1.1	88.8 ± 0.9
1	13.4 ± 1.5	257.2 ± 14.4	-64.9 ± 0.8	34.6 ± 0.2	56.1 ± 0.1	42.5 ± 0.4	85.5 ± 0.9	88.7 ± 0.6
2	15.3 ± 1.0	299.9 ± 15.2	-64.7 ± 0.5	34.5 ± 0.1	56.2 ± 0.1	42.1 ± 0.6	-	-
3	16.3 ± 1.4	353.1 ± 20.9	-64.4 ± 0.9	35.5 ± 0.1	56.1 ± 0.1	40.5 ± 0.6	84.5 ± 1.2	85.4 ± 1.1
5	16.6 ± 0.3	373.8 ± 18.6	-64.6 ± 0.8	35.2 ± 0.3	56.4 ± 0.2	39.9 ± 0.9	83.6 ± 1.4	85.2 ± 0.7
10	18.2 ± 0.3	492.5 ± 44.1	-64.5 ± 0.4	35.7 ± 0.2	56.4 ± 0.4	39.7 ± 0.5	82.6 ± 1.9	82.6 ± 0.5

T_g: glass transition temperature, T_c: crystallization temperature, and T_m: melting temperature. X_c calculated from 1st heating cycle: 49.6 ± 0.6% (PCL 0), 50.0 ± 1.0% (PCL 1), 50.6 ± 1.0% (PCL 2), 49.3 ± 0.6% (PCL 3), 49.0 ± 0.6% (PCL 5), and 48.9 ± 1.1% (PCL 10).

It is essential for implant materials to achieve an appropriate cellular response for tissue regeneration. The material surfaces will have direct contact with the biological environment (e.g., protein from blood and cells) on their surface and the resulting responses are critically important for successful implantation in tissue engineering applications. As bone scaffold materials, for example, the interactions between cell and material can promote preosteoblastic cell attachment, migration, proliferation, differentiation, and bioactivity (bone formation) [58]. It is commonly observed that hydrophilic surfaces provide a better environment for cell adhesion, but many bioresorbable polymers (e.g., PCL) exhibit hydrophobic nature. We expect that the hydrophilic SO-CNCs may influence the hydrophobicity of PCL. Therefore, both DI water and SBF contact angle measurements were performed with the SO-CNCs/PCL nanocomposites summarized in Table 2. The contact angle of PCL was decreased from 87.0 ± 1.1 ° (DI water) and 88.8 ± 0.9 ° to 82.6 ± 1.9 ° and 82.6 ± 0.5 °, respectively. This indicates that the overall hydrophobicity of PCL was decreased by addition of the hydrophilic SO-CNCs, and the reduced hydrophobicity may be beneficial, allowing polar head groups of cells to approach the surface due to its more wetted nature. It is difficult to draw any conclusive results based on the contact angle measurements, and the overall biocompatibility of CNCs and the SO-CNCs/PCL nanocomposites will be investigated.

3.5. Summary

With respect to the objective of this study, our summaries are:

- The negatively charged surface of CNCs by the sulfate groups (SH-CNCs) and the carboxyl groups (SO-CNCs) exhibited high probability of such cationic depositions in SBF (e.g., calcium ion), and thus the SO-CNCs showed more impact on the mineralization in terms of overall size increase resulting from ion depositions than the SH-CNCs;
- The mechanical properties of PCL were significantly reinforced by addition of SO-CNCs;
- The glass transition and melting temperatures were not influenced by addition of SO-CNCs, but the increased crystallization temperature and the lower enthalpy of fusion resulted in decreased crystallinity of the SO-CNC/PCL nanocomposites.
- The initial surface hydrophobicity of PCL was slightly reduced by addition of the hydrophilic SO-CNCs.

3.6. References

1. Kataoka, K., A. Harada, and Y. Nagasaki, *Block copolymer micelles for drug delivery: design, characterization and biological significance.* Advanced Drug Delivery Reviews, 2001. **47**(1): p. 113-131.

2. Mironov, V., V. Kasyanov, and R.R. Markwald, *Nanotechnology in vascular tissue engineering: from nanoscaffolding towards rapid vessel biofabrication.* Trends in Biotechnology, 2008. **26**(6): p. 338-344.

3. Panyam, J. and V. Labhasetwar, *Biodegradable nanoparticles for drug and gene delivery to cells and tissue*. Advanced Drug Delivery Reviews, 2012. **64**: p. 61-71.

4. Shi, J.J., et al., *Nanotechnology in Drug Delivery and Tissue Engineering: From Discovery to Applications.* Nano Letters, 2010. **10**(9): p. 3223-3230.

5. Stevens, M.M., *Biomaterials for bone tissue engineering.* Materials Today, 2008. **11**(5): p. 18-25.

6. Brechet, Y., et al., *Polymer based nanocomposites: Effect of filler-filler and filler-matrix interactions.* Advanced Engineering Materials, 2001. **3**(8): p. 571-577.

7. Albrektsson, T. and C. Johansson, *Osteoinduction, osteoconduction and osseointegration.* Eur Spine J, 2001. **10 Suppl 2**: p. S96-101.

8. Cohen, S., et al., *Design of synthetic polymeric structures for cell transplantation and tissue engineering.* Clin Mater, 1993. **13**(1-4): p. 3-10.

9. Hutmacher, D.W., *Scaffolds in tissue engineering bone and cartilage.* Biomaterials, 2000. **21**(24): p. 2529-43.

10. Sultana, N., *In: Biodegradable polymer-based scaffolds for bone tissue engineering*. 2013: SpringerBriefs in Applied Sciences and Technology.

11. Liu, H., E.B. Slamovich, and T.J. Webster, *Increased osteoblast functions among nanophase titania/poly(lactide-co-glycolide) composites of the highest nanometer surface roughness.* Journal of Biomedical Materials Research Part A, 2006. **78A**(4): p. 798-807.

12. Chen, L., et al., *Mechanical properties and in vitro evaluation of bioactivity and degradation of dexamethasone-releasing poly-D-L-lactide/nano-hydroxyapatite composite scaffolds.* Journal of the Mechanical Behavior of Biomedical Materials, 2013. **22**: p. 41-50.

13. Rodenas-Rochina, J., J. Ribelles, and M. Lebourg, *Comparative study of PCL-HAp and PCL-bioglass composite scaffolds for bone tissue engineering.* Journal of Materials Science-Materials in Medicine, 2013. **24**(5): p. 1293-1308.

14. Wei, G.B. and P.X. Ma, *Structure and properties of nano-hydroxyapatite/polymer composite scaffolds for bone tissue engineering.* Biomaterials, 2004. **25**(19): p. 4749-4757.

15. Wutticharoenmongkol, P., et al., *Preparation and characterization of novel bone scaffolds based on electrospun polycaprolactone fibers filled with nanoparticles.* Macromolecular Bioscience, 2006. **6**(1): p. 70-77.

16. Shi, X.F., et al., *Rheological behaviour and mechanical characterization of injectable poly(propylene fumarate)/single-walled carbon nanotube composites for bone tissue engineering.*

Nanotechnology, 2005. **16**(7): p. S531-S538.

17. Shi, X.F., et al., *Injectable nanocomposites of single-walled carbon nanotubes and biodegradable polymers for bone tissue engineering.* Biomacromolecules, 2006. **7**(7): p. 2237-2242.

18. Shi, X.F., et al., *Fabrication of porous ultra-short single-walled carbon nanotube nanocomposite scaffolds for bone tissue engineering.* Biomaterials, 2007. **28**(28): p. 4078-4090.

19. Pan, L.L., et al., *Multiwall carbon nanotubes/polycaprolactone composites for bone tissue engineering application.* Colloids and Surfaces B-Biointerfaces, 2012. **93**: p. 226-234.

20. Dufresne, A., *Polysaccharide nano crystal reinforced nanocomposites.* Canadian Journal of Chemistry-Revue Canadienne De Chimie, 2008. **86**(6): p. 484-494.

21. Chen, G.J., et al., *A Novel Thermoformable Bionanocomposite Based on Cellulose Nanocrystal-graft-Poly(epsilon-caprolactone).* Macromolecular Materials and Engineering, 2009. **294**(1): p. 59-67.

22. Habibi, Y. and A. Dufresne, *Highly filled bionanocomposites from functionalized polysaccharide nanocrystals.* Biomacromolecules, 2008. **9**(7): p. 1974-1980.

23. Habibi, Y., et al., *Bionanocomposites based on poly(epsilon-caprolactone)-grafted cellulose nanocrystals by ring-opening polymerization.* Journal of Materials Chemistry, 2008. **18**(41): p. 5002-5010.

24. Moon, R.J., et al., *Cellulose nanomaterials review: structure, properties and nanocomposites.* Chemical Society Reviews, 2011. **40**(7): p. 3941-3994.

25. Fleming, K., et al., *Cellulose crystallites: A new and robust liquid crystalline medium for the measurement of residual dipolar couplings.* Journal of the American Chemical Society, 2000. **122**(21): p. 5224-5225.

26. Lin, N., J. Huang, and A. Dufresne, *Preparation, properties and applications of polysaccharide nanocrystals in advanced functional nanomaterials: a review.* Nanoscale, 2012. **4**(11): p. 3274-3294.

27. Kovacs, T., et al., *An ecotoxicological characterization of nanocrystalline cellulose (NCC).* Nanotoxicology, 2010. **4**(3): p. 255-270.

28. Domingues, R.M.A., M.E. Gomes, and R.L. Reis, *The Potential of Cellulose Nanocrystals in Tissue Engineering Strategies.* Biomacromolecules, 2014. **15**(7): p. 2327-2346.

29. Colfen, H., *Biomineralization a Crystal-Clear View.* Nature Materials, 2010. **9**(12): p. 960-961.

30. Dey, A., et al., *The role of prenucleation clusters in surface-induced calcium phosphate crystallization.* Nature Materials, 2010. **9**(12): p. 1010-1014.

31. Sato, K., et al., *Crystal orientation of hydroxyapatite induced by ordered carboxyl groups.* Journal of Colloid and Interface Science, 2001. **240**(1): p. 133-138.

32. Weiner, S. and P.M. Dove, *An overview of biomineralization processes and the problem of the vital effect.* Biomineralization, 2003. **54**: p. 1-29.

33. Kokubo, T. and H. Takadama, *How useful is SBF in predicting in vivo bone bioactivity?* Biomaterials, 2006. **27**(15): p. 2907-2915.

34. Tanahashi, M. and T. Matsuda, *Surface functional group dependence on apatite formation on self-assembled monolayers in a simulated body fluid.* Journal of Biomedical Materials Research, 1997. **34**(3): p. 305-315.

35. Araki, J., M. Wada, and S. Kuga, *Steric stabilization of a cellulose microcrystal suspension by poly(ethylene glycol) grafting.* Langmuir, 2001. **17**(1): p. 21-27.

36. Habibi, Y., H. Chanzy, and M.R. Vignon, *TEMPO-mediated surface oxidation of cellulose whiskers.* Cellulose, 2006. **13**(6): p. 679-687.

37. Jiang, F., A.R. Esker, and M. Roman, *Acid-Catalyzed and Solvolytic Desulfation of H2SO4-Hydrolyzed Cellulose Nanocrystals.* Langmuir, 2010. **26**(23): p. 17919-17925.

38. Runt, J., *Polymers - Crystal Structure and Morphology 9. Thermal Analysis of Polymers.* Methods of experimental physics, 1980. **16**: p. 287-337.

39. Pitt, C.G., et al., *Aliphatic Polyesters .1. The Degradation of Poly(Epsilon-Caprolactone) Invivo.* Journal of Applied Polymer Science, 1981. **26**(11): p. 3779-3787.

40. Garcia, R., R. Magerle, and R. Perez, *Nanoscale compositional mapping with gentle forces.* Nature Materials, 2007. **6**(6): p. 405-411.

41. Garcia, R., et al., *Identification of nanoscale dissipation processes by dynamic atomic force microscopy.* Physical Review Letters, 2006. **97**(1).

42. Stark, M., et al., *From images to interactions: High-resolution phase imaging in tapping-mode atomic force microscopy.* Biophysical Journal, 2001. **80**(6): p. 3009-3018.

43. Tamayo, J. and R. Garcia, *Effects of elastic and inelastic interactions on phase contrast images in tapping-mode scanning force microscopy.* Applied Physics Letters, 1997. **71**(16): p. 2394-2396.

44. Cleveland, J.P., et al., *Energy dissipation in tapping-mode atomic force microscopy.* Applied Physics Letters, 1998. **72**(20): p. 2613-2615.

45. Czajkowsky, D.M., et al., *Direct visualization of surface charge in aqueous solution.* Ultramicroscopy, 1998. **74**(1-2): p. 1-5.

46. Boussu, K., et al., *Roughness and hydrophobicity studies of nanofiltration membranes using different modes of AFM.* Journal of Colloid and Interface Science, 2005. **286**(2): p. 632-638.

47. Zurick, K.M., C.L. Qin, and M.T. Bernards, *Mineralization induction effects of osteopontin, bone sialoprotein, and dentin phosphoprotein on a biomimetic collagen substrate.* Journal of Biomedical Materials Research Part A, 2013. **101**(6): p. 1571-1581.

48. Prasad, M., W.T. Butler, and C.L. Qin, *Dentin sialophosphoprotein in biomineralization.* Connective Tissue Research, 2010. **51**(5): p. 404-417.

49. Kvien, I., B.S. Tanem, and K. Oksman, *Characterization of cellulose whiskers and their nanocomposites by atomic force and electron microscopy.* Biomacromolecules, 2005. **6**(6): p. 3160-3165.

50. Samir, M.A.S.A., et al., *Preparation of cellulose whiskers reinforced nanocomposites from an organic medium suspension.* Macromolecules, 2004. **37**(4): p. 1386-1393.

51. Marcovich, N.E., et al., *Cellulose micro/nanocrystals reinforced polyurethane.* Journal of

Materials Research, 2006. **21**(4): p. 870-881.

52. van den Berg, O., J.R. Capadona, and C. Weder, *Preparation of homogeneous dispersions of tunicate cellulose whiskers in organic solvents.* Biomacromolecules, 2007. **8**(4): p. 1353-1357.

53. Grunert, M. and W.T. Winter, *Nanocomposites of cellulose acetate butyrate reinforced with cellulose nanocrystals.* Journal of Polymers and the Environment, 2002. **10**(1-2): p. 27-30.

54. Gousse, C., et al., *Surface silylation of cellulose microfibrils: preparation and rheological properties.* Polymer, 2004. **45**(5): p. 1569-1575.

55. Rohl, L., et al., *Tensile and Compressive Properties of Cancellous Bone.* Journal of Biomechanics, 1991. **24**(12): p. 1143-1149.

56. Hikosaka, M.Y., et al., *Montmorillonite (MMT) effect on the structure of poly(oxyethylene) (PEO)-MMT nanocomposites and silica-PEO-MMT hybrid materials.* Journal of Non-Crystalline Solids, 2006. **352**(32-35): p. 3705-3710.

57. Di Maio, E., et al., *Isothermal crystallization in PCL/clay nanocomposites investigated with thermal and rheometric methods.* Polymer, 2004. **45**(26): p. 8893-8900.

58. Wilson, C.J., et al., *Mediation of biomaterial-cell interactions by adsorbed proteins: A review.* Tissue Engineering, 2005. **11**(1-2): p. 1-18.

Chapter 4. Mechanical performance of 3D-printed porous nanocomposite bone scaffolds

4.1. Abstract

3D porous surface oxidized-cellulose nanocrystal (SO-CNC)/ poly(ε-caprolactone) (PCL) nanocomposite (SO-CNC content of up to 3 wt %) scaffolds with well-controlled pore size/shape and fully interconnected pores were successfully fabricated by 3D printing. The effect of SO-CNCs on the mechanical performance of scaffolds was assessed. The compression test (under dry condition in nitrogen gas) and short-term (1,000 s) creep tests (under dry and phosphate buffered saline (PBS) submersion conditions) showed that both the modulus and creep compliance of the scaffolds were remarkably improved by the small amount of SO-CNCs. In addition, the time-temperature superposition (TTS) principle was applied using the short-term creep data since TTS analysis could provide insightful and potentially useful information for the applications of scaffolds. The mechanical stability of the PCL scaffold was influenced by both temperature (> 30 °C) and submersion condition based on the long-term prediction from the TTS master curve. Especially, the rapid increase of creep compliance observed for scaffolds containing SO-CNCs in submersion conditions may be the results of plasticizer effect of phosphate buffered saline (PBS) (aqueous environment) in combination with the presence of hydrophilic SO-CNC aggregates in the PCL matrices.

4.2. Introduction

Scaffolds are among the major components of the bone tissue engineering approach. The main requirements for scaffolds are closely related to their ability to stimulate bone tissue regeneration through osteoconduction, osteoinduction and/or osseointegration. A tremendous number of studies have been conducted and many successful cases in specific areas of focus (i.e., osteoinduction and osteoconduction properties) have been suggested. However, it is an unquestionable fact that these proposals will be unfeasible if the scaffolds cannot provide sufficient mechanical stability. Unlike any other tissue engineered material, bone scaffolds require relatively strong mechanical properties, especially in the case of defects of critical size or larger. By definition, a critical-sized bone defect is the smallest tissue defect that will not completely heal over the lifespan of an animal and will not heal without intervention [1-3]. Therefore, mechanical instability could preclude many proposed materials from being viable options in bone scaffold applications of critical size or larger.

The mechanical stability of 3D porous scaffolds is a crucial factor in the repair of critical-sized defects that require long-term performance of the scaffolds during tissue regeneration. Therefore, scaffolds should be carefully designed to obtain adequate mechanical and structural properties found in natural bone in order to minimize failure [4-6]. The porosity and architecture of scaffolds are important because they profoundly influence metabolite transport, cell ingrowth, and vascularization by providing spatial organization composed of structural elements [7, 8]. The structural characteristics, including pore sizes/shape and interconnectivity of pores, in 3D constructions are

determined mainly by the fabrication techniques. Furthermore, scaffold mechanical stability varies with fabrication technique, and the porosity and interconnectivity of the pores have an inverse relationship with the mechanical stability of the scaffolds [8]. Therefore, ideal scaffolds should be fabricated by striking a balance between the structural elements and mechanical stability to optimize performance of the scaffolds for the desired applications.

A number of fabrication techniques have been developed for the fabrication of 3D porous structures and some of the common techniques were discussed in Chapter 2. For example, a variety of materials and fabrication techniques for the 3D porous scaffolds have previously been reported including particle/salt leaching [9, 10], freeze-drying [11], thermally induced phase separation [7] , and electrospining [12]. Although they may have several advantages in certain applications, those approaches cannot provide well-defined 3D porous configurations with fully controlled pore size, shape and interconnectivity of pores that could significantly influence the mechanical stability of the scaffold. On the other hand, rapid prototyping (RP) techniques, also known as solid free-form fabrication (SFF), have shown enormous potential in the field of biomedical engineering because they allow a customizable configuration through precise control using computer aided systems [13]. Other technologies, including Fused Deposition Modeling (FDM) and RP, are based upon concepts similar to SFF, where a 3D object of desired design is built using computer-aided design (CAD program) using raw materials, such as metals, ceramics, and polymers, in a layer-by-layer fashion. Recently among the SFF techniques, 3D printing has drawn considerable attention and opened up the customizable implants for a

wide range of tissue engineering applications because of the ability to directly create complex 3D porous scaffold structures without special molds and toxic solvents [13-15]. The 3D printing technology was developed and patented by Massachusetts Institute of Technology in 1993 [16], but the first to develop this technology was Charles Hull in 1984, who named it Stereo lithography [17].

In particular, poly(ε-caprolactone) (PCL) is a potential candidate for bone scaffolds that have been preferably fabricated by 3D printing because of its good processibility and slower bioresorption rate over other polymers [18-21]. PCL is a hydrophobic and semi-crystalline linear polymer which belongs to the family of aliphatic polyesters. It had long been used for biomedical applications, such as drug delivery systems and medical devices [22, 23]. However, there are critical challenges arising from the insufficient mechanical properties of PCL in load-bearing bone tissue engineering applications. Our previous studies have shown successful mechanical reinforcement of PCL nanocomposites by incorporation of cellulose nanocrystals (CNCs). In addition, the negatively charged carboxyl groups on the surface oxidized-CNCs (SO-CNCs) provided a strong capacity to bind calcium ions (i.e., calcium chelating properties) in simulated body fluid (1x) *in vitro* thereby indicating a potential role in biomineralization *in vivo* (bioactivity).

In the present study, we attempted to fabricate porous SO-CNC/PCL nanocomposite scaffolds by 3D printing techniques, in order to achieve a precise control of scaffold properties, such as pore geometry, size, and interconnectivity. The mechanical properties of these 3D porous scaffolds were evaluated using compression tests. In addition, the

creep behavior of the scaffolds has been studied using a short-term compressive-torsion creep test at different temperatures under dry and submersion conditions to provide more relevant information for potential bone tissue engineering applications.

4.3. Experimental

4.3.1. Materials

Bleached softwood sulfite dissolving-grade pulp (Temalfa 93A) was kindly provided by Tembec Inc. (Témiscaming, QC, CA). Sulfuric acid (H_2SO_4, 96.2 wt %), acetonitrile (CH_3CN, HPLC Grade), dichloromethane (CH_2Cl_2), and sodium hydroxide (NaOH, 0.5M) were purchased from Fisher Scientific. 2,2,6,6,-Tetramethyl-1-piperidinyloxy (TEMPO, $C_9H_{18}NO$, free radical, 98%), sodium hypochlorite solution (NaOCl, reagent grade, available chlorine 10-15%), methanol (CH_3OH, anhydrous, 99.8%) polycaprolactone (PCL, $(C_6H_{10}O_2)_n$, M_n: 70,000-90,000) were purchased from Sigma-Aldrich. Sodium bromide (NaBr, 99+%, extra pure, anhydrous) was purchased from Acros organics.

4.3.2. Methods

4.3.2.1. Porous scaffold fabrication by 3D printing

The preparation or SO-CNCs and fabrication of SO-CNC/PCL nanocomposite were described in Chapter 3.

3D porous SO-CNC/PCL nanocomposite scaffolds were fabricated with a Thing-O-Matic 3D printer (MakerBot® Industries, LLC.). The 3D printer is controlled via G-code, a computer numerical control programming language in stl file format. The 3D design file is translated to G-code with ReplicatorG, an open source 3D printing program. In this process, the design is converted into a sequence of slices used for the layer by layer printing of the 3D object. In addition, the generated G-code contains details about the process parameters, such as stage (X and Y directions) and nozzle movement (Z direction) and speed, nozzle temperature, and feed rate of the filament, controlled by the motor speed (e.g., nozzle size: 0.3 mm, nozzle temperature: 185 °C, extruder motor speed: 1.0 rpm, feed rate: 1800 mm/min) . SO-CNC/PCL nanocomposite filaments (PCL 0, PCL 1, PCL 3 with 0, 1, and 3 wt % SO-CNCs, respectively) were used to fabricate the scaffolds.

4.3.2.2. Compression test

Compression testing of the porous SO-CNC/PCL nanocomposite scaffolds (diameter: 8 mm, thickness: 2 mm) were performed with an MTS Sintech 10/GL Material Testing Workstation equipped with a 5,000 N load cell. A cross head speed of 0.5 mm/min was employed under ambient conditions (in air at room temperature). The compressive modulus was determined from the linear elastic region of the stress-strain curve. Measurements were carried out in triplicate and results averaged.

4.3.2.3. Compressive-torsion mode creep test

Disc shaped samples (8 mm in diameter, 2 mm in thickness) porous scaffolds were tested in parallel-plate compressive-torsion mode using a TA Instruments AR 2000 rheometer. Torsional slippage was prevented with a compressive clamping force (static normal force: 10 N). Creep tests were performed both in dry and in solvent submersion conditions. All specimens were stored in a desiccator prior to testing. On the other hand, specimens for submersion tests were immersed in PBS and a vacuum was applied for 10 min in order to remove trapped air within the pores of scaffold before testing. To maintain specimen immersion during analysis, the submersion test was conducted such that the bottom plate was surrounded by a stainless steel cup. A thin layer of silicon oil was applied on the top of the PBS and the stainless steel cup was covered with an aluminum pan to prevent evaporation during the test. All tests were performed under anhydrous nitrogen (N_2) gas and liquid N_2 was used to control the temperature. Creep tests were performed and duplicated at different temperatures, 5, 10, 15, 20, 25, 30, 35, 37, 40 and 45 °C. The lower (5 °C) and upper (45 °C) were chosen based on the freezing point of PBS (≈ 0 °C) and melting point (≈ 56 °C) of PCL.

The linear viscoelastic response (LVR) region was determined using a stress sweep (oscillation stress: 100-100,000 Pa, frequency: 1 Hz). The measurements were conducted at lower (5 °C) and upper (45 °C) temperature limits with PCL 0 and PCL 3 both in dry and in submersion conditions. Prior to the creep test the stress limit was determined from the stress-strain curves of the stress sweep tests and was fixed at 15,000 Pa, to ensure that the creep tests were confined to the LVR regime.

The temperature range was from 5 ℃ to 45 ℃, in 5 ℃ steps, and the isothermal tests were run on the same specimen in the temperature range. The 15,000 Pa creep stress (shear stress) was applied for 1,000 s at each temperature. Before each test, the specimen was equilibrated for 5 min at each temperature, in order to ensure the correct temperature of the specimen.

Master curves at 37 °C of creep compliance were constructed using a time-temperature superposition (TTS) concept. The horizontal shift factor (a_T) data points were fitted with an Arrhenius expression.

4.4. Results and discussion

SO-CNC/PCL nanocomposite scaffolds with well-controlled pore size and fully interconnected pores, fabricated by 3D printing, are shown in Figure 4.1. The SO-CNC/PCL nanocomposites with different concentrations of SO-CNC (0 wt %: PCL 0, 1 wt %: PCL 1 and 3 wt %: PCL 3) were extruded through a 0.3 mm nozzle and plotted as layer-by-layer deposition on a stage. Each layer was deposited with an angle of 90 ° and the fabricated scaffolds have the diameter of a single strand was 300 μm, with a pore size of 500 μm. Porosity of the scaffold was estimated based on the ratio of pore volume to its total volume, as ca. 66 %.

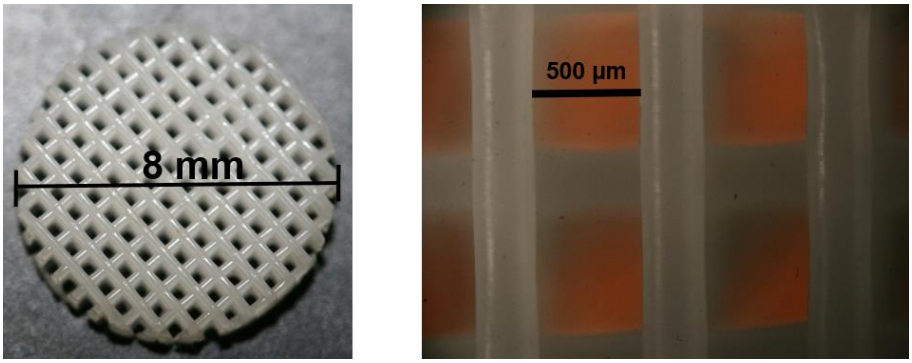

Figure 4.1 3D porous SO-CNC/PCL (PCL 1, 1 wt % of SO-CNC) nanocomposite scaffold (left) and the pore size (right).

The pore sizes within the scaffolds should be carefully controlled and tailored to the application since different pore sizes are required for different cell types and tissue regeneration. For example, it has been reported that the optimum pore size for osteoid development is about 40-100 µm and for bone regeneration about 100-400 µm [24, 25]. Also, Green *et al.* [26] suggested that different pore diameters are required to stimulate fibrovascular growth (15-50 µm) and osteoid formation (50-150 µm), with pores in the range of 150-500 µm leading directly to mineralized bone. The 3D printer employed here can create a pore size as small as 300 µm.

To determine the reinforcing effect of the SO-CNC on the compressive properties of the scaffold, PCL scaffolds with three different SO-CNC contents (0, 1 and 3 wt %) were evaluated (PCL 0, PCL 1 and PCL 3, respectively). Stress-strain curves from the SO-CNC/PCL nanocomposite scaffolds compression test are shown in Figure 4.2. The PCL 0 scaffold exhibited three distinct regions; a linear-elastic region and a plateau region with

a relatively constant stress, followed by a densification region of steeply increasing stress, under compression loading. Any toe region due to the initial settling of the specimen was neglected. However, upon the addition of SO-CNC, the plateau region became a transition region with linearly increasing stress between the linear-elastic and densification regions. Also, the rate of stress increased rapidly for those regions with higher SO-CNC content (PCL 3). The compressive modulus was calculated from the slope of the initial linear region of the stress-strain curve (Figure 4.2). The compression moduli were significantly increased with increasing SO-CNC content from 9.3 ± 2.6 MPa for PCL 0 to 31.5 ± 4.3 MPa for PCL 3 as shown in Figure 4.3. Park *et al.* [14] demonstrated that the mechanical properties of 3D printed PCL scaffolds could be easily adjusted by altering the strand and pore size of the scaffolds, and the compressive moduli of the PCL scaffolds were in the range of 3.5-10.3 MPa with 128-320 μm pore size. Therefore, in comparison with the present study, the mechanical properties of PCL scaffolds were remarkably reinforced by the small amount of SO-CNCs.

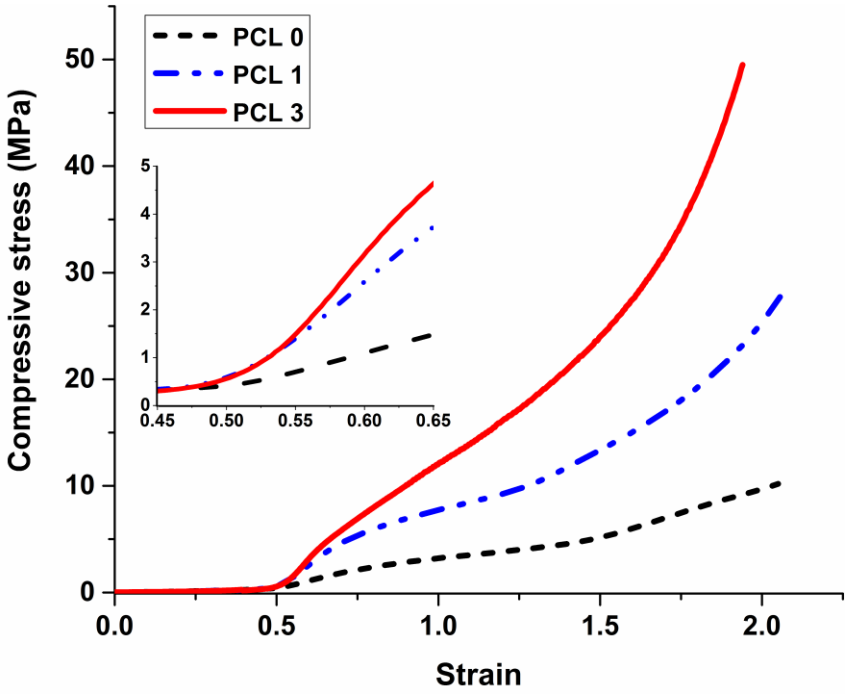

Figure 4.2. Stress-strain curves of the 3D porous SO-CNC/PCL nanocomposite scaffolds compression test.

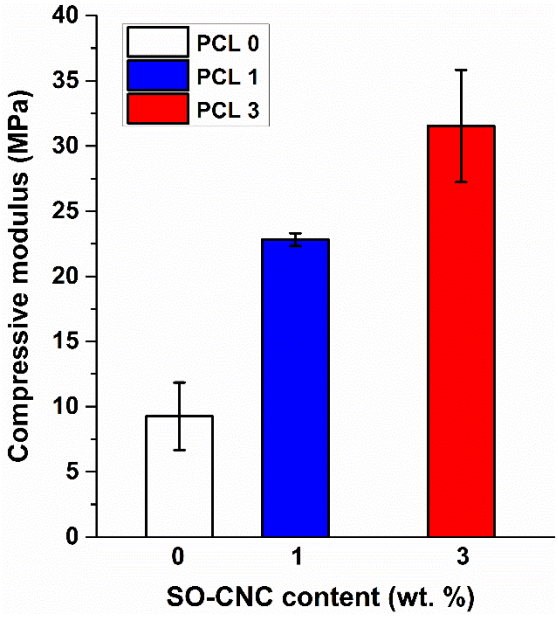

Figure 4.3. Compression modulus of the 3D porous SO-CNC/PCL nanocomposite scaffolds compression test.

The mechanical reinforcing effects of SO-CNCs on the PCL matrix were revealed from the previous (tensile test, chapter 3) and current studies (compression test). Considering the application of scaffolds in reality, however, it is necessary to address the changes for structure property relationships (e.g., interphase and bulk properties) which could influence the long-term mechanical properties of the SO-CNC/PCL nanocomposites. Although most of tissue engineered scaffolds are designed as implant materials, far less attention has been paid to long duration tests, especially those in wet conditions. In our case, thus, the mechanical performance of scaffolds was assessed with the compressive-torsion mode creep test under both dry and PBS submersion conditions.

Creep rates were determined from strain-time curves (Figure 4.4). Each data point was acquired at 1,000 s as a function of temperature under constant stress (15,000 Pa). Addition of SO-CNCs resulted in a significant reduction of strain in the dry condition and there was no difference in the mechanical performance behavior of PCL 1 and PCL 3. For PCL0, the initial strain was decreased at lower temperature in PBS submersion, but the rate was rapidly increased above 30 °C and reached a similar level of strain as in the dry condition. Interestingly, however, the effects of SO-CNCs on the creep rate were apparently different between dry and submersion conditions. The increase of strain with temperature accelerated above 30 °C for both PCL 1 and PCL 3 in submersion conditions compared to the dry condition. Material softening near the melting temperature is commonly observed for semicrystalline thermoplastic polymers and this phenomenon applies to the PCL scaffolds. However, the softening of PCL with increasing temperature strongly suppressed upon the addition of SO-CNC only under the dry condition.

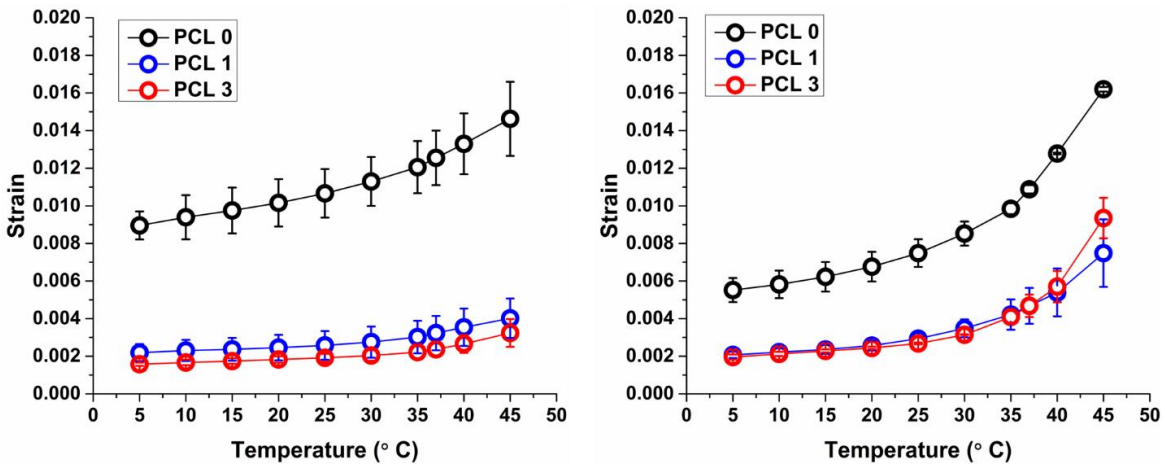

Figure 4.4. Effect of temperature on the scaffold strain (N_2 gas dry condition: left, PBS submersion condition: right) at 1,000 s of compressive-torsion mode creep test.

The effect of temperature on the shear modulus of the scaffolds is shown in Figure 4.5. Each data point was acquired at 1,000 s creep test as a function of temperature under constant stress (15,000 Pa). For PCL 0, the modulus between the responses decreased slightly with increasing temperature, but no noticeable change was observed in dry vs. submersion conditions. However, scaffold moduli decreased significantly with temperature when SO-CNCs were present, especially above 30 °C. Greater decreases in modulus were observed under submersion conditions. From the above results, it was revealed that the mechanical reinforcing effects of SO-CNCs were influenced both by temperature (≥ 30 °C) and time under constant stress, and these phenomena were more obvious under wet conditions (submersion) for the PCL matrices.

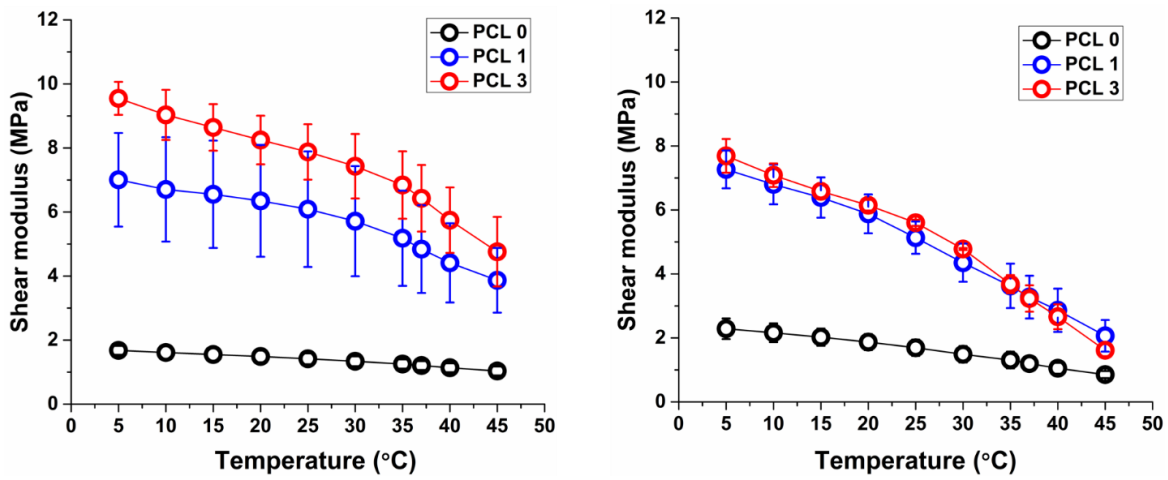

Figure 4.5. Effects of temperature on the shear modulus of scaffolds (dry: left, PBS submersion: right) at 1,000 s of compressive-torsion mode creep test.

In order to gain deeper insight into the effects of SO-CNCs in PCL matrices, as well as the impact of submersion conditions upon the creep behavior and mechanism, the time temperature superposition (TTS) concept was applied. TTS has been widely used to estimate the long-term performance of materials, such as polymeric materials and composites, with short-term test data [27-29]. Master curves for creep can be constructed by using the TTS principle [30] since effects of time and temperature on viscoelasticity of polymers are equivalent and molecular motions that influence the mechanical properties of polymer are dependent on both the temperature and time scale.

In the current studies, creep experiments of SO-CNC/PCL nanocomposite scaffolds were performed at a temperature range from 5 °C to 45 °C. This temperature range was chosen based on the PBS submersion experiments and the thermal properties of the nanocomposites (Table 4.1). All the individual creep curves corresponding to different

temperature levels were shifted along the logarithmic time axis to superimpose to a master curve. Since the reference temperature (37 °C, body temperature) is far away from the glass transition temperature (~ -65 °C), the dependence of the shift factor with the temperature can be described by an Arrhenius type equation [31]. The shift factors can be correlated with the temperature by Arrhenius equation as follows:

$$\log a_{T_0}(T) = \frac{\Delta H}{2.303R}\left(\frac{1}{T} - \frac{1}{T_{ref}}\right)$$

where ΔH is the activation energy (KJ/mol), R is the gas constant (8.314 J/°K·mol), T is the test temperature and T_{ref} is the reference temperature (in our case 37 °C). The correlation between the horizontal shift factor and temperature using the Arrhenius equation is shown in Figure 4.6. The results of master curves for the scaffolds both in dry and in submersion conditions were obtained by shifting the compliance data at different temperatures, taking 37 °C as the reference temperature because it is the body temperature shown in Figure 4.7.

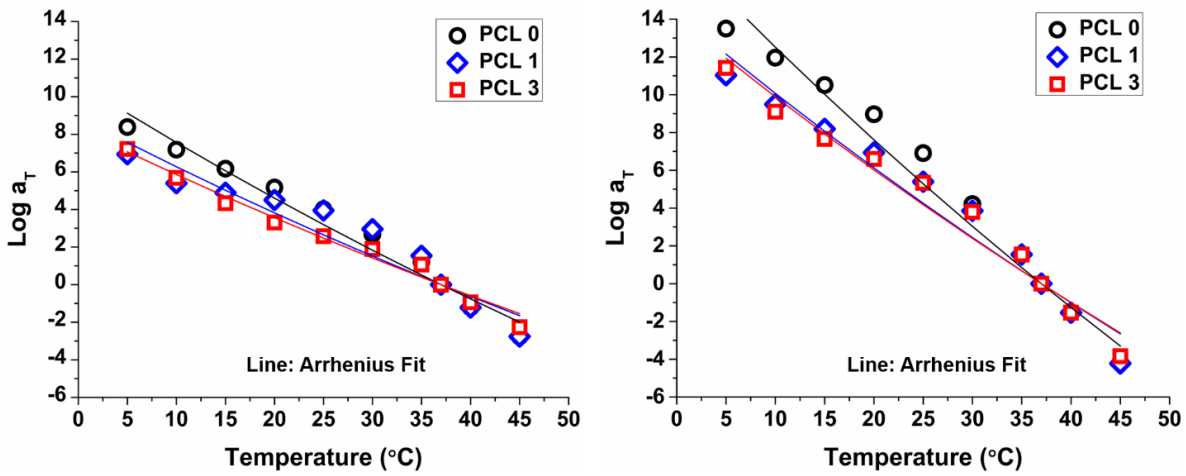

Figure 4.6. Time-temperature shift factors (a_T) as a function of temperature. The straight line corresponds to the Arrhenius fit of the data.

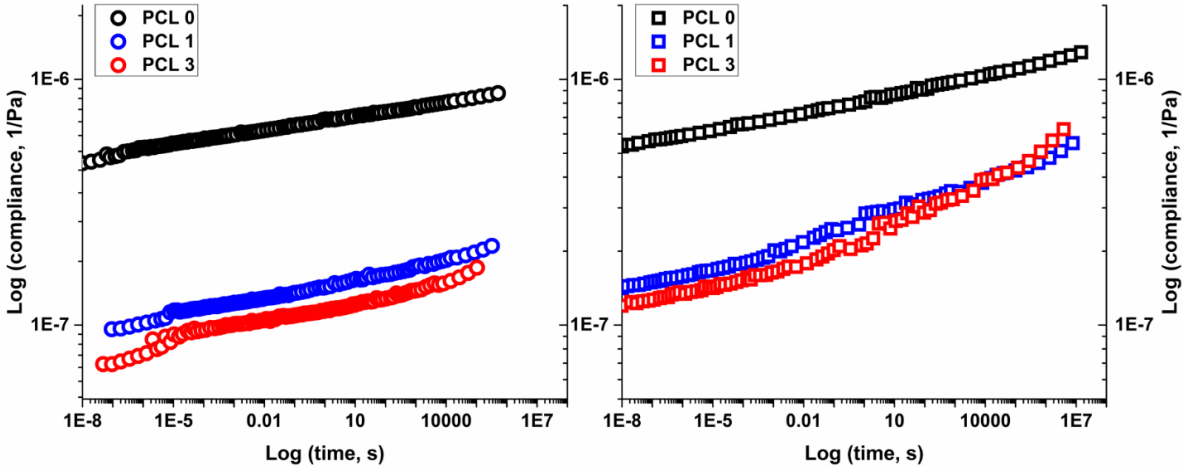

Figure 4.7. Master curve at 37 °C, dry (left) and PBS submersion (right).

Based on the master curves, the creep compliance of the scaffolds with increasing SO-CNC content was obviously lower than that of PCL 0 (PCL 0 >> PCL 1 > PCL 3). However, it is interesting to note that the increment of compliance as a function of time exhibited a tendency to increase faster in submersion conditions than in the dry condition. The effects of SO-CNC with higher concentration (PCL 3) became more pronounced as similar as the earlier results (strain-, shear modulus-temperature curves) because the significant increase of creep compliance around 10,000 s correspond to the creep test results from the higher temperature than the reference temperature (37 °C). These findings indicated that the PCL matrices could exhibit polymer deformation due to stress relaxation over a long period of time at 37 °C under the submersion condition. Also, the SO-CNCs provided better mechanical stability by reinforcing the PCL matrices in dry conditions. Even though there is a tendency towards faster increase in creep compliance at higher temperature/time and under submersion condition, the addition of SO-CNCs to PCL scaffolds remarkably improved creep resistance (decreased creep compliance).

Creep (constant stress) in semicrystalline polymers above their glass transition temperature has been attributed to stress relaxation (i.e., molecular motions) in the amorphous regions resulting in the morphological changes of polymer even within the LVR regime [32]. In order to explain the reinforcing effects of nanofillers, several models have been proposed [32-34] and are described below. The nanofillers could act as heterogeneous nucleation agents and may trigger the growth of smaller spherulites. The nanofillers are either occluded in the spherulites (in “interlamellar” and “interfibrillar” regions) or pushed into the interspherulitic boundary layer. Alternatively, they can only

be located in the amorphous phase and be responsible for the reinforcing effect if even (or homogeneous)-dispersion of nanofillers is achieved. If so, the initial improvement of the creep resistance is predominantly due to the limiting effect of nanofillers on molecular motions in the amorphous phase.

In addition, Ahmed *et al.* [35] and Di *et al.* [36] have reported similar phenomena with PCL/nanoclay and PCL/organoclay composites, respectively. The melt crystallization temperature (T_c) was increased gradually and the enthalpy of fusion (ΔH_f) decreased systematically with increasing nanofiller loading. The crystallinity (X_c) of the PCL/nanoclay (10 wt % nanoclay) nanocomposite decreased about 9 % from that of neat PCL [35]. In our system, the crystallinity of PCL decreased about 2.5 % at a SO-CNC content of 3 wt % (Table 4.1). Wu *et al.* [37] have suggested that carbon nanotubes promote crystallization of the PCL matrix, but the heterogeneous nucleation leads to the formation of a more defect ridden crystalline lamella and less ordered crystals of PCL, resulting in a decrease in the enthalpy of fusion.

Table 4.1. Summary of thermal transitions and crystallinity of the SO-CNC/PCL nanocomposites.

	Crystallization temperature T_c (°C)	**Crystallinity X_c (%)**	**Enthalpy of fusion ΔH_f (J/g)**
PCL 0	**30.2 ± 0.3**	**42.9 ± 0.7**	**59.9 ± 1.0**
PCL 1	**34.6 ± 0.2**	**42.5 ±0.5**	**58.8 ± 0.6**
PCL 3	**35.5 ± 0.1**	**40.5 ± 0.6**	**54.8 ±0.9**

**** T_g (~ -65 °C) and T_m (~ 56 °C) were not influenced by the addition of SO-CNC.***

On the other hand, the evidence indicates that even (or homogeneous)-dispersion of SO-CNCs in PCL matrices was achieved through the nanocomposite fabrication processes used in this work (solvent exchange, physical mixing and solvent casting, followed by melt compounding extrusion), based on the gradual mechanical reinforcement of PCL with increasing SO-CNC content shown by the tensile testing in Chapter 3. However, considering the hydrophilicity of SO-CNC and hydrophobicity of PCL, it is highly possible that the SO-CNCs have aggregated to some extent within the PCL matrices during the fabrication processes. Optical microscopy images of SO-CNC/PCL nanocomposites after heating at 300 °C are shown in Figure 4.8. Since the degradation temperatures of SO-CNC and PCL 0 are around 250 °C and 380 °C, respectively (see Appendix C), the brown color indicates degraded SO-CNC. Overall color of the PCL 1 and PCL 3 was changed to brown compared to that of PCL 0 (white), and this is an indication of the well-dispersed SO-CNCs in the PCL matrices. However, several dark spots due to the aggregation of SO-CNCs were observed for both PCL 1 and PCL 3 (see Appendix D). Similarly, AFM phase images were obtained from a freshly cracked surface of the SO-CNC/PCL nanocomposites along the flow direction (extrusion) shown in Figure 4.9. Tapping-mode AFM provides information about the topography and surface properties of the specimen surface, such as stiffness, viscoelasticity, or surface-adhesion energy measured by the phase shift (also known as phase lag) of the cantilever oscillation relative to the driving signal as reference [38-40]. In addition, the phase shift allows identification of regions of different interactions by the amount of energy dissipated in the tip-sample interaction, and thus it was used to directly visualize the different surface charge characteristics [41-43]. Therefore, the blue color regions from

the AFM phase images (PCL 1 and PCL 3) may be due to different viscoelastic properties between SO-CNC and PCL. Some of the individual SO-CNCs were present both in PCL 1 and PCL 3, but the blue color phase contrast domain was larger in PCL 3, which could be due to aggregation of SO-CNCs or phase separation between the SO-CNCs and PCL matrices. Especially, the rapid increase in creep compliance in submersion condition may be the results of a plasticizer effect of the PBS (aqueous environment) due to the presence of hydrophilic SO-CNCs or instability of the interfacial adhesion between the PCL matrix and SO-CNCs.

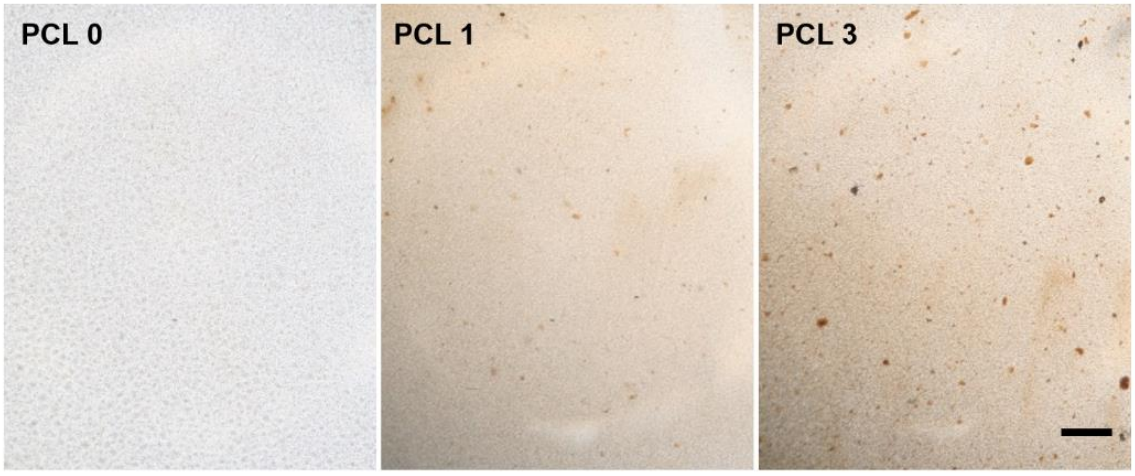

Figure 4.8. Optical microscopy images of SO-CNCs/PCL nanocomposites after the degradation of SO-CNCs at 300 °C. Scale bar: 100 µm.

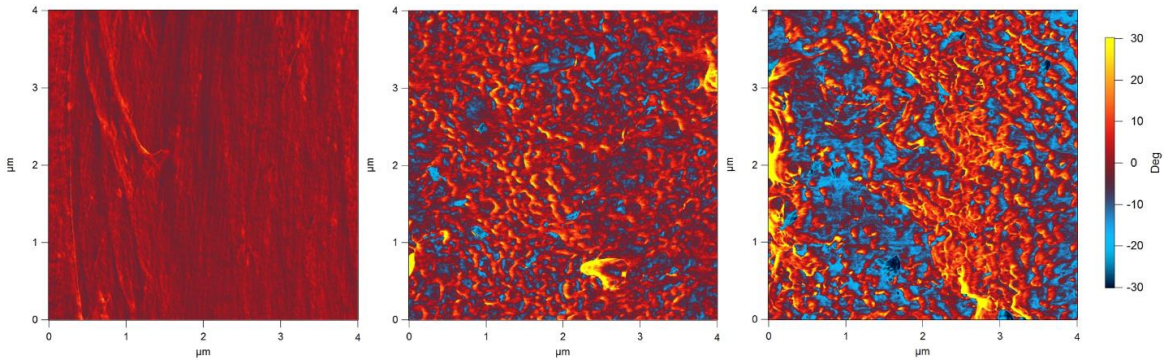

Figure 4.9. AFM phase images of SO-CNCs/PCL nanocomposites (PCL 0: left, PCL 1: middle, PCL 3: right). Scan size: 4 µm.

4.5. Summary

With respect to the objective of this study, our conclusions are:

- 3D porous SO-CNC/PCL nanocomposite (SO-CNC content of up to 3 wt %) scaffolds with the well-controlled pore size/shape and fully interconnected pores were fabricated by 3D printing;
- The compressive modulus of the scaffolds was significantly improved by addition of SO-CNCs;
- The creep compliance of the scaffolds were remarkably reduced by the small amounts of SO-CNCs;
- The mechanical stability of the PCL 3 scaffold was influenced by both temperature (> 30 °C) and submersion condition based on the long-term prediction from the TTS master curve.

4.6. References

1. Schmitz, J.P. and Hollinger, J.O., *The Critical Size Defect as an Experimental Model for Craniomandibulofacial Nonunions.* Clinical Orthopaedics and Related Research, 1986. **205**: p. 299-308.

2. Takagi, K. and M.R. Urist, *The reaction of the dura to bone morphogenetic protein (BMP) in repair of skull defects.* Ann Surg, 1982. **196**(1): p. 100-9.

3. Spicer, P.P., et al., *Evaluation of bone regeneration using the rat critical size calvarial defect.* Nat Protoc, 2012. **7**(10): p. 1918-29.

4. Caplan, A.I., *Tissue engineering designs for the future: new logics, old molecules.* Tissue Eng, 2000. **6**(1): p. 1-8.

5. Sharma, B. and J.H. Elisseeff, *Engineering structurally organized cartilage and bone tissues.* Ann Biomed Eng, 2004. **32**(1): p. 148-59.

6. Meinel, L., et al., *Silk implants for the healing of critical size bone defects.* Bone, 2005. **37**(5): p. 688-98.

7. Hutmacher, D.W., *Scaffolds in tissue engineering bone and cartilage.* Biomaterials, 2000. **21**(24): p. 2529-43.

8. Lam, C.X.F., et al., *Scaffold development using 3D printing with a starch-based polymer.* Materials Science and Engineering: C, 2002. **20**(1–2): p. 49-56.

9. Cao, H. and N. Kuboyama, *A biodegradable porous composite scaffold of PGA/beta-TCP for bone tissue engineering.* Bone, 2010. **46**(2): p. 386-95.

10. Stoppato, M., et al., *Influence of scaffold pore size on collagen I development: A new in vitro evaluation perspective.* Journal of Bioactive and Compatible Polymers, 2013. **28**(1): p. 16-32.

11. Sultana, N. and M. Wang, *Fabrication of HA/PHBV composite scaffolds through the emulsion freezing/freeze-drying process and characterisation of the scaffolds.* Journal of Materials Science-Materials in Medicine, 2008. **19**(7): p. 2555-2561.

12. Hackett, J.M., et al., *Electrospun Biocomposite Polycaprolactone/Collagen Tubes as Scaffolds for Neural Stem Cell Differentiation.* Materials, 2010. **3**(6): p. 3714-3728.

13. Schieker, M., et al., *Biomaterials as Scaffold for Bone Tissue Engineering.* European Journal of Trauma, 2006. **32**(2): p. 114-124.

14. Park, S., et al., *3D polycaprolactone scaffolds with controlled pore structure using a rapid prototyping system.* Journal of Materials Science-Materials in Medicine, 2009. **20**(1): p. 229-234.

15. Bose, S., S. Vahabzadeh, and A. Bandyopadhyay, *Bone tissue engineering using 3D printing.* Materials Today, 2013. **16**(12): p. 496-504.

16. Emanuel, M.S., Somerville; John, S. Haggerty, Lincoln; Michael, J. Cima, Lexington; Paul, A. Williams, Concord, all of Mass., *Three-dimensional printing techniques*. 1993, Massachusetts Institute of Technology, Cambridge, Mass.

17. Charles, W.H., *Apparatus for production of three-dimensional objects by stereolithography*. 1986, UVP, Inc., San Gabriel, Calif: United States Patent.

18. Park, S.A., S.H. Lee, and W.D. Kim, *Fabrication of porous polycaprolactone/hydroxyapatite (PCL/HA) blend scaffolds using a 3D plotting system for bone tissue engineering.* Bioprocess and Biosystems Engineering, 2011. **34**(4): p. 505-513.

19. Sobral, J.M., et al., *Three-dimensional plotted scaffolds with controlled pore size gradients: Effect of scaffold geometry on mechanical performance and cell seeding efficiency.* Acta Biomater, 2011. **7**(3): p. 1009-18.

20. Hoque, M.E., et al., *Processing of Polycaprolactone and Polycaprolactone-Based Copolymers into 3D Scaffolds, and Their Cellular Responses.* Tissue Engineering Part A, 2009. **15**(10): p. 3013-3024.

21. Hutmacher, D.W., et al., *Mechanical properties and cell cultural response of polycaprolactone scaffolds designed and fabricated via fused deposition modeling.* Journal of Biomedical Materials Research, 2001. **55**(2): p. 203-216.

22. Pitt, C.G., et al., *Aliphatic polyesters II. The degradation of poly (DL-lactide), poly (epsilon-caprolactone), and their copolymers in vivo.* Biomaterials, 1981. **2**(4): p. 215-20.

23. Woodruff, M.A. and D.W. Hutmacher, *The return of a forgotten polymer-Polycaprolactone in the 21st century.* Progress in Polymer Science, 2010. **35**(10): p. 1217-1256.

24. Brekke, J.H. and J.M. Toth, *Principles of tissue engineering applied to programmable osteogenesis.* Journal of biomedical materials research, 1998. **43**(4): p. 380-98.

25. Whang, K., et al., *Engineering bone regeneration with bioabsorbable scaffolds with novel microarchitecture.* Tissue Engineering, 1999. **5**(1): p. 35-51.

26. Green, D., et al., *The potential of biomimesis in bone tissue engineering: lessons from the design and synthesis of invertebrate skeletons.* Bone, 2002. **30**(6): p. 810-815.

27. Schapery, R.A., *Viscoelastic Behavior and Analysis of Composite Materials*. 1974.

28. Miyano, Y., et al., *Loading rate and temperature dependence on flexural fatigue behavior of a satin woven CFRP laminate.* Journal of Composite Materials, 1994. **28**(13): p. 1250-1260.

29. Miyano, Y., et al., *Prediction of flexural fatigue strength of CRFP composites under arbitrary frequency, stress ratio and temperature.* Journal of Composite Materials, 1997. **31**(6): p. 619-638.

30. Ward, I.M. and J. Sweeney, *Mechanical properties of solid polymers*. 2012: John Wiley & Sons.

31. Williams, M.L., R.F. Landel, and J.D. Ferry, *The Temperature Dependence of Relaxation Mechanisms in Amorphous Polymers and Other Glass-forming Liquids.* Journal of the American Chemical Society, 1955. **77**(14): p. 3701-3707.

32. Haag, R. and P. Sinpayakun, *A Review of Creep Resistance of Nano-Scale Reinforcing Thermoplastics.*

33. Ganß, M., et al., *Temperature Dependence of Creep Behavior of PP–MWNT Nanocomposites.* Macromolecular Rapid Communications, 2007. **28**(16): p. 1624-1633.

34. Yang, J.-L., et al., *On the characterization of tensile creep resistance of polyamide 66 nanocomposites. Part I. Experimental results and general discussions.* Polymer, 2006. **47**(8): p. 2791-2801.

35. Ahmed, J., et al., *Rheological, thermal and structural behavior of poly (ε-caprolactone) and nanoclay blended films.* Journal of Food Engineering, 2012. **111**(4): p. 580-589.

36. Di, Y., et al., *Nanocomposites by melt intercalation based on polycaprolactone and organoclay.* Journal of Polymer Science Part B: Polymer Physics, 2003. **41**(7): p. 670-678.

37. Wu, D., et al., *Rheological properties and crystallization behavior of multi-walled carbon nanotube/poly(ε-caprolactone) composites.* Journal of Polymer Science Part B: Polymer Physics, 2007. **45**(23): p. 3137-3147.

38. Stark, M., et al., *From images to interactions: High-resolution phase imaging in tapping-mode atomic force microscopy.* Biophysical Journal, 2001. **80**(6): p. 3009-3018.

39. Garcia, R., et al., *Identification of nanoscale dissipation processes by dynamic atomic force microscopy.* Physical Review Letters, 2006. **97**(1).

40. Garcia, R., R. Magerle, and R. Perez, *Nanoscale compositional mapping with gentle forces.* Nature Materials, 2007. **6**(6): p. 405-411.

41. Czajkowsky, D.M., et al., *Direct visualization of surface charge in aqueous solution.* Ultramicroscopy, 1998. **74**(1-2): p. 1-5.

42. Tamayo, J. and R. Garcia, *Effects of elastic and inelastic interactions on phase contrast images in tapping-mode scanning force microscopy.* Applied Physics Letters, 1997. **71**(16): p. 2394-2396.

43. Cleveland, J.P., et al., *Energy dissipation in tapping-mode atomic force microscopy.* Applied Physics Letters, 1998. **72**(20): p. 2613-2615.

Chapter 5. Cytotoxicity of cellulose nanocrystals and biocompatibility of 3D-printed, surface-oxidized CNC/poly(ε-caprolactone) nanocomposite scaffolds for bone implants

5.1. Abstract

The biocompatibility of both sulfuric acid hydrolyzed-cellulose nanocrystals (SH-CNCs)/surface oxidized-CNCs (SO-CNCs) and 3D printed SO-CNC/poly(ε-caprolactone) (PCL) nanocomposite scaffolds was evaluated *in vitro* using MC3T3 preosteoblasts. Cytotoxicity studies confirmed that both SO-CNCs and SH-CNCs are non-toxic at all concentrations (0.25, 0.5, 1.0, and 3.0 mg/mL) tested. SO-CNCs exhibited better colloidal stability in cell culture media presumably because of their significantly higher surface charge density compared to SH-CNCs. In addition, 3D porous scaffold fabrication processes including solvent casting, melt compounding extrusion, and 3D printing were assessed by measuring the proliferation and differentiation of MC3T3 propsteoblasts. Although initial cell attachment followed by proliferation were delayed by the hydrophobicity of PCL, there was no observable harmful effect of the 3D porous scaffold fabrication processes.

5.2. Introduction

Autologous bone has long been considered the most compatible materila for repairing bone defects because it provides key elements, including osteogenic progenitor cells, osteoinductive growth factors and osteoconductive matrices, for bone regeneration [1]. Nevertheless, it has several limitations of traditional autographs [2], including donor site morbidity, unpredictable resorption, molding challenges, supply limitations and additional operations. As a promising tissue engineering approach, three-dimensional (3D) porous scaffolds could play an essential role as templates for mimicking the properties of natural bone tissue by providing a specific environment and architecture for tissue regeneration [1, 3]. A variety of materials and techniques for the fabrication of 3D porous scaffolds have previously been reported. Even though many materials and fabrication methods show promise, the mechanical instabilities of these materials preclude them from being viable options in bone scaffold applications, especially for defects of critical size or larger. By definition, a critical-sized bone defect is the smallest tissue defect that will not completely heal over the lifespan of an animal and will not heal without intervention [4-6]. Thus, the mechanical stability of the 3D porous scaffolds, which could be largely ascribed to both the configuration and fabrication method, is a crucial factor in the repair of critical-sized defects that require long-term performance of the scaffolds during tissue regeneration. Therefore, the design of scaffolds is of utmost importance because it is closely related to the performance of the scaffolds and should be carefully considered to obtain adequate mechanical and structural properties found in natural bone in order to minimize scaffold failures [7-9].

A variety of methods can be used to fabricate porous scaffolds, such as particle/salt leaching [10, 11], freeze-drying [12], thermally induced phase separation [13], and electrospinning [14]. Although there are several advantages in certain applications, those approaches cannot provide well-defined 3D porous configurations with fully controlled pore size, shape and interconnectivity of pores that could significantly influence the mechanical stability of the scaffold. On the other hand, rapid prototyping (RP) techniques, also known as solid free-form fabrication (SFF), have shown enormous potential in the field of biomedical engineering because they permit a customizable configuration through precisely controlled, computer-aided systems [1]. Recently among the SFF techniques, 3D printing has drawn considerable attention and paved the way to customizable implants for a wide range of tissue engineering applications due to the ability to directly create complex structure of 3D porous scaffolds without special molds and toxic solvents [1, 15, 16]. In particular, PCL is a potential candidate for bone scaffolds fabricated by 3D printing because of its good processibility and slower bioresorption rate compared to other polymers [17-20]. PCL is a hydrophobic and semi-crystalline linear polymer which belongs to the family of aliphatic polyesters and has long been used for biomedical applications, such as drug delivery systems and medical devices [21, 22]. However, there are critical challenges arising from the insufficient mechanical properties and low bioactivity of PCL in load-bearing bone tissue engineering applications.

Our previous studies have demonstrated the mechanical reinforcement of PCL nanocomposites by incorporation of SO-CNCs. In addition, the negatively charged

carboxyl groups on the SO-CNCs provided a strong capacity to bind calcium ions (i.e., calcium chelating properties) in simulated body fluid (1x) *in vitro* thereby indicating a potential to aid biomineralization *in vivo*. CNCs are elongated rod-like nanoparticles that are derived from cellulose-containing natural resources (e.g., wood or plant fibers, tunicate, algae, and bacterial cellulose) [23]. Due to their unique characteristics, such as outstanding mechanical properties, reactive surface properties, excellent biodegradability and biocompatibility, low ecotoxicological risk and comparatively low cost, CNCs have gained attention in various research fields over the past decades [24-27]. The overall goal of this research was to investigate the potential use of SO-CNCs as multi-functional additives that enhance the mechanical properties and increase the biomineralization rate of PCL for bone tissue engineering applications. In the present study, one of the main focuses was to examine the biocompatibility of CNCs and 3D printed SO-CNC/PCL nanocomposite scaffolds. We hypothesiz that CNCs derived from renewable natural resources are non-toxic, and that porous SO-CNC/PCL nanocomposite scaffolds constructed by fabrication processes including solvent casting, melt compounding extrusion and 3D printing are biocompatible for bone tissue engineering applications.

5.3. Experimental

5.3.1. Materials

Bleached softwood sulfite dissolving-grade pulp (Temalfa 93A) was kindly provided by Tembec Inc. (Témiscaming, QC, CA). Sulfuric acid (H_2SO_4, 96.2 wt %), acetonitrile (CH_3CN, HPLC Grade), dichloromethane (CH_2Cl_2), and sodium hydroxide (NaOH, 0.5M) were purchased from Fisher Scientific. 2,2,6,6,-Tetramethyl-1-piperidinyloxy

(TEMPO, $C_9H_{18}NO$, free radical, 98%), sodium hypochlorite solution (NaOCl, reagent grade, available chlorine 10-15%), methanol (CH_3OH, anhydrous, 99.8%) polycaprolactone (PCL, $(C_6H_{10}O_2)_n$, M_n: 70,000-90,000) were purchased from Sigma-Aldrich. Sodium bromide (NaBr, 99+%, extra pure, anhydrous) was purchased from Acros organics.

5.3.2. Methods

5.3.2.1. SO-CNCs preparation

First, CNCs were prepared by acid hydrolysis. Milled (60-mesh, Thomas Wiley® Mini-Mill, Thomas Scientific) pulp was hydrolyzed by adding 64 wt % sulfuric acid (500 mL, acid-to-pulp ratio of 10 mL/g) at 45.5 ºC under stirring. After 60 min, the hydrolysis was stopped by dilution of the reaction mixture with deionized (DI) water (2500 mL, ~4 ºC, 18.2 MΩ·cm, Millipore Direct-Q5 Ultrapure Water System) and the acid was removed by centrifugation (4500 rpm for 20 min at 4 ºC, IEC CENTRA GP8R Refrigerated Centrifuge, Thermo Electron Corporation) followed by discarding of the supernatant. The sediment was redispersed in DI water and centrifuged. This step was repeated three times. Then, the collected sediment was transferred to dialysis tubing (Spectra/Por 4, molecular weight cut off of 12-14 kDa) and dialyzed against DI water (refreshed daily) for one week to remove remaining the residual acid. After the dialysis, the sulfuric acid hydrolyzed-CNC (SH-CNC) suspension was sonicated (BRANSONIC® 3510) for 30 min and filtered through 0.45 µm syringe filter. The concentration of the filtered SH-CNC suspension was adjusted to 1.0 wt % with a rotary evaporator (Büchi Roravapor R-200)

using a water bath at 40 ºC and the stock suspensions were stored in a refrigerator until used.

SO-CNCs were prepared by surface oxidation of SH-CNCs. Surface modification of SH-CNCs was performed by TEMPO-mediated oxidation methods according to references [28, 29] with minor modifications. Briefly, the (TEMPO)-mediated oxidation was conducted by thoroughly mixing the aqueous SH-CNC suspension (1.0 wt %, 500 g), TEMPO (0.5 g) and NaBr (5 g) in a 1,000 mL flask with a magnetic stir bar at room temperature. The reaction was started by adding sodium hypochlorite solution (NaClO, reagent grade, available chlorine 10-15 %, Sigma-Aldrich) into the mixture. In order to maintain the pH between 10.2-10.5 during the oxidation, 50 mL of NaClO was added dropwise to the flask. The reaction was continued for three hours by adding sodium hydroxide (0.5 M) to maintain the pH. Afterwards, methanol (5 mL) was added to quench the reaction and the mixture was transferred to the dialysis tubing, then dialyzed against DI water (refreshed daily) for two weeks. Finally, the aqueous SO-CNC suspension was obtained followed by sonication for 30 min and filtered through 0.45 µm syringe filter. A concentration of SO-CNC suspensions was adjusted to 3 wt % and stored in a refrigerator until used.

5.3.2.2. SO-CNCs characterization

5.3.2.2.1. Atomic Force Microscopy (AFM)

The size of both SH-CNCs and SO-CNCs were measured by AFM. The AFM samples of SH-CNCs and SO-CNCs were prepared from 0.002 wt % aqueous suspensions. A mica

disc (diameter: 0.5 inch, Ted Pella) was mounted using epoxy adhesive resin onto a standard microscope slide. CNC suspensions (15 µL) were sonicated for 10 min and spin coated (4,000 rpm for 1 min, Laurell model WS-400B-6NPP/LITE) onto a freshly cleaved mica disc (diameter: 0.5 inch, Ted Pella). The spin coated CNCs samples were placed in a vacuum oven at 60 °C overnight. AFM analysis was performed under ambient conditions in tapping (AC) mode with an Asylum Research MFP3D-Bio atomic force microscope using standard silicon probes (Olympus OMCL-AC160TS, resonant frequency: ~300 kHz, spring constant: ~42 N/m, nominal tip radius: <10 nm) with a scan speed of 512 points/scan. The obtained AFM images were analyzed using IGOR pro software.

5.3.2.2.2. Dynamic light scattering (DLS) and zeta (ζ)-potential

Hydrodynamic diameters (or radii) of the CNCs in DI water and cell culture media are measured by DLS. The CNCs were prepared in DI water with a concentration of 0.1 wt % and the measurements were performed before and after ultraviolet (UV) light treatment. UV treatment and filtration were used as sterilization method of the CNCs for cytotoxicity test. Thus, the UV treated CNCs were filtered through a 0.22 µm syringe filter, and then different concentrations (0.25, 0.5, 1.0 and 3.0 mg/mL) of the CNCs in cell culture media were prepared. Also, the ζ-potential of the CNCs in DI water (1.0 wt %) was measured before and after UV treatment. The suspensions were sonicated for 10 min and transferred to Malvern Instruments DTS0012 disposable polystyrene cuvettes (for DLS) and to DTS1060 folded capillary cells (for ζ-potential). The sonication was not applied for the cell culture media samples. All measurements were carried out in

triplicate at 37 °C with a Malvern Instruments Zetasizer Nano ZS particle analyzer equipped with a He-Le laser (633 nm, 4.0 mW) and a photodiode detector located at 173°.

5.3.2.3. Fabrication of SO-CNC/PCL nanocomposites and 3D porous scaffolds

The SO-CNC/PCL nanocomposites were fabricated through a four-step processing including (i) solvent exchange of aqueous SO-CNC suspension, (ii) physical mixing, (iii) solvent casting and (iv) melt compounding extrusion. The solvent exchange process was performed by addition of CH_3CN to the aqueous SO-CNC suspension followed by centrifugation (SORVALL LEGEND X1R Centrifuge, Thermo Scientific) for 20 min at 5,000 rpm. Then, fresh CH_3CN was added to the collected sediment and homogenized (Power Gen 500, Sawtooth 10 x 95 mm, Fisher Scientific) for 5 min and sonicated for 30 min. This process was repeated three times. PCL was dissolved in CH_2Cl_2 at a ratio of 1:10 (w/v). The solvent exchanged SO-CNC suspension was stirred under sonication at 40 °C and the PCL solution was slowly added to the suspension and stirred for 30 min before solvent casting. The solvent cast films were cut into small pellets, then thoroughly rinsed with DI water and dried in a vacuum oven at 40 °C for 24 h. Finally, the pellets were extruded into a 3 mm (diameter) filament with a twin screw extruder (HAAKE MiniLab II, ThermoFisher Scientific) at 80 °C. The SO-CNCs/PCL nanocomposites were prepared with different SO-CNC contents (wt %) and denoted as PCL 0 (0 wt %), PCL 1 (1 wt %) and PCL 3 (3 wt %).

The 3D porous SO-CNC/PCL nanocomposite scaffolds were fabricated with a Thing-O-Matic 3D printer (MakerBot® Industries, LLC). The 3D printer is controlled via G-code, a computer numerical control programming language in stl file format. The 3D design file is translated to G-code with ReplicatorG, an open source 3D printing program. In this process, the design is converted into a sequence of slices used for the layer by layer printing of the 3D object. In addition, the generated G-code contains details about the process parameters, such as stage (X and Y directions) and nozzle movement (Z direction) and speed, nozzle temperature, and feed rate of the filament, controlled by the motor speed (e.g., nozzle size: 0.3 mm, nozzle temperature: 185 °C, extruder motor speed: 1.0 rpm, feed rate: 1800 mm/min) . The SO-CNC/PCL nanocomposite filaments (PCL 0, PCL 1, PCL 3) were used to fabricate the films and scaffolds.

5.3.2.4. Cell Culture

Each of the cell investigations in this study used Alpha Minimum Essential Medium (α-MEM, Life Technologies) with 10 % Fetal Bovine Serum (FBS, Life Technologies) and 1 % Penicillin-Streptomycin (Life Technologies). Each study also used 10,000 Mouse preosteoblast (MC3T3, ATCC) cells. The same spectrophotometer (BioTek, Multi-Mode Plate Reader, Synergy Mx, USA) was used to measure absorbance. A sample size of three was used for each variable and factor in these studies.

5.3.2.5. Cytotoxicity of CNCs

Both the SH-CNC and SO-CNC suspensions were sterilized using 0.22 μm syringe filters and the concentrations were measured. Targeted concentrations of CNCs in DI water were 0, 0.25, 0.5, 1.0, and 3.0 mg/mL. Ultraviolet light (UV) was applied to the filtered CNCs suspensions for sterilization. Different concentrations of CNC in DI water (150 μL) were combined with 10,000 cells in 850 μL of α-MEM for cytotoxicity testing. After 24 h, 20 μL of Trypan blue assay (0.4%, Life Technologies) was used to stain the cells for cytotoxicity. Using an optical microscope (Fisher Scientific) both live cells (clear) and dead cells (blue) were counted and averaged with a hemacytometer. A control group contains only DI water (150 μL) with 10,000 cells in 850 μL of α-MEM was used to compare the cytotoxicity of the CNC's. A sample size of three was used for each suspension concentration (0, 0.25, 0.5, 1.0, and 3.0 mg/mL) and type (SO-CNC and SH-CNC).

5.3.2.6. Cell proliferation on 3D printed SO-CNC/PCL nanocomposite films

Films (10 mm in diameter) were immersed in 70 % ethanol and exposed to UV (Thermo Scientific, 1300 Series A2, Remel Ultraviolet Light, 365 nm wavelength) for 24 h for sterilization. Films were then immersed in α-MEM with 10 % Fetal Bovine Serum (FBS) and 1 % Penicillin-Streptomycin for 12 h. Once soaked in α-MEM, films were placed in 48-well plates. Each film was seeded with 10,000 mouse preosteoblast cells (MC3T3) and 100 μL of α-MEM. The well plate was then incubated for 1 h at 37 °C under 5 %

CO_2 to allow for attachment. Once attachment occurred, 600 μL of α-MEM was added to each well. Cells were grown for 1, 4 and 7 days to determine proliferation of MC3T3's. A sample size of three was used for each time point (1, 4, and 7 days) and film SO-CNC concentration (0, 0.25, 0.5, 1.0, and 3.0 mg/mL within PCL film)

5.3.2.7. MTS Assay

CellTiter 96® Aqueous Non-Radioactive Cell Proliferation Assay (MTS, Promega, USA) was used to determine cell proliferation. Films were removed from wells and placed in new 48-well plates. Medium was added to each well (150μL) and combined with 50 μL of MTS assay then incubated for 4 h at 37 °C under 5 % CO_2 to allow for bioreduction of assay by cells. The solution (200 μL) was then transferred into a 96-well plate. The plate was then read using a spectrophotometer at 490 nm. A calibration curve was created using a set of standard cell concentrations (10^6, 10^5, 10^4, 10^3, 10^2). Using the calibration curve, the number of viable cells from each scaffold was determined.

5.3.2.8. Differentiation of 3D printed SO-CNC/PCL nanocomposite scaffolds

3D printed SO-CNC/PCL nanocomposite scaffolds were trimmed into a cylindrical shape (diameter: 6 mm, thickness: 3 mm). Scaffold preparation for differentiation studies followed the same procedure as with the SO-CNC/PCL films (Section 2.8). Cells were differentiated on the scaffolds for 7, 14, 21 and 28 days. After day four for each time point, medium was changed to differentiation medium (α-MEM with the addition of

0.1295 mM L-ascorbic acid-2-phosphate and 2 mM β-glycerophosphate). A sample size of three was used for each time point (7, 14, 21 and 28 days) and scaffold SO-CNC concentration (0, 0.25, 0.5, 1.0, and 3.0 mg/mL within PCL scaffolds).

5.3.2.8.1. MTS assay

MTS assay was followed using the same procedure as the films. (Section 5.2.2.7.)

5.3.2.8.2. Alkaline phosphatase assay

Alkaline Phosphatase, Diethanolamine Detection Kit (Sigma-Aldrich) was used to detect the amount of alkaline phosphate activity produced by the cells. The alkaline phosphatase assay was run on the medium in each well once the scaffolds had been removed for the MTS assay. The procedure provided by Sigma-Aldrich was followed to create enzyme solutions. Once the solutions were created, each solution's absorbance was read every min for 5 min in the spectrophotometer at 405 nm to determine increases in absorbance. Absorbance measurements were the used to calculate the amount of enzyme activity (units/mg) in each sample.

5.3.2.8.3. Osteocalcin assay

An osteocalcin rat ELISA kit (NeoBiolab) was used to detect mouse osteocalcin produced by MC3T3 cells during cell differentiation. NeoBiolab provided the procedure, a 96-well plate was used to measure the absorbance of each sample at 450 nm in a

spectrophotometer. Absorbance measurements were then graphed and used to calculate osteocalcin production.

5.3.2.8.4. Von Kossa Staining

Von Kossa staining was used to detect osteoid or supporting tissue/structures (red color) and mineralized bone or calcium deposits (black color) on the surface of scaffolds based on the procedure described in Von Kossa method for calcium kit (Polysciences, Inc.). After staining, optimal cutting temperature compound (Tissue-Tek® O.C.T.™ compound) was used to embed scaffolds prior to frozen (-20°C) sectioning (Microm HM550, Thermo Scientific, Cryostat Microtom). All of the microtomed scaffold samples (~ 50 μm) were placed on a glass slide and stored in a freezer. Prior to analysis, the samples were thoroughly rinsed in PBS and the edges of the sample were visualized using Optical light microscopy.

5.3.2.9. Statistical analysis

Statistical analysis was performed by one-way analysis of variance (ANOVA) in conjunction with Tukey's comparison test using OriginPro® 9.1 Graphing and Analysis software. Differences among groups were considered to be statistically significant at $p < 0.05$. Data are expressed as means ± standard deviations and error bars represent the standard deviation of the mean.

5.4. Results and discussion

The size of CNCs before (SH-CNC) and after surface modification (SO-CNC) were measured by AFM. AFM height images are as shown in Figure 5.1. Both length (121.5 ± 23.8 nm) and height (3.86 ± 1.1 nm) of SH-CNCs were decreased to 89.3 ± 22.7 nm and 2.23 ± 0.6 nm, respectively, after the oxidation process, introducing carboxyl groups on the surface of CNCs. The elongated rod-like morphology of CNCs were maintained but a length to height (aspect) ratio was increased from 31.5 (SH-CNCs) to 40.0 (SO-CNCs).

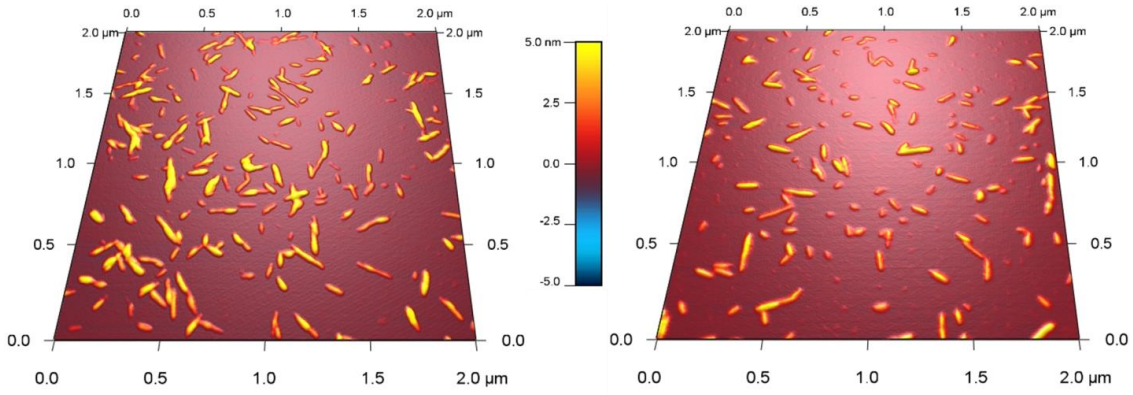

Figure 5.1. 3D AFM height images of SH-CNCs (left) and SO-CNCs (right).

Since the AFM image of the CNCs is acquired under dry condition, it is helpful to analyze the characteristics of nanoparticles in solution in order to provide the basis for understanding their biological effects and properly evaluate and/or interpret biological test results [30]. Thus, we attempted to identify sphere-equivalent hydrodynamic diameter and charge characterization of the CNCs in aqueous or physiologically relevant solutions using DLS and ζ-potential at 37 °C. The SH-CNC and SO-CNC exhibited similar size with monodispersed particle pattern in DI water before and after UV

treatment. However, both of the CNCs tended to have larger z-average value which is an indication of flocculation (or aggolomeration) in cell culture media (Figure 5.2). The z-average of SO-CNCs ranged from about 100 nm to 160 nm depending on the concentrations but the monodispersed pattern was maintained. On the other hand, the size of flocculated (or agglomerated) SH-CNCs was larger (about 1 to 2 µm) with very high PdI readings (PdI ≈ 1) in cell culture media (Figure 5.2) indicating significant particle aggregation.

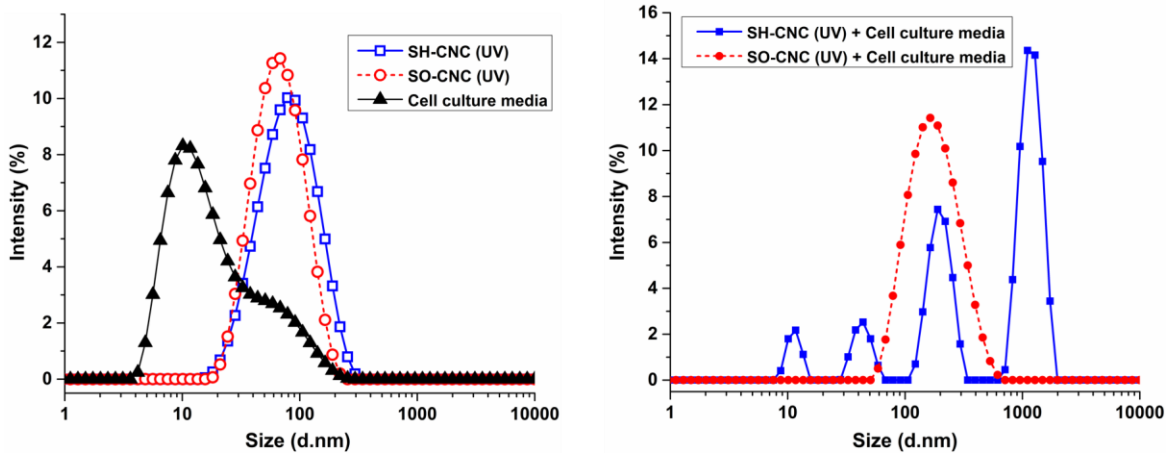

Figure 5.2. Dynamic light scattering of CNCs in DI water after the UV treatment (left), cell culture media only (left) and mixtures of CNCs and cell culture media (right) at 37 °C. The concentration of SH-CNC (pH=4.0) and SO-CNC (pH=6.3) in DI water and cell culture media was adjusted to 1 mg/mL.

A multimodal distribution pattern of the SH-CNCs and cell culture media mixture could be possibly due to the phase separation where the two phases were induced from the cell culture media (peaks < 100 nm) and the flocculations of SH-CNCs (peaks > 100 nm).

The DLS results for the particle size (z-average) and distributions (polydispersity index, PdI) in the solutions are presented in Table 5.1.

Table 5.1. Dynamic light scattering data for CNCs in aqueous and cell culture media.

		DI water	DI water (UV)	DI water (UV) + Cell culture media			
	Concentration	1.0 mg/mL	1.0 mg/mL	0.25 mg/mL	0.5 mg/mL	1.0 mg/mL	3.0 mg/mL
SH-CNC	Z-average (d.nm)	64.2 ±0.2	68.5 ±3.1	1221.0 ±17.1	1669.3 ±37.2	1214.7 ±63.5	2018.0 ±1851.4
	PdI	0.19 ±0.01	0.23 ±0.00	0.97 ±0.05	1.0 ±0.00	0.98 ±0.02	0.82 ±0.31
SO-CNC	Z-average (d.nm)	52.0 ±1.60	55.0 ±2.02	157.7 ±6.7	143.9 ±9.0	143.4 ±5.4	99.7 ±6.2
	PdI	0.19 ±0.01	0.20 ±0.00	0.32 ±0.00	0.34 ±0.06	0.28 ±0.01	0.24 ±0.00

**** Nanoparticles in DI water before and after UV treatment were sonicated before measurement but the samples with cell culture media were not sonicated after mixing. The measurements were performed at 37 °C.***

To better understand the increased z-average size and the multimodal dispersion pattern of CNCs in cell culture media, their surface charge properties such as ζ-potential and electrophoretic mobility were measured in DI water and summarized in Table 5.2. Both of the CNC types were stable in DI water with negative ζ-potentials (below -40) due to a negative surface charge of CNCs, and there was no significant difference before and after UV treatment.

Table 5.2. Summary of Zeta (ζ)-potential, electrophoretic mobility and conductivity of aqueous CNCs suspensions before and after UV treatment.

	SH-CNC	SH-CNC (UV)	SO-CNC	SO-CNC (UV)
ζ-potential (mV)	-41.13 ± 1.93	-42.67 ± 2.16	-41.40 ± 1.97	-40.50 ± 0.87
Electrophoretic mobility (μm·cm/V·s)	-3.95 ± 0.18	-4.10 ± 0.21	-3.97 ± 0.19	-3.88 ± 0.084

**** The concentration of aqueous SH-CNCs (pH: 2.7) and SO-CNCs (pH: 5.4) suspensions was adjusted to 10 mg/mL and the measurements were performed at 37 °C. The ζ-potential was calculated using Smoluchowski (F (ka)=1.5) approximation since the nanoparticles were dispersed in polar solvents.***

SO-CNC/PCL nanocomposite scaffolds with different concentrations of SO-CNC (0, 1, and 3 wt %) were fabricated using 3D printing technique. The SO-CNC/PCL nanocomposites were extruded through 0.3 mm nozzle and plotted as layer-by-layer deposition on a stage. Each layer was deposited with an angle of 90 ° from a previous layer. Diameter of single strand was 300 μm with a pore size of 500 μm as shown in Figure 5.3. Porosity of the scaffold was estimated based on the ratio of pore volume to its total volume, and was about 66 %. Additionally, a single layer of film (connected strands) was fabricated in order to evaluate whether the scaffold fabrication processes including solvent casting, melt compounding extrusion followed by 3D printing introduced any toxic components.

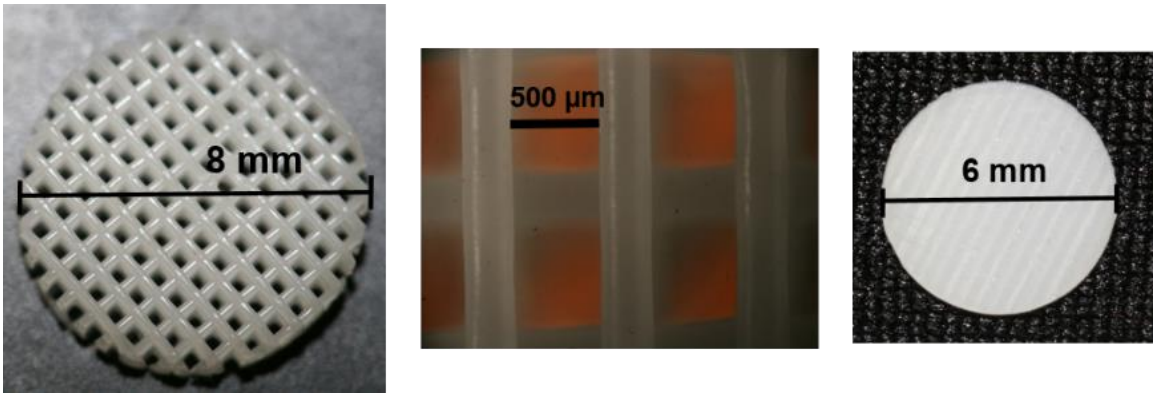

Figure 5.3. 3D printed SO-CNC/PCL nanocomposite porous scaffold (left), pore size (middle) and film (left).

Our previous studies showed that the surface carboxyl groups on the SO-CNCs have stronger calcium ion binding capacity in SBF 1x than that of sulfate groups (SH-CNCs), and thus the PCL nanocomposites were prepared by incorporating the SO-CNCs. However, the cytotoxicity of both SO-CNCs and SH-CNCs was investigated because the SH-CNCs are commonly used in research and are considered as potential candidates for biomedical applications [31-33]. SO-CNCs and SH-CNCs at all concentrations were found to be nontoxic to MC3T3s. After 24 h of exposure to all concentrations of CNCs, MC3T3 cells showed no significant difference ($p < 0.05$) from the DI water control (Figure 5.4). It was observed that lower cell viability was due to the low pH of DI water (pH 5.4). Therefore, to eliminate cytotoxic effects from those exposed to DI water, all the data was normalized to the DI water group as a control.

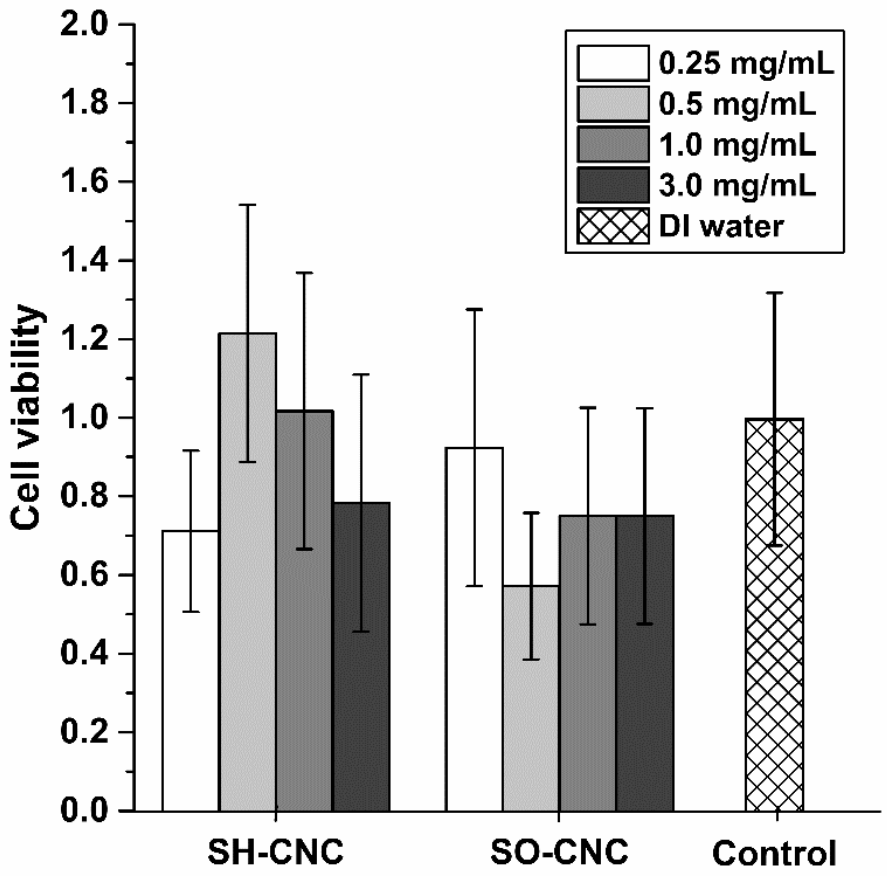

Figure 5.4. Cytotoxicity of MC3T3 cells after 24 h exposure to SO and SH CNC's. Each data set mean value was normalized to the DI water control, data showed no significant difference in means ($p<0.05$) compared to the control. Error bars represent standard deviation of the mean.

Cell proliferation of SO-CNC/PCL nanocomposite films (Figure 5.3) prepared using 3D printing techniques were evaluated to be sure that cells would grow on the SO-CNC/PCL material. Since the scaffolds were fabricated through several steps including solvent casting, melt compounding extrusion, and 3D printing, it is helpful to provide certain information for creation of preliminary cell data on the biocompatibility of these scaffolds.

An MTS assay was used to count the number of live cells on the films. Results indicated that the numbers of viable cells on the SO-CNC/PCL films at days 1 and 4 were significantly lower than the number on the control, which is a polystylene well plate (Figure 5.5).

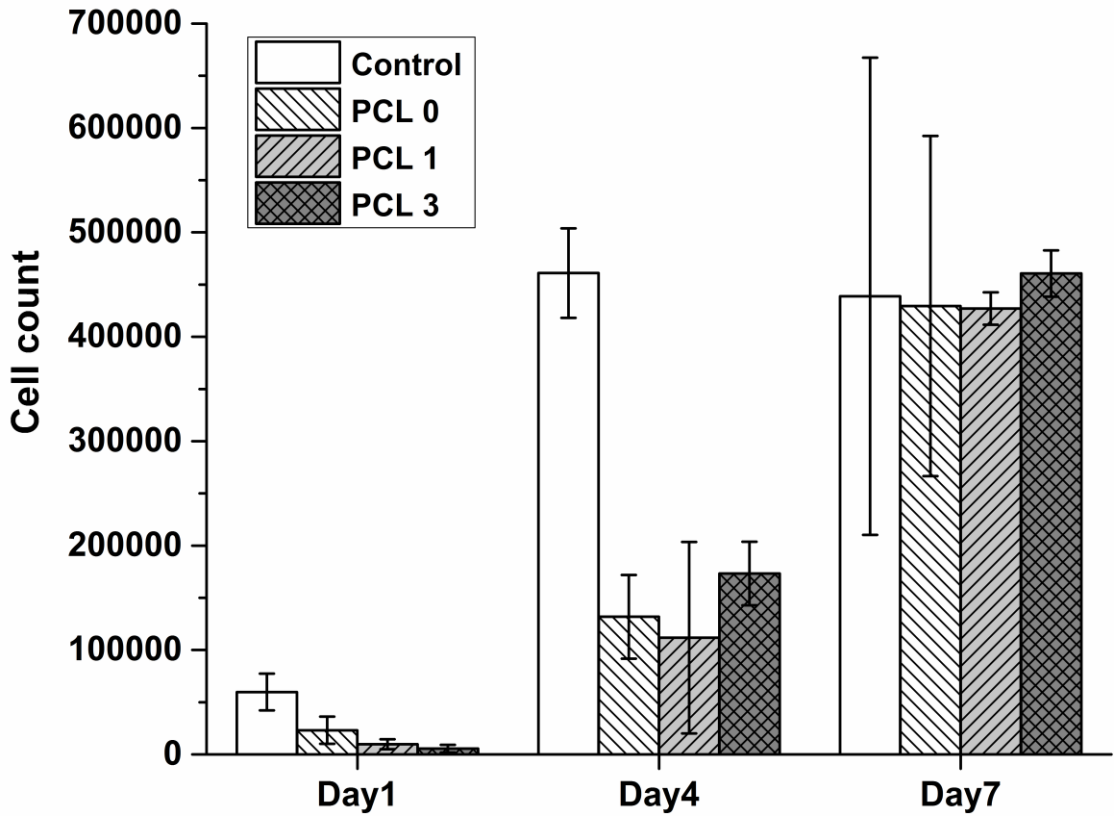

Figure 5.5. Cell viability on 3D printed SO-CNC/PCL nanocomposite films. Error bars represent standard deviation of the mean.

However, by day 7 there was no significant difference between PCL films (PCL 0, PCL 1, and PCL 3) and the control. Cell proliferation rapidly increased after day 4 and reached the same level as the control group at day 7. Therefore, it can be concluded that there are

no observable cytotoxic effect from the CNCs or material fabrication process and that once cells have been growing for at least 7 days, the cells grow at the same rate on films as on a polystyrene well plate.

Three different assays were used to investigate the differentiation of MC3T3 on SO-CNC scaffolds; MTS assay, alkaline phosphatase, and an osteocalcin ELISA Kit. The MTS assay kit was used to determine whether cells were still proliferating throughout the 7, 14, 21 and 28 day study and to count the number of cells throughout the study. Alkaline phosphatase is expressed as enzymatic activity when mouse preosteoblast cells differentiate into mouse osteoblast cells. Osteocalcin indicates that cells completed the differentiation process and began to produce bone mineralization.

MTS assay results found that cell proliferation continued throughout the 28 days (Figure 5.6). Significant differences were seen between the control groups and scaffold samples (Day 7, 14 and 28) due to the method used to count the cells. While control groups were allowed to grow on the complete surface area of the polystyrene wells, MTS results were only conducted on the scaffolds themselves. Cells significantly grow after day 7 for PCL1, PCL 3 and controls but showed significant differences on day 14, 21 or 28. PCL 0 showed a significant increase only between day 7 and day 21. These results confirmed that there is no negative effect of CNCs on cell proliferation.

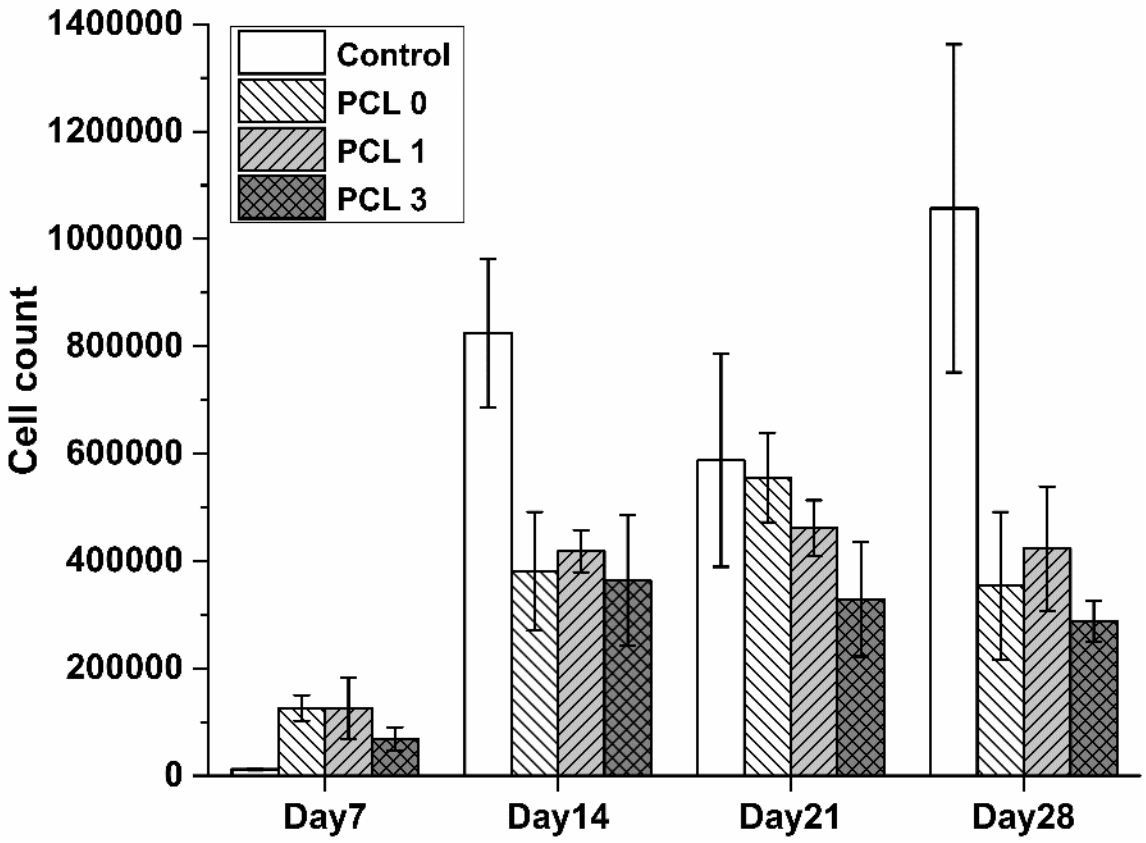

Figure 5.6. Cell viability on 3D printed SO-CNC/PCL nanocomposite scaffolds. Error bars represent standard deviation of the mean.

Alkaline phosphates measure the enzymatic activity as the cells differentiate into osteoblast cells. Alkaline phosphatase will general peak around day 7 for MC3T3 cells (Citation). However, no significant differences were seen in the alkaline phosphatase results (Figure 5.7). Alkaline phosphatase activity is seen throughout days 7, 14, 21, and 28, which may indicate that the peak enzymatic activity occurred before day 7. In agreement with these results, a similar study has reported that ALP activity was significantly increased and up-regulated in PCL scaffolds on day 7 (no significant difference after day 1) [34].

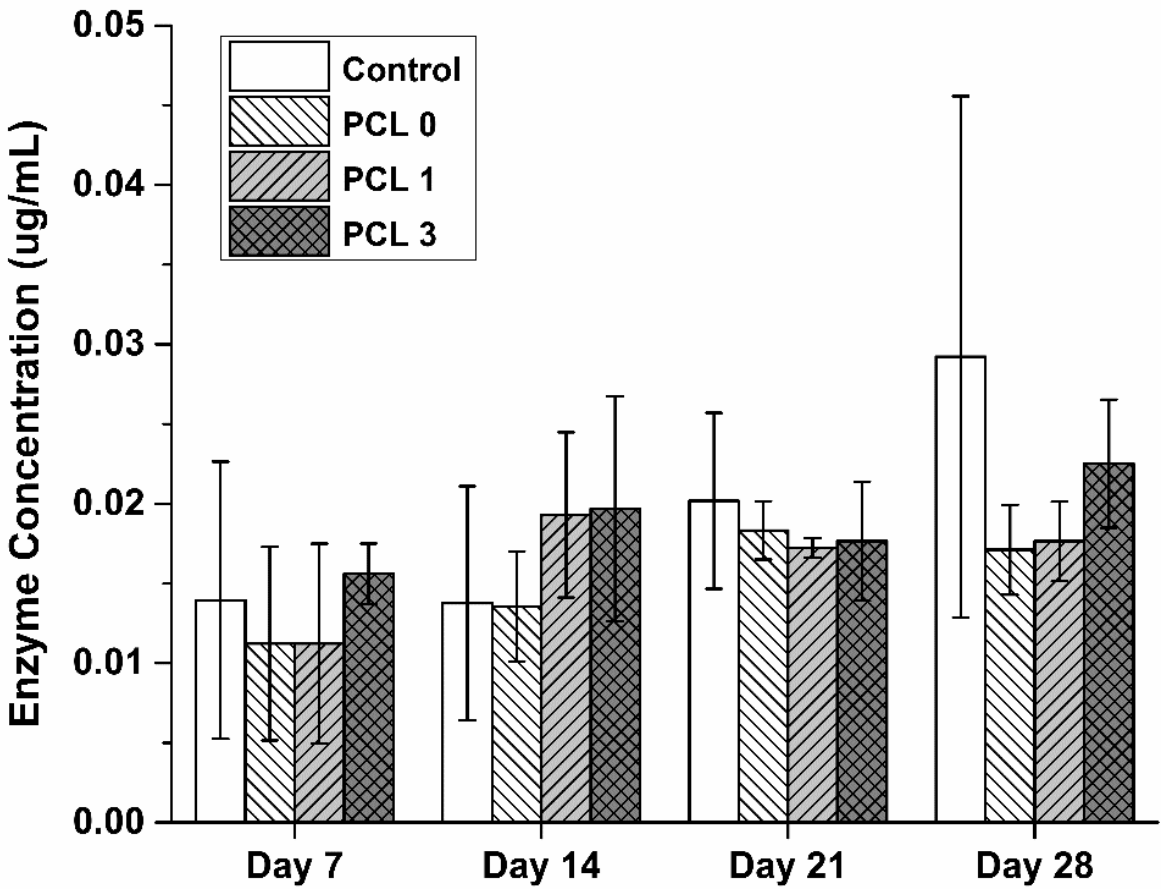

Figure 5.7. Alkaline phosphatase enzymatic activity on 3D printed SO-CNCs/PCL nanocomposite scaffolds.

The osteocalcin ELISA kit measures the concentration of protein produced by the osteoblast cells. There were significant decreases between day 7 and day 14 for the control, PCL 0 and PCL 1 (Figure 5.8). The protein concentration of PCL 0 is significantly high than both the control and PCL 3 on day 7, but day 14, 21, and 28 show no differences between the different samples. PCL 1 also showed a significant increase between day 14 and day 28, while PCL 3 showed no significant differences between any of the days. These results indicate that there may be a peak osteocalcin protein

concentration at day 7, which would confirm the prediction of an earlier alkaline phosphatase peak.

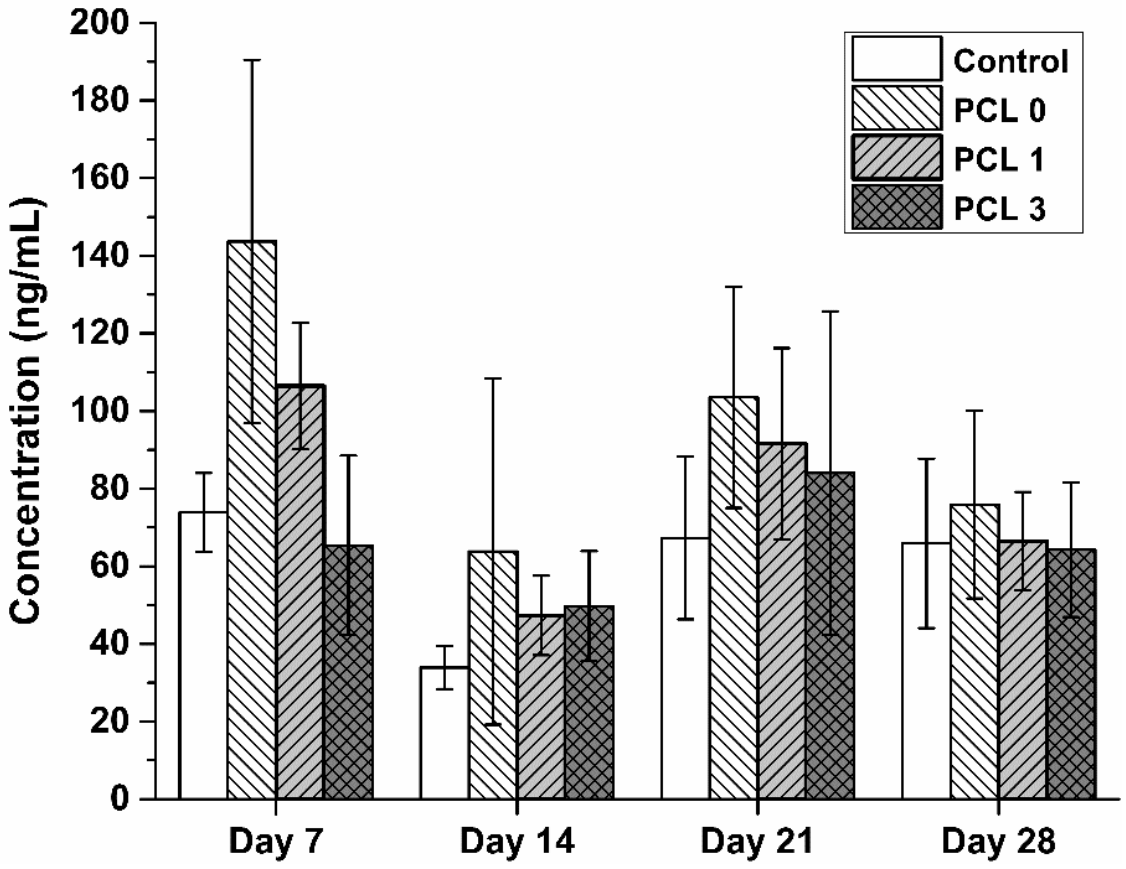

Figure 5.8. Osteocalcin assay on 3D printed SO-CNCs/PCL nanocomposite scaffolds.

The surface charge of nanoparticles is important not only because it plays a crucial role in determining the particle dispersion properties but also because it affects the adsorption of ions and biomolecules, which may influence the cell-particle interaction [30]. In general, particle ζ-potential of +/- 30 mV is often considered as an approximate threshold for

stability [35]. The surface charge of SH-CNCs is the result of partial esterification of the surface hydroxyl groups by sulfuric acid during the hydrolysis. In aqueous suspension, these sulfate groups are dissociated and carry a negative charge; this stabilizes the suspension through electrostatic repulsion among the particles. In addition, the primary hydroxyl groups which were not occupied by sulfate groups are selectively oxidized to carboxyl groups during the surface modification for SO-CNCs. Similarly, most of the carboxyl groups on the surface of SO-CNC should be dissociated and negatively charged in aqueous suspension (pH: 5.4~6.3) since pKa values of carboxylic acids are approximately 4.8. Therefore, both of the sulfate and carboxyl groups should be dissociated and negatively charged in the cell culture media (pH ≈ 7).

On the other hand, the surface charge density of both SH-CNCs (sulfate group) and SO-CNCs (carboxyl group) was estimated by the conductometric titration in a previous study. The calculated surface charge densities of SH-CNCs and SO-CNCs in DI water were 0.35 ± 0.02 mmol/g and 1.86 ± 0.07 mmol/g, respectively. In contrast with DI water, the electrostatic repulsion of the negatively charged CNCs could be weaker in cell culture media, due to charge screening. This could cause reduction in net charge (zeta potential) of the particle, thereby inducing flocculation (or agglomeration) in cell culture media [36]. Unlike the SH-CNCs, therefore, the SO-CNC could have enough negative charge to prevent flocculation (or agglomeration) and keep particles separated.

Cytotoxicity studies confirm that CNC's are non-toxic to MC3T3 cells. Cell proliferation confirms that cells proliferate at rates equivalent to those of the control groups after day

7. This could indicate that the cells had a difficult time initially attaching to the PCL scaffolds. MC3T3 are cultured on polystyrene material and take less than 24 h to adhere to that material (citation). However, PCLs surface characteristics are not favorable for cell adhesion and proliferation due to its intrinsic hydrophobicity and lack of bioactive functional groups [38, 39], resulting in poor cell attachment and proliferation [40]. To enhance the bioactivity properties of PCL, various surface modification techniques have been developed, including chemical treatments, laser surface modification, ion beam radiation, plasma modification, and protein coating [41-50]. Thus, the unfavorable surface properties of the SO-CNC/PCL nanocomposite scaffolds need to be further improved by providing better cell-adhesion properties. The PCL scaffolds caused a slower initial proliferation rate, but after day 7, the cell growth was not significantly different than control growth. This could be attributed to the fact that cell proliferation occurs much slower on the PCL films (PCL 0, PCL 1, and PCL 3) due to the hydrophobicity. The contact angles of the PCL 0, PCL 1 and PCL 3 films in DI water were 87.0°, 85.5° and 84.5°, respectively, from our previous study. Thus, the initial attachment efficiency of the cells might be inhibited by the surface hydrophobicity of the PCL films [51] resulting in slower cell proliferation at the beginning of the cell seeding.

Differentiation studies also confirm that proliferation occurs throughout the entire study but at significantly lower rates than the control groups. This may be due to the analysis techniques for the MTS assay. For the scaffolds, each scaffold is removed from the well and then analyzed. This way the only cells that were counted were the ones on the scaffolds themselves. This is different than the control groups because all of the cells in

empty polystyrene well were counted. It is possible that the cells were colonized only at the edge of the scaffold and no cells were present in the center of the scaffold [34]. This could account for increased cell counts seen in the control groups. If the PCL groups are compared to each other, cell counts for PCL 1 and PCL 3 significantly increase between day 7 and day 14. This could indicate that the CNC concentration helps the cells to attach to the PCL scaffolds but more data is need to confirm these results. The alkaline phosphatase assay (Figure 5.7) measures the concentration of enzyme activity in the media around the scaffolds. The results confirm the high proliferation rates that are seen in the MTS assay results. More cells result in higher enzyme concentration, as observed which in the alkaline phosphatase assay. However, there are very few differences observed between the days or sample variables. As stated previously this could be due to the up regulation of ALP. As previously described [34], the ALP activity peak is an indicator of the start of differentiation and may appear before day 7, which could be why the enzyme activity is relatively stable for days 7 through 28. The osteocalcin results show a peak in protein concentration at day 7, which supports the contention that the ALP peak is earlier than day 7. In order to confirm these results, scaffold were further stained with Von Kossa method for visualization of calcium deposit and mineralized matrix and scaffold sections were shown in Figure 5.9. A visual difference between the scaffolds and time points were seen due to osteoid or supporting tissue/structure formation (red) and mineralized bone or calcium deposits (black). The results indicated that the SO-CNCs do not impede the differentiation of MC3T3's cells and may in fact encourage cells to differentiate and the calcium deposits or mineralized bone matrix

formation on the surface of scaffolds (PCL 1 and PCL 3) were not precluded but accelerated.

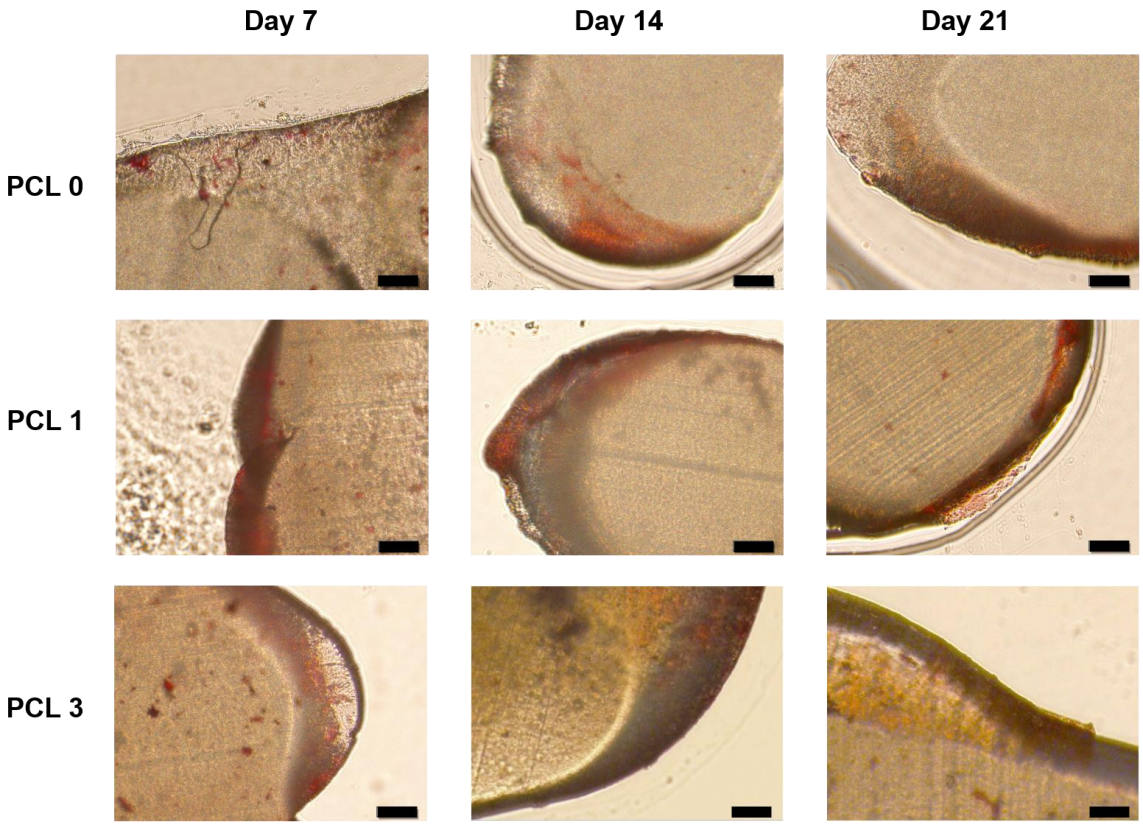

Figure 5.9. Von Kossa staining of PCL scaffolds (scale bar: 50 µm).

5.5. Summary

With respect to the objective of this study, our conclusions are:

- The SO-CNCs exhibited better stability of colloidal dispersion in cell culture media because of the significantly higher surface charge density than that of SH-CNCs;
- Cytotoxicity studies confirmed that both SO-CNCs and SH-CNCs are non-toxic to the MC3T3 cells;
- Delays in initial cell attachment followed by proliferation were influenced by the hydrophobicity of PCL;
- The porous scaffold fabrication processes (including the nanocomposite fabrications) through 3D printing did not cause any harmful effects in terms of scaffold biocompatibility.
- The SO-CNC (PCL 3) encouraged the MC3TC cell differentiation and accelerated calcium deposits and mineralized bone matrix formation on the surface of scaffold.

5.6. References

1. Schieker, M., et al., *Biomaterials as Scaffold for Bone Tissue Engineering.* European Journal of Trauma, 2006. **32**(2): p. 114-124.

2. Rogers, G.F. and A.K. Greene, *Autogenous bone graft: basic science and clinical implications.* J Craniofac Surg, 2012. **23**(1): p. 323-7.

3. Stevens, M.M., *Biomaterials for bone tissue engineering.* Materials Today, 2008. **11**(5): p. 18-25.

4. Schmitz, J.P. and Hollinger, J.O., *The Critical Size Defect as an Experimental Model for Craniomandibulofacial Nonunions.* Clinical Orthopaedics and Related Research, 1986. **205**: p. 299-308.

5. Takagi, K. and M.R. Urist, *The reaction of the dura to bone morphogenetic protein (BMP) in repair of skull defects.* Ann Surg, 1982. **196**(1): p. 100-9.

6. Spicer, P.P., et al., *Evaluation of bone regeneration using the rat critical size calvarial defect.* Nat Protoc, 2012. **7**(10): p. 1918-29.

7. Caplan, A.I., *Tissue engineering designs for the future: new logics, old molecules.* Tissue Eng, 2000. **6**(1): p. 1-8.

8. Sharma, B. and J.H. Elisseeff, *Engineering structurally organized cartilage and bone tissues.* Ann Biomed Eng, 2004. **32**(1): p. 148-59.

9. Meinel, L., et al., *Silk implants for the healing of critical size bone defects.* Bone, 2005. **37**(5): p. 688-98.

10. Cao, H. and N. Kuboyama, *A biodegradable porous composite scaffold of PGA/beta-TCP for bone tissue engineering.* Bone, 2010. **46**(2): p. 386-95.

11. Stoppato, M., et al., *Influence of scaffold pore size on collagen I development: A new in vitro evaluation perspective.* Journal of Bioactive and Compatible Polymers, 2013. **28**(1): p. 16-32.

12. Sultana, N. and M. Wang, *Fabrication of HA/PHBV composite scaffolds through the emulsion freezing/freeze-drying process and characterisation of the scaffolds.* Journal of Materials Science-Materials in Medicine, 2008. **19**(7): p. 2555-2561.

13. Hutmacher, D.W., *Scaffolds in tissue engineering bone and cartilage.* Biomaterials, 2000. **21**(24): p. 2529-43.

14. Hackett, J.M., et al., *Electrospun Biocomposite Polycaprolactone/Collagen Tubes as Scaffolds for Neural Stem Cell Differentiation.* Materials, 2010. **3**(6): p. 3714-3728.

15. Park, S., et al., *3D polycaprolactone scaffolds with controlled pore structure using a rapid prototyping system.* Journal of Materials Science-Materials in Medicine, 2009. **20**(1): p. 229-234.

16. Bose, S., S. Vahabzadeh, and A. Bandyopadhyay, *Bone tissue engineering using 3D printing.* Materials Today, 2013. **16**(12): p. 496-504.

17. Park, S.A., S.H. Lee, and W.D. Kim, *Fabrication of porous polycaprolactone/hydroxyapatite (PCL/HA) blend scaffolds using a 3D plotting system for bone tissue engineering.* Bioprocess and Biosystems Engineering, 2011. **34**(4): p. 505-513.

18. Sobral, J.M., et al., *Three-dimensional plotted scaffolds with controlled pore size gradients: Effect of scaffold geometry on mechanical performance and cell seeding efficiency.* Acta Biomater, 2011. **7**(3): p. 1009-18.

19. Hoque, M.E., et al., *Processing of Polycaprolactone and Polycaprolactone-Based Copolymers into 3D Scaffolds, and Their Cellular Responses.* Tissue Engineering Part A, 2009. **15**(10): p. 3013-3024.

20. Hutmacher, D.W., et al., *Mechanical properties and cell cultural response of polycaprolactone scaffolds designed and fabricated via fused deposition modeling.* Journal of Biomedical Materials Research, 2001. **55**(2): p. 203-216.

21. Pitt, C.G., et al., *Aliphatic polyesters II. The degradation of poly (DL-lactide), poly (epsilon-caprolactone), and their copolymers in vivo.* Biomaterials, 1981. **2**(4): p. 215-20.

22. Woodruff, M.A. and D.W. Hutmacher, *The return of a forgotten polymer-Polycaprolactone in the 21st century.* Progress in Polymer Science, 2010. **35**(10): p. 1217-1256.

23. Moon, R.J., et al., *Cellulose nanomaterials review: structure, properties and nanocomposites.* Chemical Society Reviews, 2011. **40**(7): p. 3941-3994.

24. Fleming, K., et al., *Cellulose crystallites: A new and robust liquid crystalline medium for the measurement of residual dipolar couplings.* Journal of the American Chemical Society, 2000. **122**(21): p. 5224-5225.

25. Lin, N., J. Huang, and A. Dufresne, *Preparation, properties and applications of polysaccharide nanocrystals in advanced functional nanomaterials: a review.* Nanoscale, 2012. **4**(11): p. 3274-3294.

26. Kovacs, T., et al., *An ecotoxicological characterization of nanocrystalline cellulose (NCC).* Nanotoxicology, 2010. **4**(3): p. 255-270.

27. Domingues, R.M.A., M.E. Gomes, and R.L. Reis, *The Potential of Cellulose Nanocrystals in Tissue Engineering Strategies.* Biomacromolecules, 2014. **15**(7):

p. 2327-2346.

28. Araki, J., M. Wada, and S. Kuga, *Steric stabilization of a cellulose microcrystal suspension by poly(ethylene glycol) grafting.* Langmuir, 2001. **17**(1): p. 21-27.

29. Habibi, Y., H. Chanzy, and M. Vignon, *TEMPO-mediated surface oxidation of cellulose whiskers.* Cellulose, 2006. **13**(6): p. 679-687.

30. Powers, K.W., et al., *Research strategies for safety evaluation of nanomaterials. Part VI. Characterization of nanoscale particles for toxicological evaluation.* Toxicol Sci, 2006. **90**(2): p. 296-303.

31. DONG, S., et al., *CYTOTOXICITY AND CELLULAR UPTAKE OF CELLULOSE NANOCRYSTALS.* Nano LIFE, 2012. **02**(03): p. 1241006.

32. Mahmoud, K.A., et al., *Effect of Surface Charge on the Cellular Uptake and Cytotoxicity of Fluorescent Labeled Cellulose Nanocrystals.* ACS Applied Materials & Interfaces, 2010. **2**(10): p. 2924-2932.

33. Empson, Y.M., et al., *High elastic modulus nanoparticles: a novel tool for subfailure connective tissue matrix damage.* Translational Research, 2014. **164**(3): p. 244-257.

34. Declercq, H.A., et al., *Synergistic effect of surface modification and scaffold design of bioplotted 3-D poly-epsilon-caprolactone scaffolds in osteogenic tissue engineering.* Acta Biomater, 2013. **9**(8): p. 7699-708.

35. *Marlvern Instruments Ltd. Zetasizer Nano Series User Manual*. 2005, Worcestershire, UK.

36. Hu, Y. and J. Dai, *Hydrophobic aggregation of alumina in surfactant solution.* Minerals Engineering, 2003. **16**(11): p. 1167-1172.

37. Park, S., et al., *3D polycaprolactone scaffolds with controlled pore structure using a rapid prototyping system.* J Mater Sci Mater Med, 2009. **20**(1): p. 229-34.

38. Chen, G., et al., *Silk fibroin modified porous poly(E-caprolactone) scaffold for human fibroblast culture in vitro.* Journal of Materials Science-Materials in Medicine, 2004. **15**(6): p. 671-677.

39. Yildirim, E.D., et al., *Effect of dielectric barrier discharge plasma on the attachment and proliferation of osteoblasts cultured over poly(epsilon-caprolactone) scaffolds (vol 4, pg 58, 2007).* Plasma Processes and Polymers, 2008. **5**(4): p. 397-397.

40. Woodruff, M.A. and D.W. Hutmacher, *The return of a forgotten polymer—Polycaprolactone in the 21st century.* Progress in Polymer Science, 2010. **35**(10): p. 1217-1256.

41. Seyednejad, H., et al., *Preparation and characterization of a three-dimensional printed scaffold based on a functionalized polyester for bone tissue engineering applications.* Acta Biomater, 2011. **7**(5): p. 1999-2006.

42. Cheng, Z. and S.-H. Teoh, *Surface modification of ultra thin poly (ε-caprolactone) films using acrylic acid and collagen.* Biomaterials, 2004. **25**(11): p. 1991-2001.

43. Lee, H. and G. Kim, *Three-dimensional plotted PCL/[small beta]-TCP scaffolds coated with a collagen layer: preparation, physical properties and in vitro evaluation for bone tissue regeneration.* Journal of Materials Chemistry, 2011. **21**(17): p. 6305-6312.

44. Oliveira, A.L., et al., *Nucleation and growth of biomimetic apatite layers on 3D plotted biodegradable polymeric scaffolds: Effect of static and dynamic coating conditions.* Acta Biomaterialia, 2009. **5**(5): p. 1626-1638.

45. Chim, H., et al., *A comparative analysis of scaffold material modifications for load-bearing applications in bone tissue engineering.* Int J Oral Maxillofac Surg, 2006. **35**(10): p. 928-34.

46. Tiaw, K.S., et al., *Laser surface modification of poly(epsilon-caprolactone) (PCL) membrane for tissue engineering applications.* Biomaterials, 2005. **26**(7): p. 763-9.

47. Pignataro, B., et al., *Improved cell adhesion to ion beam-irradiated polymer surfaces.* Biomaterials, 1997. **18**(22): p. 1461-70.

48. Yildirim, E.D., et al., *Accelerated differentiation of osteoblast cells on polycaprolactone scaffolds driven by a combined effect of protein coating and plasma modification.* Biofabrication, 2010. **2**(1): p. 014109.

49. Yildirim, E.D., et al., *Enhanced Cellular Functions on Polycaprolactone Tissue Scaffolds by O2 Plasma Surface Modification.* Plasma Processes and Polymers, 2011. **8**(3): p. 256-267.

50. Berneel, E., et al., *Double protein-coated poly-ε-caprolactone scaffolds: Successful 2D to 3D transfer.* Journal of Biomedical Materials Research Part A, 2012. **100A**(7): p. 1783-1791.

51. Ng, K.W., et al., *Evaluation of ultra-thin poly(epsilon-caprolactone) films for tissue-engineered skin.* Tissue Eng, 2001. **7**(4): p. 441-55.

Chapter 6. Conclusions

This research investigated the potential use of cellulose nanocrystals (CNCs) as multi-functional additives that can enhance the insufficient properties, such as poor mechanical properties and low bioactivity of bioresorbable polymer (PCL) for bone tissue engineering applications. Hence, this project brings forward a novel nanocomposite material for 3D printing of bone scaffolds, based on poly(ε-caprolactone) (PCL) and surface-oxidized-cellulose nanocrystals (SO-CNCs), that stimulates bone formation, provides adequate mechanical support during healing, and is gradually absorbed by the body. To this end, the effect of surface functional groups of CNCs on biomineralization was assessed using simulated body fluid. The mechanical reinforcing effects of SO-CNCs on the PCL matrices as well as the mechanical stability of the 3D porous scaffolds were studied. Lastly, the biocompatibility of CNCs and SO-CNC/PCL scaffolds were evaluated.

From the biomineralization study, the carboxyl groups on the surface of CNCs (SO-CNCs) are more effective than the sulfate groups (SH-CNCs) in terms of calcium ion binding capacity which could play an important role in the biomineralization process by the induction of mineral formation for bone tissue engineering applications. In addition, the SO-CNCs exhibits a prominence effect on the mechanical reinforcement of PCL. The 3D porous SO-CNC/PCL nanocomposite (SO-CNC content of up to 3 wt %) scaffolds with the well-controlled pore size/shape and fully interconnected pores are successfully fabricated by 3D printing. A small amount of SO-CNCs remarkably enhance the

compressive modulus and creep resistance of the PCL scaffolds even though the mechanical stability of the PCL 3 scaffold is influenced by both temperature and submersion condition based on the long-term prediction from the TTS master curve. Lastly, the biocompatibility study reveals that there are no observable cytotoxic effect from the CNCs or material fabrication processes. Therefore, the SO-CNCs are expected to play a critical role in the development of tissue engineered materials and are being considered as a feasible option for reinforcing nanofillers in bone tissue engineering applications.

Chapter 7. Future work

The results presented in this study have demonstrated the potential applications of cellulose nanocrystals (CNCs) as multi-functional additives for developing bone scaffold materials not only by providing a significantly strong calcium ion binding ability (bioactivity in terms of biomineralization) induced by the negatively charged carboxyl groups through the surface oxidation of CNCs but also by reinforcing the mechanical properties of 3D printed porous poly(ε-caprolactone) nanocomposites. However, there is clearly much work to be done in order to promote new bone tissue formation perhaps by incorporating with osteoinductive elements such as cells and bioactive agents, and it could be further developed with various approaches.

Ideally, for instance, the porous scaffolds can be filled with biodegradable hydrogels (e.g., collagen, alginate and chitosan) which could encapsulate cells and embed growth factors, thus providing osteoinductive properties shown in Figure 7.1. Thus, cell-material interactions that can provide adequate environment for bone regeneration *in vivo*, and eventually, the scaffolds can be comparable to those of current bone grafts (e.g., autograft).

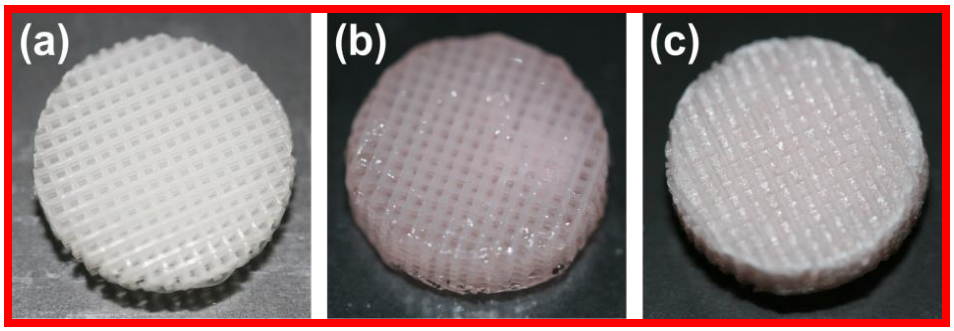

Figure 7.1. 3D printed PCL nanocomposite scaffold. (a) Porous scaffold. (b) Scaffold filled with alginate hydrogel. (c) Scaffold filled with alginate hydrogel after lyophilization.

Over the last few decades, bone tissue engineering have been developed and achieved significant improvement in various aspects in terms of osteoinduction, osteoconduction and osseointegration. In order to obtain more reliable outcome as feasible therapeutic options, cross-disciplinary research collaborations that can combine expertise from material and biological perspectives would lead to a better strategies for bone tissue engineering application. It is sincere hope that this study would contribute and potentially provide some useful insights for developing bone scaffold materials in the near future.

Appendix A. The effect of ion exchange resin treatment on both titration and ICP analysis

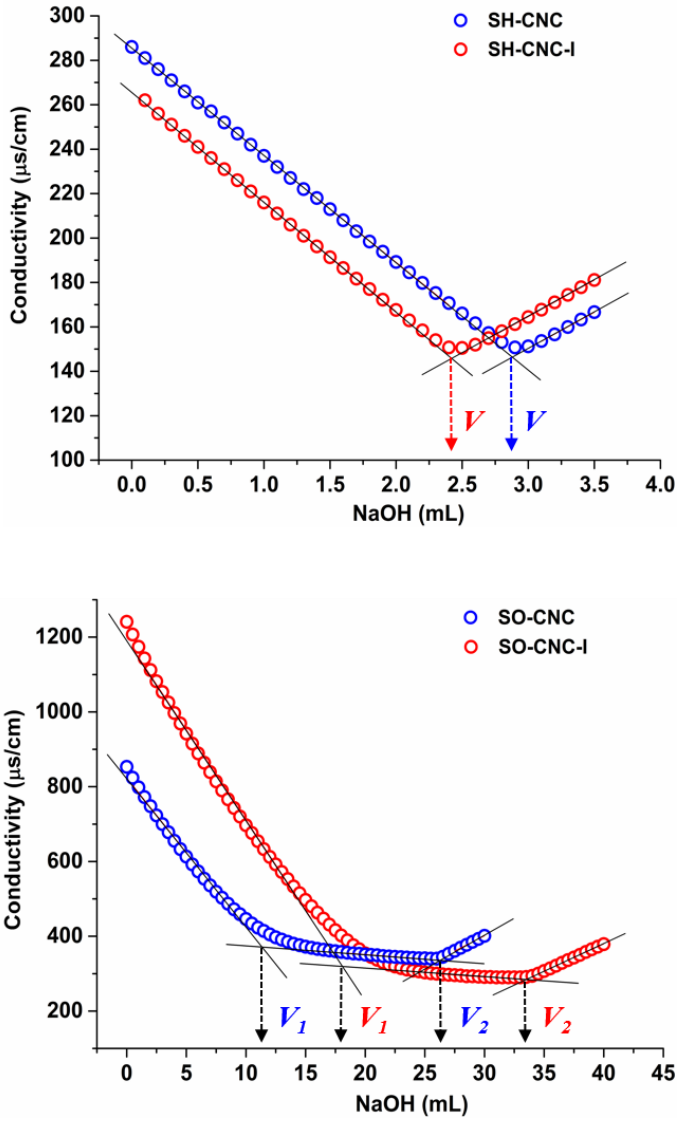

Figure A.1. Conductometric titrations of aqueous SH-CNC (top) and SO-CNC (bottom) suspension before (blue) and after ion exchange resin treatment for 12 h (red).

Table A.1. Summary of titration (surface charge density) and ICP analysis (sulfur and sodium) of CNCs before and after ion exchange resin treatment.

	Conductometric titration	ICP analysis	
	Surface charge density (mmol/g)	Analyte (mg/L)	
		S	Na
SH-CNC	0.316 ± 0.007	0.217 ± 0.04	0.020 ± 0.004
SH-CNC-I	0.271 ± 0.002	0.180 ± 0.004	0.052 ± 0.005
SO-CNC	1.840 ± 0.004	0.171 ± 0.004	0.881 ± 0.005
SO-CNC-I	1.997 ± 0.142	0.152 ± 0.002	0.065 ± 0.008

**** Surface charge density of SH-CNC/SH-CNC-I and SO-CNC/SO-CNC-I indicate sulfate group and carboxyl group, respectively.***

Appendix B. X-ray diffraction measurement of mineralized CNCs

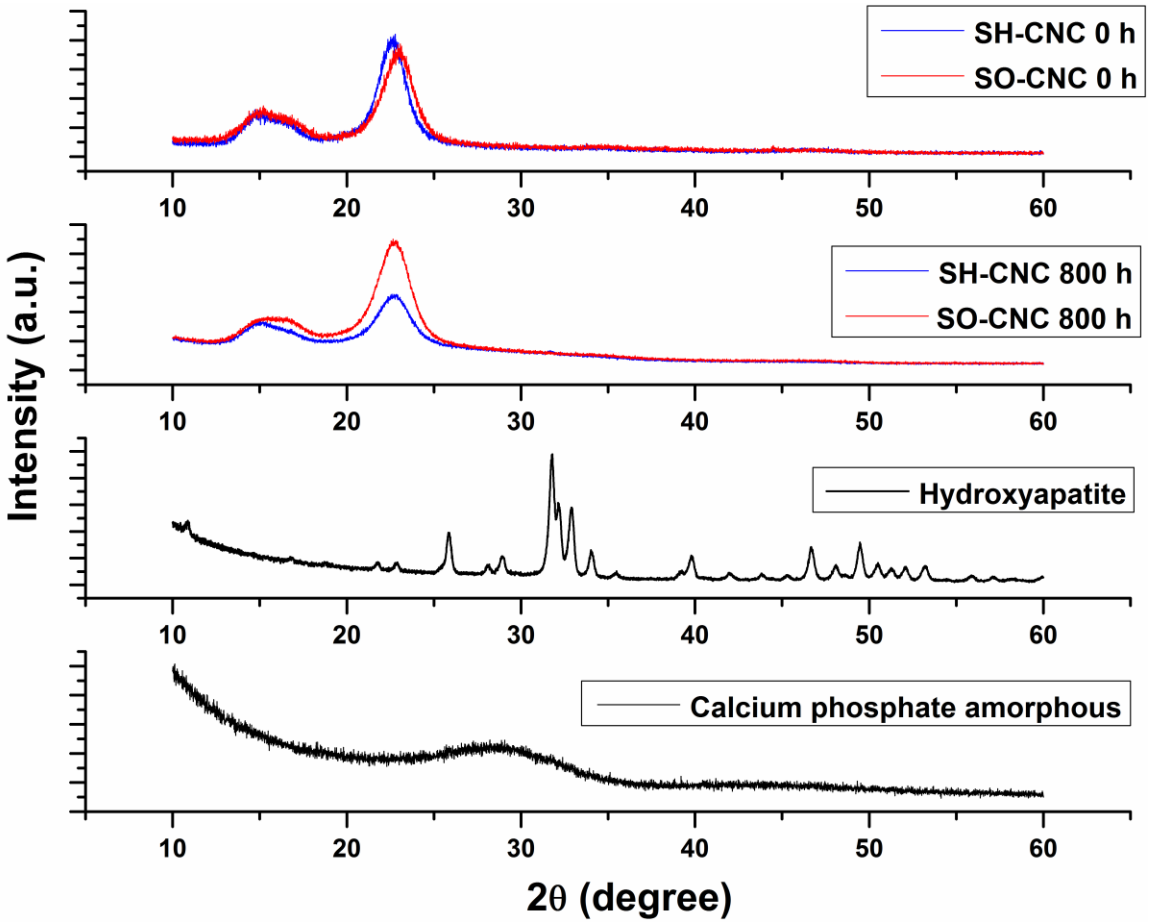

Figure B.1. X-ray diffraction pattern of CNCs before and after the mineralization compared to hydroxyapatite and calcium phosphate amorphous.

Appendix C. Themogravimetric analysis of SO-CNC, PCL 0 and PCL 10

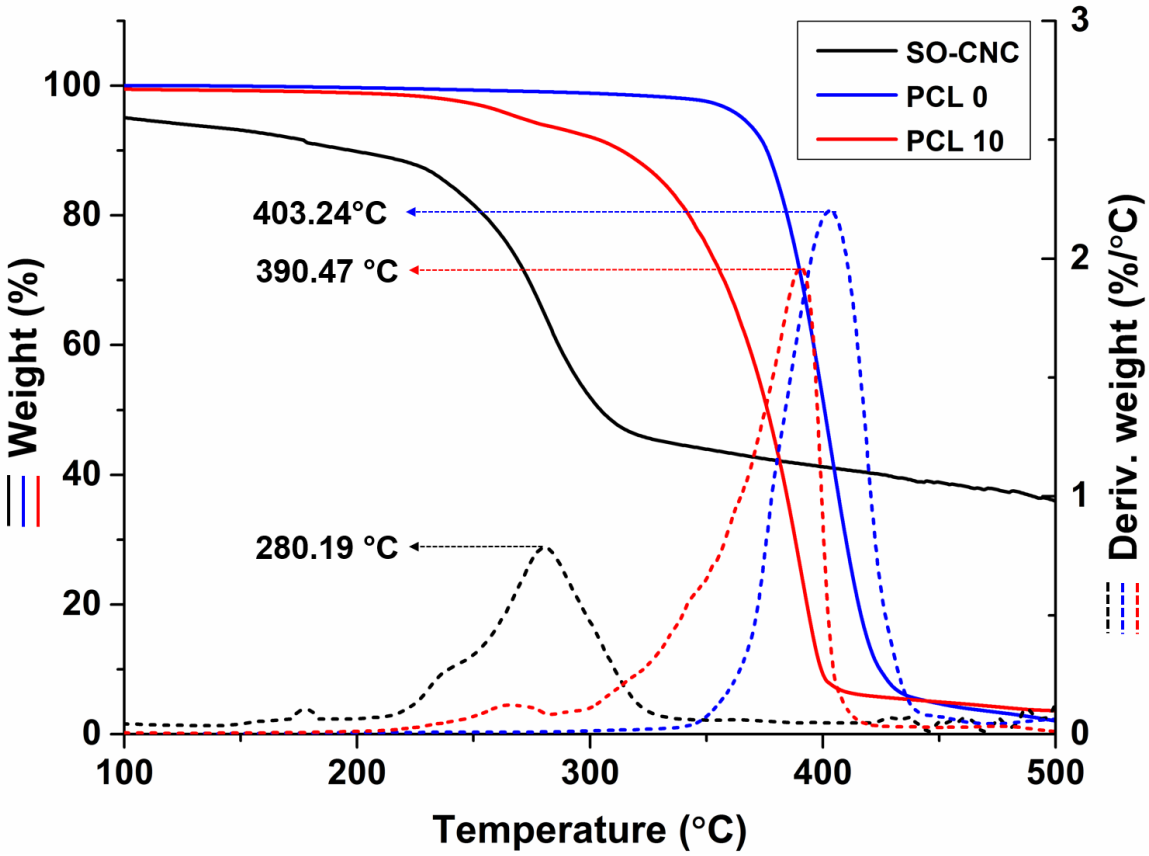

Figure C.1. TG (solid line) and DTG (dash line) curves for SO-CNC, PCL 0 and PCL 10.

Appendix D. Optical light microscopy images of PCL nanocomposites after heated at 300 °C

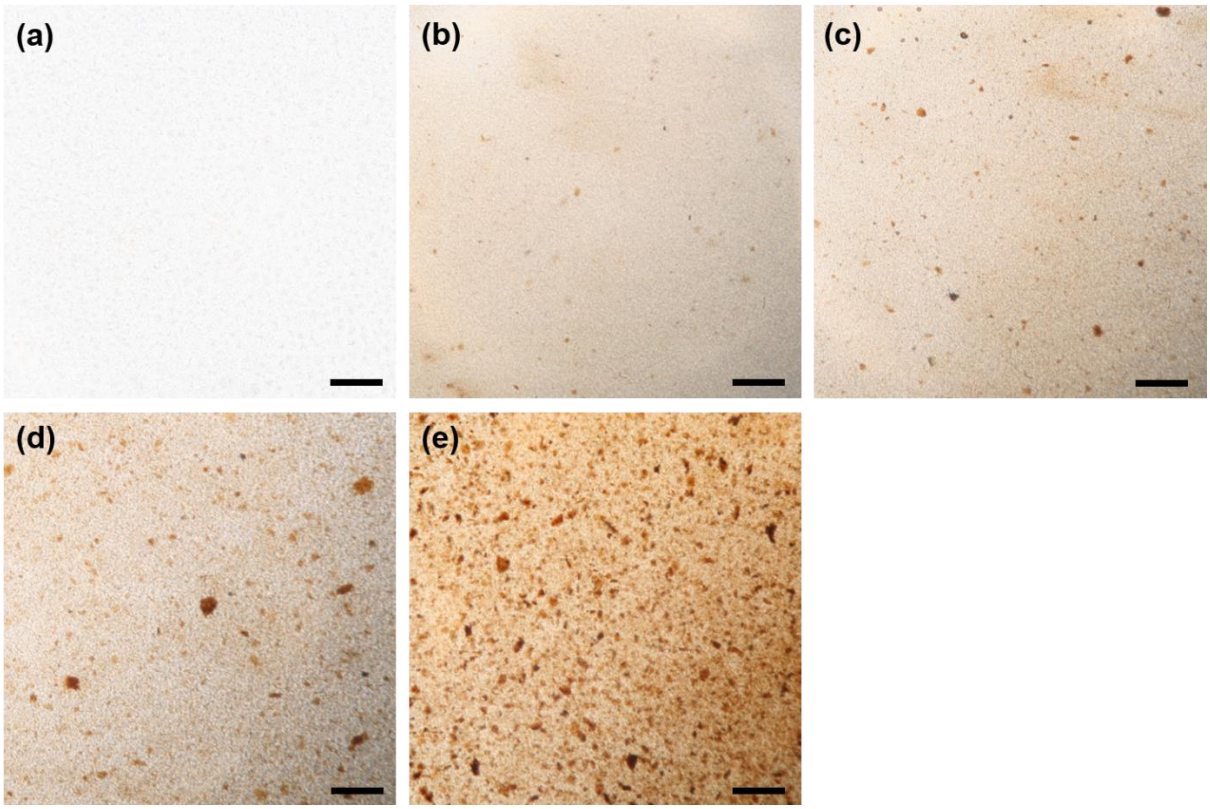

Figure D.1. Optical light microscopy images of PCL nanocomposites with different SO-CNC concentrations, (a) PCL 0 (0 wt %), (b) PCL 1 (1 wt %), (c) PCL 3 (3 wt %), (d) PCL 5 (5 wt %) and (e) PCL 10 (10 wt %) after heated at 300 °C for 10 min.